

The Pennsylvania State University
The Graduate School
College of Earth and Mineral Sciences

**MECHANISMS OF SINTERING AND SECOND PHASE
FORMATION IN BAYER ALUMINA**

A Dissertation in
Materials Science and Engineering
by
Tobias Frueh

© 2017 Tobias Frueh

Submitted in Partial Fulfillment
of the Requirements
for the Degree of

Doctor of Philosophy

September 2017

The dissertation of Tobias Frueh was reviewed and approved* by the following:

Gary Messing

Distinguished Professor of Ceramic Science and Engineering

Thesis Advisor, Chair of Committee

James Adair

Professor of Materials Science and Engineering, Biomedical Engineering and
Pharmacology

Optional Title Here

John Hellmann

Professor of Materials Science and Engineering

Associate Dean for Graduate Education and Research

Douglas Wolfe

Associate Professor of Materials Science and Engineering

Department Head, Advanced Coatings at the Applied Research Laboratory

Senior Scientist

*Signatures are on file in the Graduate School.

Abstract

Table of Contents

List of Figures	vii
List of Tables	xii
Acknowledgments	xiii
Chapter 1	
Introduction	1
1.1 Motivation	1
1.2 The Bayer Process	2
1.3 Influence of Impurities and Dopants on the Sintering Behavior of Al ₂ O ₃	3
1.3.1 MgO in Al ₂ O ₃	3
1.3.2 Other Impurities in Al ₂ O ₃	4
1.3.3 Impurities in MgO-doped Al ₂ O ₃	5
1.3.4 Influence of Na ₂ O and SiO ₂ on the Sintering Behavior of Al ₂ O ₃	8
Chapter 2	
The Effects of Na₂O and SiO₂ on Liquid Phase Sintering of Bayer Al₂O₃	14
2.1 Introduction	14
2.2 Experimental	15
2.3 Results	16
2.3.1 Effects of Na ₂ O-doping	16
2.3.2 Effects of Na ₂ O/SiO ₂ co-doping	17
2.4 Discussion	18
2.5 Summary	23

Chapter 3	
Powder Chemistry Effects on the Sintering Behavior of MgO-doped Bayer Alumina	36
3.1 Introduction	36
3.2 Experimental	38
3.3 Computational Methodology	39
3.4 Sintering and Microstructure Analysis	41
3.5 Mechanistic Interpretation	44
3.6 Summary and Conclusion	49
Chapter 4	
Dynamic development of nanometer scale grain boundaries during liquid phase sintering	66
4.1 Introduction	66
4.2 Experiment	68
4.3 Grain boundary thickness in MgO-free alumina	69
4.4 The equilibrium film thickness model	71
4.5 Calculation of the theoretical Equilibrium Film Thicknesses	72
4.6 High-resolution TEM	76
4.7 The effect of changes in powder chemistry	77
4.7.1 Na ₂ O/SiO ₂ ratio	77
4.7.2 MgO-doped Bayer alumina	78
4.8 Conclusion	78
Chapter 5	
Second phase formation in Bayer alumina	92
5.1 Introduction	92
5.2 Experimental	94
5.3 Results	94
5.3.1 Influence of MgO on the formation of β -Al ₂ O ₃	95
5.3.2 MgO-doped Bayer alumina	95
5.3.2.1 Number frequency of β -Al ₂ O ₃ grains	95
5.3.2.2 Size of β -Al ₂ O ₃ grains	96
5.3.3 Interpretation and mechanisms of formation	97
5.4 Summary	99
Chapter 6	
A Critique of the Master Sintering Curve Analysis of Sintering Processes	111
6.1 Introduction	111

6.2	Experimental Procedure	114
6.3	Results and Discussion	115
6.3.1	Anisotropy	115
6.3.2	MSC at high densities	116
6.3.3	Quantification of the MSC shape	117
6.3.4	Influence of forming technique	118
6.3.5	Influence of powder chemistry	118
6.3.6	Prediction of densities	119
6.4	Conclusions	119
Chapter 7		
	Summary and Future Work	134
7.1	Introduction	134
7.2	More Declaration	134
Bibliography		136

List of Figures

1.1	SIMS maps of Al_2O_3 doped with 500 ppm MgO (a) and 1000 ppm SiO_2 (b). Samples were sintered for 8 h at 1650°C [15].	12
1.2	SIMS maps of Al_2O_3 co-doped with 500 ppm MgO and 1000 ppm SiO_2 and sintered at 1650°C for 8h. (a) shows the distribution of SiO_2 , (b) the distribution of MgO in the same samples [15].	13
2.1	SEM image of as-received chemically purified Bayer Al_2O_3 powder used in this study.	27
2.2	Dilatometer curves of as-received and singly Na_2O -doped samples heated at 10°C/min to 1525°C.	28
2.3	Densification kinetics of Bayer Al_2O_3 doped with different Na_2O concentrations and sintered at 1525°C.	29
2.4	Microstructures of as-received and singly 529 ppm Na_2O doped samples after 30 min, 3 h and 8 h at 1525°C.	30
2.5	Dilatometer curves of as-received, singly SiO_2 -doped, and $\text{Na}_2\text{O}/\text{SiO}_2$ -doped Bayer Al_2O_3 heated at 10°C/min to 1525°C.	31
2.6	Densification kinetics of Bayer Al_2O_3 doped with different concentrations of Na_2O and SiO_2 at 1525°C.	32
2.7	Microstructures of Bayer Al_2O_3 doped with a) 603 ppm SiO_2 and b) 529 ppm Na_2O and 603 ppm SiO_2 after heating at 1525°C for 8h.	33
2.8	Micrographs of a sample doped with 1029 ppm Na_2O after sintering at 1525°C for 3 Åh. The micrographs were recorded using a) a secondary electron detector and b) a backscattered electron detector. The arrows point at the platelet shaped beta alumina grains that form in samples doped with Na_2O . The samples were not thermally etched.	34

2.9	Liquidus projection of the Al_2O_3 - SiO_2 - Na_2O ternary phase diagram. The red solid lines are isoplethal cuts representing the samples investigated in this study. The red dashed line is the 1525°C isotherm where α - Al_2O_3 and liquid are in equilibrium. The blue dash-dot line and green dotted line are eutectic lines at which α - Al_2O_3 and liquid is in equilibrium with β - Al_2O_3 or mullite, respectively.	35
3.1	SEM image of 380 ppm MgO-doped specialty alumina powder used in this work.	54
3.2	Dilatometer curves of a) 380 ppm MgO-doped and b) MgO-free [1] specialty alumina samples with different $\text{Na}_2\text{O}/\text{SiO}_2$ levels heated at 10°C/min to 1525°C.	55
3.3	Densification kinetics of specialty processed alumina containing different amounts Na_2O and SiO_2 and a) 380 ppm MgO sintered at 1450°C, b) 380 ppm MgO sintered at 1525°C, and c) 2 ppm MgO sintered at 1525°C [1].	56
3.4	Microstructures of 380 ppm MgO-doped specialty alumina samples with different Na_2O and SiO_2 concentrations sintered at 1525°C for 8 h.	57
3.5	Sintering trajectories (grain size vs. relative density) for 380 ppm MgO-doped specialty alumina samples with different Na_2O and SiO_2 concentrations.	58
3.6	Grain boundary of a sample containing 529 ppm Na_2O , 603 ppm SiO_2 , and 2 ppm MgO after 3 h at 1525°C.	59
3.7	Grain boundaries of samples containing 560 ppm Na_2O , 582 ppm SiO_2 , and 380 ppm MgO after a) 0 h and b) 3 h at 1525°C.	60
3.8	EDS of grain boundaries of samples containing 560 ppm Na_2O , 582 ppm SiO_2 , and 380 ppm MgO after a) 0 h and b) 3 h at 1525°C showing the Si distribution. After 0 h Si shows a stronger segregation to the grain boundaries than after 3 h.	61
3.9	EDS line scan across a grain boundary of a sample containing 560 ppm Na_2O , 582 ppm SiO_2 , and 380 ppm MgO after sintering at 1525°C for a) 0 h and b) 3 h.	62
3.10	Comparison of the formation energy of alpha- Al_2O_3 with an Mg-cluster (E_{Form}^{Mg}), Si-cluster (E_{Form}^{Si}) and Mg+Si-cluster (E_{Form}^{Mg+Si}) as a function of temperature. The formation energy difference (ΔE_{Form}) between the structures was calculated from Eq. REF to compare the formation energy values and show that it is energetically favorable to form Mg+Si-clusters over Si-clusters and Mg-clusters.	63

3.11	EDS maps of different oxides in 380 ppm MgO-doped specialty alumina samples after sintering at 1525°C for a-d) 0 h and e-h) 3 h.	64
3.12	Na ₂ O concentration (ICP measurements) of 380 ppm MgO-doped specialty alumina samples with 560 ppm Na ₂ O as a) function of sintering temperature and b) as a function of sintering time at 1525 °C.	65
4.1	Increase in concentration of liquid phase as a function of temperature for MgO-free powder samples with 529 ppm Na ₂ O and different SiO ₂ concentrations.	80
4.2	Relative density as a function of temperature and hold time determined from dilatometry for MgO-free powder samples with 529 ppm Na ₂ O and different SiO ₂ concentrations.	81
4.3	Liquid phase concentration as a function of relative density for MgO-free powder samples with 529 ppm Na ₂ O and different SiO ₂ concentrations.	82
4.4	Grain size - density trajectories as a function of Na ₂ O and SiO ₂ concentration for MgO-free alumina.	83
4.5	Change in Na/Al ion ratio in the liquid phase during sintering of samples with Na ₂ O/SiO ₂ ratios > 0.5.	84
4.6	Development of the electrostatic potential as a function of relative density. For MgO-free powder samples with 529 ppm Na ₂ O and different SiO ₂ concentrations.	85
4.7	Contributions to the equilibrium film thickness as a function of film thickness for MgO-free powder samples with 529/603 ppm Na ₂ O/SiO ₂ at a relative density of 93%.	86
4.8	Calculated equilibrium film thickness for MgO-free powder samples at different chemistries as a function of relative density.	87
4.9	Calculated grain boundary thicknesses as a function of relative density for MgO-free powder samples. The trajectories labeled with 529/603 ppm Na ₂ O/SiO ₂ , 529/203 ppm Na ₂ O/SiO ₂ , and 529 ppm Na ₂ O/SiO ₂ were calculated based on the liquid phase concentration and sintering stage. The equilibrium film thickness was calculated based on Clarke's model. The calculated grain boundary thicknesses are compared to measured grain boundary thicknesses (data points a: 1000/1000 ppm Na ₂ O/SiO ₂ , b) 529/603 ppm Na ₂ O/SiO ₂ , c) 529/203 ppm Na ₂ O/SiO ₂ after heating at 1525°C for 3 h).	88
4.10	TEM images of MgO-free powder samples with a) 529/203 ppm Na ₂ /SiO ₂ , b) 529/603 ppm Na ₂ /SiO ₂ , c) 1000/1000 ppm Na ₂ /SiO ₂ , and d) 29/103 ppm Na ₂ /SiO ₂ after sintering at 1525°C for 3 h.	89

4.11	TEM image of a MgO-free powder sample with 29/603 ppm Na ₂ O/SiO ₂ .	90
4.12	TEM images of MgO-doped (380 ppm) powder samples with a) 60/82 ppm Na ₂ O/SiO ₂ , b) 60/582 ppm Na ₂ O/SiO ₂ , and c) 560/582 ppm Na ₂ O/SiO ₂ . After heating at 1525°C for 3 h.	91
5.1	SEM micrographs of β -Al ₂ O ₃ grains in a-c) Bayer alumina with 560 ppm Na ₂ O, 82 ppm SiO ₂ , and 380 ppm MgO after 3 h at 1525°C and d) Bayer alumina with 29 ppm Na ₂ O, 103 ppm SiO ₂ , and 502 ppm MgO after 3 h at 1525°C. The samples in a) and b) were not etched and the samples in c) and d) were etched. a), c), and d) were obtained using a secondary electron detector, and b) was obtained using a backscattered electron detector.	101
5.2	Formation of β -Al ₂ O ₃ in MgO-free powder samples as a function of a) MgO concentration and b) Na ₂ O concentration in samples after 3 h at 1525°C.	102
5.3	Formation of β -Al ₂ O ₃ a function of a) Na ₂ O concentration, b) SiO ₂ concentration for different Na ₂ O concentrations, and c) of the Na ₂ O/SiO ₂ ratio in MgO-doped (380 ppm) powder samples. In c) the black diamonds are samples with 82 ppm SiO ₂ and the blue squares are samples with 182 and 582 ppm SiO ₂	103
5.4	Kinetics of β -Al ₂ O ₃ formation for different powder chemistries of MgO-doped powder samples (380 ppm MgO).	104
5.5	Micrographs showing β -Al ₂ O ₃ grains (red circles) in Bayer alumina samples with a) 1000 ppm MgO, 1000 ppm SiO ₂ , 29 ppm Na ₂ O, b) 2 ppm MgO, 1000 ppm SiO ₂ , 1000 ppm Na ₂ O, c) 1000 ppm MgO, 1000 ppm SiO ₂ , 1000 ppm Na ₂ O after 3 h at 1525°C.	105
5.6	Micrographs showing β -Al ₂ O ₃ grains (red circles) in MgO-doped (380 ppm) Bayer alumina samples with 82 ppm SiO ₂ and a) 185 ppm Na ₂ O, b) 560 ppm Na ₂ O, and c) 1060 ppm Na ₂ O after sintering at 1525°C for 3 h.	106
5.7	Micrographs showing β -Al ₂ O ₃ grains (red circles) in MgO-doped (380 ppm) Bayer alumina samples with a) 185/182 ppm Na ₂ O/SiO ₂ and b) 560/182 ppm Na ₂ O/SiO ₂ after sintering at 1525°C for 3 h. .	107
5.8	Micrographs showing β -Al ₂ O ₃ grains (red circles) in MgO-doped (380 ppm) Bayer alumina samples with 82 ppm SiO ₂ and 560 ppm Na ₂ O after sintering at 1525°C for a) 0 h, b) 1 h, and c) 8 h. . . .	108
5.9	XRD pattern of a sample with 1060 ppm Na ₂ O, 82 ppm SiO ₂ , and 380 ppm MgO after sintering at 1525°C for 5 h. The red arrows indicate the peaks that can be assigned to β -Al ₂ O ₃ . The other peaks can be assigned to α -Al ₂ O ₃	109

5.10	Micrograph showing β -Al ₂ O ₃ grains (red circles) in an ultra high purity powder sample with 502 ppm Na ₂ O, 2 ppm MgO, and 11 ppm SiO ₂ after sintering at 1525°C for 0 h	110
6.1	Dilatometry curves of slip cast CT3000LS-SG samples heated at a) 5°C/min, b) 10°C/min, and c) 20°C/min to 1525°C measured along different directions relative to the capillary force acting during slip casting.	121
6.2	Development of the anisotropy factor for shrinkage, k , as a function of relative density for CT3000LS-SG samples heated at different rates.	122
6.3	Development of the relative density corrected for anisotropy as a function of temperature for slip cast CT3000LS-SG samples for different heating rates.	123
6.4	Mean residuals of the MSC curves assuming different values for the activation energy Q for slip cast CT3000LS-SG samples.	124
6.5	Apparent activation energy of slip cast CT3000LS-SG samples obtained from anisotropy-corrected iso-density analysis.	125
6.6	MSC curves of CT3000LS-SG samples prepared by non-aqueous slip casting using the activation energy obtained from a) minimum mean residuals, and b) the average of the iso-density analysis.	126
6.7	MSC curve of CT3000LS-SG samples prepared by non-aqueous slip casting neglecting the anisotropic shrinkage in the samples. Q was obtained from the minimum mean residuals.	127
6.8	a) Densification of dry pressed CT3000LS-SG samples heated at different rates, b) mean residuals as a function of activation energy, and c) MSC for $Q = 700$ kJ/mol obtained from the minimum mean residuals, showing divergence at densities >90%.	128
6.9	Activation energy of dry pressed CT3000LS-SG samples as a function of relative density obtained from iso-density analysis.	129
6.10	Development of the microstructural parameters, summarized in a factor C , as a function of relative density for a dry pressed CT3000LS-SG sample.	130
6.11	MSC curves and activation energies of CT3000LS-SG samples obtained from the minimum mean residuals for samples prepared by different forming techniques.	131
6.12	MSCs and activation energies for CT3000LS-SG samples prepared by non-aqueous slip casting with different Na ₂ O concentrations. . . .	132
6.13	Equivalent time/temperature diagram for CT3000LS-SG samples prepared by non-aqueous slip casting heated at 10°C. The contours indicate what heat treatment is required to obtain the shown density.	133

List of Tables

2.1	Physical and chemical characteristics of the as-received Bayer Al ₂ O ₃ powder used in this study.	25
2.2	Calculated compositions and amounts of liquid in as-received, singly doped and co-doped samples at 1525°C ($\alpha = \alpha\text{-Al}_2\text{O}_3$, $\beta = \beta\text{-Al}_2\text{O}_3$, L= liquid, M = mullite).	26
3.1	Physical and chemical characteristics of the as-received 380 ppm MgO-doped specialty alumina powder used in this study.	51
3.2	Calculated compositions and amounts of liquid in 380 ppm MgO-doped specialty alumina samples of different chemistries at 1450°C and 1525 °C.	52
3.3	Lattice parameters and equilibrium energy (E_0) compared to previous first-principles and experimental values.	53
5.1	Estimated amount of $\beta\text{-Al}_2\text{O}_3$ in MgO-doped (380 ppm) Bayer alumina samples after 3 h at 1525°C.	100

Acknowledgments

Dedication

Chapter 1

Introduction

1.1 Motivation

Al_2O_3 is arguably the most extensively used and researched ceramic material with a total estimated market of 2.8 million tons per year. The applications for Al_2O_3 vary drastically such as high temperature refractories, technical ceramics, high voltage insulators, and functional fillers. Bayer feedstocks make a majority of the synthetic and specialty aluminas used in Al_2O_3 applications, such as aluminum trihydrate ($\text{Al}(\text{OH})_3$), smelter grade Al_2O_3 and others. Bayer process aluminas typically have a purity between 99.0 - 99.9% and contain impurities such as, Na_2O , CaO , Fe_2O_3 , and SiO_2 that originate from the bauxite ore and/or Bayer process reagents (e.g., NaOH). However, even with the focus being on purities between 99.0-99.9%, the vast majority of research has focused on ultra-high purity ($\geq 99.99\%$) aluminas derived from specialty feedstocks, such as ammonium alum ($\text{NH}_4\text{Al}(\text{SO}_4)_2 \cdot 12\text{H}_2\text{O}$), boehmite (AlOOH) and aluminum chloride (AlCl_3). These high purity powders ($\geq 99.99\%$ purity) are typically one to two orders of magnitude higher in cost than Bayer process aluminas (99.0 - 99.9% purity). Therefore, an overwhelming majority of the global market share, over 90%, use aluminas derived from the Bayer processes.

Research conducted on ultra-high purity aluminas can provide the best platform for understanding and conducting fundamental research but does not explore the types and amounts of impurities seen in teh typical Bayer aluminas. Different grades of Bayer Al_2O_3 powders are made that range in the amount and type of impurities. Additionally, MgO is added to commerical alumina powders because it

is known for its beneficial effects during sintering.

The purpose of this thesis is to provide an in-depth investigation of how the chemistry of commercial Bayer alumina powder affects the sintering mechanisms, densification, grain growth, and the nucleation and growth of second phases. Specifically, this dissertation will focus on understanding the effects and cross effects of MgO, Na₂O and SiO₂ on Bayer process aluminas and how the impurities effect the densification and microstructure evolution as well as, provide insight into the fundamental mechanisms that are responsible for changes in sintering behavior. Furthermore, a model is developed to describe the dynamic development of grain boundaries during densification as a function of powder chemistry. It is crucial to understand the structure and chemistry of grain boundaries during sintering, as grain boundary diffusion is the dominant mechanism for mass transport. The methodology developed to analyze sintering behavior, mechanisms, and grain boundaries during densification will serve as a model for investigating and tailoring the mechanisms of sintering in ceramic powders as a function of powder chemistry. Finally, the Master Sintering Curve approach is evaluated as a tool to evaluate the sinterability of ceramic powders.

1.2 The Bayer Process

The Bayer process is a hydrothermal precipitation process. An aqueous solution of caustic soda (NaOH) is used to digest the bauxite mineral ($\text{AlOOH} \cdot x\text{Fe}_2\text{O}_3 \cdot y\text{SiO}_2$) at pressures up to 40 bar and temperatures up to 230°C. Bauxite and NaOH form NaAl(OH)₄, which dissolves as a complex, while Fe₂O₃, SiO₂ and other accessory minerals separate as red mud because they are not soluble under these conditions. The temperature of the sodium aluminate solution is decreased to 50-70°C and Al(OH)₃ seed crystals are added to cause the Al(OH)₃ in the solution to precipitate. The Al(OH)₃ is then heat treated and calcinated at 1100-1200 °C to form α -Al₂O₃.

The main components of bauxite ore are SiO₂ and Fe₂O₃ and trace amounts are thus present in the final product. SiO₂ is also used in the milling media to grind the calcinate the powder and thus SiO₂ impurities may originate from the milling media [2]. Na₂O impurities are introduced through the digestion of the bauxite in NaOH and the precipitation of the Al(OH)₃ crystals from the NaAl(OH)₄ solution [2]. The Al(OH)₃ powder surface is washed to remove the NaOH, however,

small amounts of NaOH or rather Na₂O remain on the powder surface or are entrapped in the alumina grains. Other impurities such as gallium, calcium and magnesium originate from accessory minerals in the bauxite.

1.3 Influence of Impurities and Dopants on the Sintering Behavior of Al₂O₃

1.3.1 MgO in Al₂O₃

Since the work by Coble, showing that MgO doping produces high-density translucent alumina [3–5], numerous research has been completed to try and understand the underlying mechanisms. Initially the research by Coble concluded, that the abnormal grain growth is prevented by spinel particles that precipitate and pin the grain boundaries. Jorgensen [6, 7] used a solute-drag mechanism to explain the effect MgO had on the sintering of Al₂O₃. The solute-drag mechanism was based on the theory for metal systems that was proposed and refined by Lücke and Detert [8] and Cahn [9]. The mechanism suggests that MgO solutes segregate in the grain boundaries and thus controls the grain growth kinetics. When in the initial sintering stage with no grain growth, Jorgensen suggested that MgO decreases the sintering kinetics by lowering the diffusion coefficient and surface energy. Then during the later sintering stages, the segregated MgO increases the sintering kinetics by lowering the mobility of the grain boundaries by decreasing the rate of grain growth and thus leading to enhanced densification. The change in sintering kinetics was proposed by Johnson and Coble [10] to be due to the formation of a solid solution of MgO in Al₂O₃, which causes a change in grain growth and pore elimination. More recently, the role of MgO was proposed to be due to a segregation and precipitation mechanism by Zou et al. [11]. When MgO in Al₂O₃ exceeds the maximum solubility of MgO in the Al₂O₃ lattice and grain boundaries the excess MgO and Al₂O₃ forms spinel precipitates on the grain boundaries which reduces the grain boundary mobility and inhibits grain growth. However, Zou et al. [11] continues by proposing, that when MgO in the Al₂O₃ is below the solubility limit of the crystal and grain boundaries Schottky defects are formed :



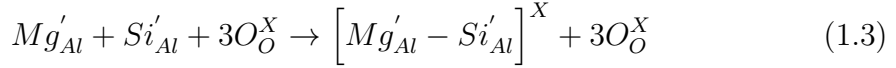
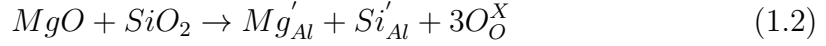
The densification and grain growth are enhanced by the formation of the Schottky defects by the increased concentration of point defects that facilitates diffusion and hence promotes the sintering. They suggest that the required MgO concentration to form spinel decreases with increasing grain size. This is explained by the fact that the total area of the grain-boundary interface decreases with increasing grain size, and hence the maximum concentration of MgO in the Al₂O₃ grain boundaries changes.

1.3.2 Other Impurities in Al₂O₃

With Coble's discovery [3–5], there has been a high interest in understanding how small concentrations of other dopants or impurities such as Na₂O, CaO, Fe₂O₃, and SiO₂ affect the sintering kinetics, density and microstructure of alumina. Bae and Baik [1, 12] showed that as long as the impurity content stayed below 10 ppm there was no abnormal grain growth in ultra pure Al₂O₃. Previous research has shown a correlation between the presence of a liquid phase and abnormal grain growth suggesting that the impurity content in commercial alumina powders (purity 99.7–99.8%) are high enough to form a liquid phase during sintering, if glass-forming impurities are present [2, 13–17]. Using transmission electron microscopy (TEM) Hansen and Philips [18] studied a 99.8% pure alumina powder, and their TEM images showed the presence of a thin glassy film in grain boundaries of sintered samples. Research has shown that the formation of a liquid phase during sintering can happen even in 99.98% pure alumina and thus cause abnormal grain growth can only be prevented by adding beneficial sintering additives like MgO [19]. Bae and Baik [12] were able to show that a liquid forms during sintering by co-doping Al₂O₃ with SiO₂ as soon as the solubility of SiO₂ and CaO in Al₂O₃ is exceeded. They estimated that the solubility of SiO₂ and CaO in Al₂O₃ is 100 and 20 ppm, and that discontinuous grain growth sets in after a critical thickness of the amorphous grain boundary has formed.

1.3.3 Impurities in MgO-doped Al₂O₃

As discussed above a very small amounts of impurities are sufficient for the formation of liquid phases during sintering, which exhibit a deleterious effect on the sintering of alumina. Therefore, for a better fundamental understanding of the role of MgO in Al₂O₃ the presence of other impurities should be considered. MgO is commonly used as an additive for the sintering of commercial aluminas because it prohibits the deleterious effect of the liquid phase forming impurities during sintering and facilitates the formation of a fine and homogeneous microstructure. From the literature, many explanations have been proposed to explain the effect of MgO on the sintering behavior of Al₂O₃ [2] REF 23. The solute-drag mechanism and the pinning-by-particle-precipitation mechanism are commonly accepted interpretations of the role of MgO regardless of the presence of other impurities REF 24, 25. However, another possible mechanism is that the liquid film by itself lowers the grain boundary mobility REF 26. This is due to the fact that MgO doping provides a uniform wetting of all grain boundaries causing slow isotropic grain growth whereas the undoped cases only basal planes are wetted. It was suggested by Bea and Baik [40] the kinetics of dissolution precipitation mass transport are changed by modifying the viscosity because MgO acts as a glass modifier in intergranular films. Still other interpretations suggest that MgO changes the solubility of other oxides in alumina. Handwerker et al. [14] suggested that the co-dissolving MgO and SiO₂ increases the solubility of SiO₂ because of strain and charge compensation which was further supported by the work of Gavrilov et al. [15]. They used high resolution scanning secondary mass spectrometry (SIMS) to investigate the distribution of impurities in sintered Al₂O₃ shown in Figure 1.1 and Figure 1.2. The SIMS maps of sintered Al₂O₃ singly doped with (a) 500 ppm MgO or with (b) 1000 ppm SiO₂ are shown in Figure 1.1, respectively. Areas of high dopant concentrations appear bright, and in both cases it can be seen that the dopants segregate to the grain boundaries. They showed in the SIMS maps in Figure 1.2 that co-doping Al₂O₃ with 500 ppm MgO and 1000 ppm SiO₂, leads both dopants to segregate to the grain boundaries, but with a substantially higher MgO and SiO₂ concentration towards the grain center. The authors claim that the solubility of MgO and SiO₂ in Al₂O₃ is increased by co-doping via the following defect compensation mechanism:



Coble and Roy 27 REF proposed a simliar reaction to explain a higher solubility of TiO_2 in Al_2O_3 when an equimolar amount of MgO is added. Gavrilov et al. [15] concluded the formation of a liquid phase during sintering is prevented by MgO increasing the solubility of glass forming impurities in Al_2O_3 . However, they note that other background-impurities might influence the solubility of MgO in Al_2O_3 as well.

More recently in literature, general explanations for microstructure evolution in ceramics and metals has been explored. The impurities or dopants were proposed to form thermodynamically stable grain boundary phases known as "complexions" and show transitions during sintering REF 23-27. They distinguish six complexions which can occur orderd or amorphous and depend on the thickness of the adsorbed layer: clean, monolayer, bilayer, multilayer, nanolayer and wetted. They further state that the type of complexion depends on impurity type, temperature, impurity concentration, and orientation of adjacent crystals and that the mobility of the grain boundaries is determined by the type of complexion. After the impurity solubility is exceeded in the crytal the impurities remain in the grain boundaries. The grain boundaries can then supersaturate during sintering because of the reduction of grain boundary area due to grain growth. The authors argue that there are only 2 ways for the excess impurities to reduce the free energy of the system. The first is by the the formation of a new phase and the second is by the transition to another complexion REF 30. These two possiblities are competing and which event will occur depends on the activation energy. Different complexions may co-exist in a microstructure since crystal planes of different orientation have different grain boundaries or interface energies and the type and number of complexions coexisiting depends mainly on the temperature. Another reason to consider for the formation of different complexions in the same microstructure is due to the inhomogeneous impurity distribution. The authors interpreted the microstructure developement of Al_2O_3 with different impurities using this concept. SiO_2 in Al_2O_3 does not have a preferred crystal plane on which it can form precipitations with low interfacial

energy. However, CaO impurities in Al_2O_3 can form calcium hexaluminate, which shows epitaxy on the basal planes of $\alpha\text{-Al}_2\text{O}_3$ and has a low interfacial energy. Therefore also has the activation energy for formation on the basal planes but the activation energy is too high for crystal planes with other orientations. Therefore, the authors' theory proposes that complexion transitions are preferred on the basal planes compared to all other planes which leads to anisotropic and abnormal grain growth. This phenomena is often observed in CaO containing alumina because the activation energy for precipitation is high for all crystal orientations and therefore this system is interpreted to prefer complexion transitions rather than the formation of a new phase. It is stated that the grain growth is enhanced with complexions that have higher grain boundary mobilities formed upon heating. For MgO in Al_2O_3 , their theory states that this system behaves isotropic and spinel precipitates are formed which prevents the formation of complexion transitions even though the activation for precipitation is low, or the precipitations occur uniformly throughout the microstructure. However, this model is not applied to densification and only describes the stable microstructure of dense ceramics and metals. Furthermore, the model does not explain how different chemistries and grain boundary structures affect the rate-limiting sintering mechanisms.

Kang et al. REF 28-31 uses the activation energy and driving force of atoms to cross the grain boundaries to explain the microstructure evolution in metals and ceramics. According to the authors interpretation equiaxed microstructure and normal grain growth happens if the critical driving force for appreciable grain boundary migration is zero and the grains grow "rough". The factors such as temperature, dopant concentration, and oxygen partial pressure, determine the critical driving force for appreciable grain boundary migration. If the critical driving force is zero then the step free energy has to be zero. Meaning the additional surface energy created during nucleation and growth of grains (the ledges of the nucleus) is zero. Thus the grains grow faceted if the critical driving force is not zero and abnormal grain growth occurs when the maximum driving force, i.e. the driving force for the largest grains to grow, is larger than the critical driving force. However, if the maximum driving force is a lot larger than the critical driving force meaning that the driving force of many grains is larger than the critical driving force, than grains start growing fast and abnormally but form a microstructure that looks like a normally grown microstructure, and this is defined as pseudo-normal grain growth.

Grain growth becomes stagnant if the maximum driving force is smaller than the critical driving force and thus the microstructure does not change. Parameters such as partial pressure, temperature, dopants, and impurities for different materials systems were investigated by Kang et al. but they only explained the microstructure evolution qualitatively with a described model, and the majority of observations from experiments were fitted into the model rather than predicted by the model. For example, it is concluded that MgO lowers the step free energy of alumina since the addition of MgO to alumina results in a homogeneous and equiaxed microstructure REF 30-31. However, it is not explained why MgO lowers the step free energy, and why MgO is the only material that lowers the step free energy in that manner. Furthermore the model only takes into account the microstructural evolution in already dense bodies, and does not address densification.

1.3.4 Influence of Na₂O and SiO₂ on the Sintering Behavior of Al₂O₃

Despite the extensive interest in the effects that Na₂O has on the sintering of alumina only a few studies have been published. The effect of adding 1 wt.% Na₂O to high purity alumina powder was published by Sumita and Bowen (Sumitomo, AKP-HP) REF 33. However, after sintering at 1400°C for 2 h, they determined, using inductively coupled plasma (ICP), that only ~8 ppm Na₂O was present and did not add any additional details to explain the large discrepancy between the doping concentration and the amount after sintering. The effect of 1 wt.% of different additives on the sintering of 99.3% alumina (Alcoa A-11) was studied by Smothers and Reynolds REF 34. They showed that grain growth is inhibited and sintering is retarded by Na₂CO₃ or NaF. Cahoon and Christensen REF 35 also reported a deleterious effect of Na₂O on the sintering of alumina. They added between 300 ppm and 5.9 wt.% Na₂O to their alumina powder (Alcoa A-14, no purity specifications given) and heated the samples in a 5 days cycle (2 days heating, 3 days cooling) to temperatures between 1600°C and 1835°C for 1 h. They showed an inhibition of abnormal grain growth and a retardation of sintering with increasing Na₂O as well as cracking of their samples and inferior compressive strengths. Their suggestion was that the formation of β - or ζ -Al₂O₃ caused these effects. They also reported a "moderately deleterious effect" of SiO₂ on the sintering of Al₂O₃. They

reported that concentrations of SiO_2 as low as 0.1 wt.% can inhibit abnormal grain growth and that with increasing SiO_2 this effect is enhanced. When co-doping Al_2O_3 with Na_2O and SiO_2 they found that the deleterious effects of Na_2O were moderated. The effect of doping Al_2O_3 with Na_2O and SiO_2 on densification and microstructure evolution was studied by Louet et al. REF 36 for the Bayer process alumina (Rhone-Poulenc, P172SB), containing 550 ppm Na_2O , 770 ppm SiO_2 , 1010 ppm MgO , 600 ppm CaO and 115 ppm Fe_2O_3 . The levels of Na_2O and SiO_2 were adjusted by adding $\text{CH}_3\text{COOH-Na}$ and silica gel. They measured the concentrations of samples after sintering for 2 h at 1540°C while adding Na_2O using ICP and saw they had less than 50 wt.% of their targeted amount. The difference was explained by stating AlJNa has a very low vaporization temperature (882.9°C) and may easily evaporate from this liquid phase³⁶ REF 36. Unfortunately, there was no attempt to verify this contention, even though, the effect of Na_2O concentrations as high as 1510 ppm were studied. It was concluded from this work that the doping of Na_2O causes the sintering process to slow and decreases the sintering density from 98 to 97 % when the Na_2O concentration goes from 550 ppm to 1150 ppm. The authors reported a drop in grain size from 4-5 μm to 3 μm when the concentration of Na_2O was greater than 1000 ppm. They then noted that high levels of Na_2O result in a homogenous, fine microstructure. This work also reported that in the presence of Na_2O , increasing SiO_2 concentration from 770 ppm to as high as 1500 ppm causes anisotropy of the grains but does not affect the final density. The authors' work stated that increasing SiO_2 concentratiaon leads to abnormal grain growht but does not effect the average grain size. However, their presented micrographs show an increase in grain size with increasing SiO_2 concentration but no abnormal grain growth. The authors' did note that the interperting the results in terms of what is caused by Na_2O or SiO_2 impurities is difficult because the as-received powder has a large number and high concentrations of several impurities. The effects of different SiO_2 - and Na_2O concentrations on the sintering behaviour of alumina was also investigated by Compson et al. [2]. They chose four commercial alumina powders that were 99.8 wt.% pure and had similar specific surface areas, particle diameter and particle distributions. The four commercial powders only varied in their impurity concentrations. Specifically, the Na_2O and SiO_2 concentrations varied from 0.02 to 0.1% and 0.01 to 0.04%, respectively. They showed that the four powders exhibited different shrinkage, sintering and densification behavior in

the temperature range from 1150°C to 1500°C using dilatometry. From their work, they concluded that SiO₂ has a deleterious effect on the sintering of Al₂O₃, but they could not detect an influence of Na₂O.

This completed thesis consists of the studying the main tasks:

1. Effects of Na₂O and SiO₂ on liquid phase sintering of Bayer Al₂O₃
2. Powder chemistry effects on the sintering behavior of MgO-doped Bayer Al₂O₃
3. Dynamic development of nanometer scale grain boundaries during liquid phase sintering
4. Second phase formation in Bayer Al₂O₃
5. A critique of the master sintering curve analysis of sintering processes

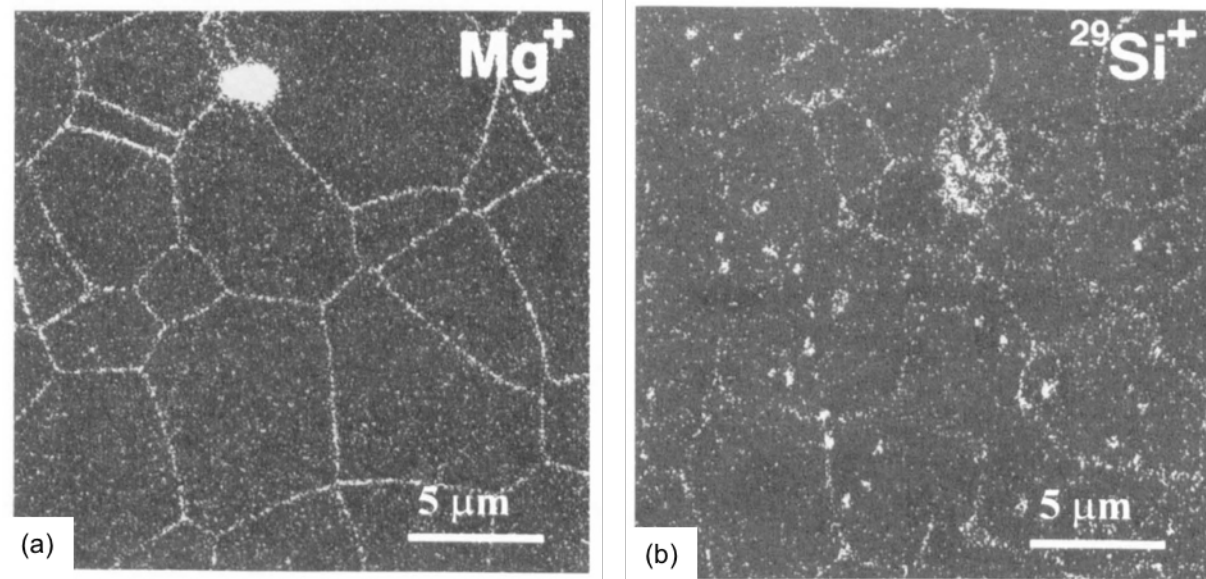


Figure 1.1. SIMS maps of Al_2O_3 doped with 500 ppm MgO (a) and 1000 ppm SiO_2 (b). Samples were sintered for 8 h at 1650°C [15].

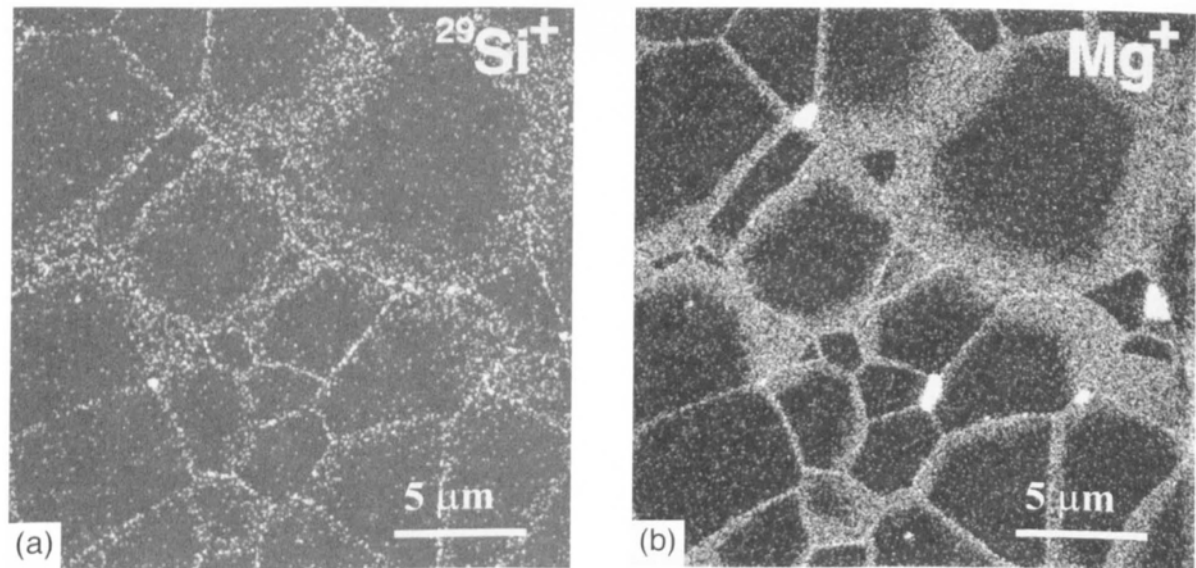


Figure 1.2. SIMS maps of Al_2O_3 co-doped with 500 ppm MgO and 1000 ppm SiO_2 and sintered at 1650°C for 8h. (a) shows the distribution of SiO_2 , (b) the distribution of MgO in the same samples [15].

Chapter 2 |

The Effects of Na₂O and SiO₂

on Liquid Phase Sintering of Bayer

Al₂O₃

2.1 Introduction

Al₂O₃ is arguably the most extensively used and researched ceramic material because it is used in many large volume applications such as high temperature refractories, technical ceramics, high voltage insulators, and functional fillers. The majority of Al₂O₃ applications use synthetic or specialty aluminas derived from Bayer feedstocks, such as aluminum trihydrate (Al(OH)₃), smelter grade Al₂O₃ and others. Bayer process aluminas are typically 99.0 - 99.9% pure and contain Na₂O, CaO, Fe₂O₃, and SiO₂ impurities that originate from the bauxite ore and/or Bayer process reagents (e.g., NaOH). The vast majority of research on the sintering of Al₂O₃, however, focuses on ultra-high purity ($\geq 99.99\%$) aluminas derived from specialty feedstocks, such as ammonium alum (NH₄Al(SO₄)₂·12H₂O), boehmite (γ -AlOOH) and aluminum chloride (AlCl₃). While ultra-high purity aluminas provide the purest platform from which to conduct fundamental sintering research, that research does not usually explore the types and amounts of impurities typical of Bayer aluminas. Commercial Bayer Al₂O₃ powders exist in a range of reactive grades that differ in the amount and types of these impurities. Therefore, the evaluation of specialty reactive aluminas, within the context of previous work on ultra-high purity aluminas, is a valuable contribution to industrial users and bridges

fundamental sintering research with ultra-high purity aluminas.

2.2 Experimental

A chemically purified 0.4 μm median particle size Bayer process Al_2O_3 powder (Almatis, Inc., Leetsdale, PA, USA) with only 2 ppm MgO was used to study the sintering of near MgO -free Bayer Al_2O_3 (Figure 2.1). The powder was chemically purified by the manufacturer so that impurity levels similar to commercial high purity Bayer process aluminas were obtained after doping with Na_2O and/or SiO_2 . The physical and chemical characteristics of the as-received powder are shown in Table 2.1. Chemical analysis of the as-received Al_2O_3 was performed by inductively coupled plasma (ICP) emission spectroscopy (iCap 6000, Thermo Fischer Scientific, Inc., Waltham, MA, USA) after Al_2O_3 samples were acid digested in a microwave digestion unit in a TeflonTM sample holder. It should be noted that the as-received Bayer Al_2O_3 contained impurity levels of 90 ppm Fe_2O_3 , 62 CaO , and 22 ppm TiO_2 . The Na_2O and SiO_2 reported after doping include the impurity concentrations in the as-received powder (29 ppm Na_2O and 103 ppm SiO_2).

The Al_2O_3 powders were doped with up to 1000 ppm Na_2O using sodium acetate ($\text{NaC}_2\text{H}_3\text{O}_2 \cdot 3\text{H}_2\text{O}$, ACS grade, BDH, West Chester, PA, USA), based on the procedure reported by Louet et al. [?]. The Al_2O_3 powders were dispersed in a solution of sodium acetate dissolved in de-ionized water. The suspension was stirred on a magnetic stir plate for 5 h at room temperature, and held at 80°C for 24 h while stirring until the mixture was too viscous to stir, and then dried at 100°C for 24 h.

Samples were doped with up to 500 ppm SiO_2 by first dissolving tetraethyl orthosilicate (TEOS, $\text{Si}(\text{OC}_2\text{H}_5)_4$, 98%, Aldrich Chemical Company, Inc., Milwaukee, WI, USA) in 200 proof ethanol with a few drops of de-ionized water to hydrolyze the TEOS and immediately mixed at room temperature for 5 h with either the as-received or Na_2O -doped Al_2O_3 powder. The mixture was subsequently stirred at 70°C for an additional 12 h. The powder was then dried at 100°C for 2 h, followed by crushing in a mortar and pestle, and sieving to -106 μm (US Standard 140 mesh).

Samples were prepared for sintering studies by uniaxially dry pressing the powders at 170 MPa and then cold isostatic pressing at 200 MPa (CIP, Autoclave

Engineers, Erie, PA, USA) to obtain cylindrical samples (3.0-3.5 mm long by 12.7 mm diameter or 8.5-10 mm long by 6 mm diameter) with green densities of 59.0% \pm 0.5% of theoretical density. To investigate the sintering process, dry pressed 8.5-10 mm long by 6 mm diameter cylinders were heated at 10°C/min to 1525°C in a thermomechanical analyzer (TMA, Linseis PT1600, Robbinsville, NJ, USA). The kinetics of sintering and grain growth were evaluated on 3.0-3.5 mm long by 12.7 mm diameter samples heated at 10°C/min to 1200 °C then 5°C/min to 1525°C followed by sintering at 1525°C for up to 8 h. The density of three samples of each condition was measured by the Archimedes method according to ASTM standard B962-15 [20] and the average density reported for each sintering time and temperature. For microstructure analysis, samples were first polished to a surface finish of 1 μ m and then thermally etched in air at 1425°C for 40 min. Average grain sizes were measured on SEM (ESEM, Quanta 200, FEI Company, Hillsboro, OR, USA) micrographs using a linear intercept method (ASTM Standard E112-96) [21].

2.3 Results

2.3.1 Effects of Na₂O-doping

The doping experiments were designed to uniformly distribute Na₂O and SiO₂ on the surfaces of the Al₂O₃ particles. Upon heating the dopant NaC₂H₃O₂·3H₂O first dehydrates and then decomposes to form Na₂CO₃ above 385°C [22]. Using a video recorder, we observed that anhydrous sodium acetate melts and rapidly spreads on the surface of an Al₂O₃ substrate at \sim 420°C. Na₂CO₃ melts at 851°C and subsequently decomposes to Na₂O [22]. As a result of the rapid wetting of the Na₂O precursor on the Al₂O₃ substrate we conclude that Na₂O is uniformly distributed on the powder surface by the acetate doping process.

Figure 2.2 shows the shrinkage behavior of Bayer Al₂O₃ doped with different Na₂O concentrations during heating to 1525°C at 10°C/min. The as-received Al₂O₃ (intrinsic impurities: 29 ppm Na₂O, 103 ppm SiO₂) begins to shrink at \sim 1050 °C, whereas shrinkage begins at 1100°C for samples doped with 1029 ppm Na₂O. The difference in density at the beginning of densification continues throughout the heating cycle. However, above \sim 1350°C the densification rate of the Na₂O doped samples surpasses that of the as-received sample. Overall, the Na₂O-doped samples

are 2.5% less dense than the as-received Al_2O_3 after heating to 1525°C.

Figure 2.3 shows the influence of Na_2O concentration on the densification kinetics at 1525°C. Clearly, the degree of densification decreases with increasing Na_2O concentration for up to 30 min with the Na_2O -doped samples being as much as 2% less dense than the as-received Al_2O_3 . However, after ≥ 30 min at 1525°C densification is independent of Na_2O content and all samples are 97.5-98.0% dense after ≥ 3 h.

The microstructures of as-received samples (29 ppm Na_2O) and samples doped with 529 ppm Na_2O sintered for 30 min, 3 h and 8 h at 1525°C are compared in Figure 2.4. It is seen that higher Na_2O concentration does not affect the average grain size for all hold times. Microstructures of as-received samples are predominantly equiaxed with a small number of faceted grains, whereas samples doped with Na_2O appear to have an increasing number of faceted grain boundaries with increasing Na_2O concentration. A few tabular grains of up to $60 \mu\text{m}$ were seen in both as-received and Na_2O -doped samples after 8 h at 1525°C (see Figure 2.4c and 2.4f). Those faceted grains are larger in the as-received powder samples compared to Na_2O -doped samples, whereas the Na_2O -doped samples show more large tabular grains than samples from the as-received powder.

2.3.2 Effects of $\text{Na}_2\text{O}/\text{SiO}_2$ co-doping

As seen in Figure 2.5, the presence of 603 ppm SiO_2 significantly retards densification of as-received alumina. Starting at $\sim 1250^\circ\text{C}$, all of the SiO_2 -doped samples densify less than as-received and singly Na_2O -doped samples. The densification rate of the SiO_2 -doped samples from 1250 to 1525°C is slower than the as-received alumina. SiO_2 reduces the linear shrinkage by $\sim 3.0\%$ and thus the samples are 8.7% less dense than the as-received Al_2O_3 after 8 h at 1525°C.

The densification kinetics of the Al_2O_3 powders doped with different amounts of Na_2O (154 and 529 ppm) and SiO_2 (203 and 603 ppm) are compared in Figure 2.6. It is seen that the addition of SiO_2 significantly reduces sintered density for all hold times. For example, samples containing as much as 603 ppm SiO_2 have densities of 81.5% after 0 h and 93.8% after 8 h at 1525°C, whereas the as-received and singly Na_2O -doped Al_2O_3 samples are 98% dense after 3 h at 1525°C.

Figure 2.6 shows the effect of Na_2O on the densification of SiO_2 -doped samples.

For hold times < 1 h, samples doped with 529 ppm Na₂O and 203 ppm SiO₂ are ~ 1.5% denser than samples doped with 154 ppm Na₂O and 203 ppm SiO₂. A difference in Na₂O concentration does not affect the final density of samples containing 203 ppm SiO₂ (96.5 - 97.0%) after 3 h at 1525°C. For higher SiO₂ concentrations (603 ppm), singly SiO₂ doped samples are 1 - 2.5% less dense than samples co-doped with 529 ppm Na₂O and 603 ppm SiO₂ for all hold times at 1525°C.

The average grain sizes of the as-received and Na₂O-doped samples are nominally the same and increase from 1.6 μm to 2.5 μm after 30 min and 8 h at 1525°C, respectively. There was little grain growth (1.4 μm to 2.1 μm) in singly SiO₂-doped samples (603 ppm) after 30 min and 8 h at 1525°C, respectively. In samples co-doped with 529 ppm Na₂O and 603 ppm SiO₂ the average grain size is 1.6 μm for hold times between 30 min and 8 h at 1525°C. The limited grain growth is attributed primarily to the large fraction of porosity. Micrographs of 603 ppm SiO₂ singly doped and 529 ppm Na₂O and 603 ppm SiO₂ co-doped samples heated for 8 h after heating for 8 h at 1525°C are compared in Figure 2.7. Both samples are only 92-94% dense and thus it was difficult to prepare polished micrographs without some grain pull-out.

2.4 Discussion

To understand the above effects, we first note from the Al₂O₃-Na₂O phase diagram [?] that Na₂O is insoluble in α -Al₂O₃. A few platelet shaped grains with high aspect ratios were observed in the microstructures of sintered Na₂O-doped samples (Figure 2.8). Due to their morphology and literature reports, [?, 23–26] it is assumed that these grains are a type of β -Al₂O₃. Four types of β -Al₂O₃ exist; two of them, β -Al₂O₃ (Na₂O·11Al₂O₃) and β'' -Al₂O₃ (Na₂O·5Al₂O₃), form in the binary system Na₂O-Al₂O₃ [27, 28]. The determination of which type of β -Al₂O₃ forms and the conditions of formation were not the subject of this work, so these analyses were not performed.

Sodium aluminate (NaAlO₂) is reported to form at temperatures as low as 900°C, [29] and β'' -Al₂O₃ (Na₂O·5Al₂O₃) can be synthesized at temperatures as low as 1100 °C [23, 30, 31]. Therefore, we hypothesize that either sodium aluminate or β'' -Al₂O₃ forms before the onset of densification and that the presence of the

second phases on the surface of the Al₂O₃ particles retards the initial shrinkage of Na₂O-doped samples at \sim 1050°C. However, we did not observe any β -Al₂O₃ type grains in the samples at this temperature. Alternatively, as discussed below, Na₂O may interact with the 103 ppm of intrinsic SiO₂ in the sample.

We hypothesize that the initial grain boundaries in the as-received Al₂O₃ are wetted with the intrinsic impurities such as Na₂O, CaO, TiO₂ and SiO₂. Doping with Na₂O and SiO₂ changes the relative grain boundary chemistries and the properties of the respective grain boundary liquids. In the presence of a grain boundary liquid, densification occurs by a solution-precipitation sintering process, and thus, the rate of densification is controlled by either interface reaction between the grain boundary liquid and Al₂O₃ grains, or by the diffusion of Al³⁺ through the liquid grain boundary film. Al³⁺ diffusion is rate-limiting at 1525°C since it has been shown for molten glass systems that Al³⁺ has lower ionic diffusion rates than O²⁻ [32]. For diffusion-controlled densification, the densification rate is given by [33, 34]

$$\frac{d\left(\frac{\Delta\rho}{\rho}\right)}{dt} = \frac{A\delta D_l C_0 \gamma_{lv} \Omega}{kT} r_s^{-4} \quad (2.1)$$

and for interface reaction-controlled densification, the densification rate is given by

$$\frac{d\left(\frac{\Delta\rho}{\rho}\right)}{dt} = \frac{B K C_0 \gamma_{lv} \Omega}{kT} r_s^{-2} \quad (2.2)$$

where A and B are geometric factors, δ is the thickness of the liquid film, D_l is the diffusion coefficient of Al³⁺ in the liquid, C_o is the equilibrium solute concentration, K the interface reaction constant, γ_{lv} is the liquid surface tension, Ω is the molecular volume of the solid, r_s is the particle radius, k is the Boltzmann constant and T is absolute temperature.

Equations 2.1 and 2.2 can be used to gain insights into the rate-limiting densification mechanisms during liquid phase sintering by evaluating their ratio [33, 34]

$$\alpha = \frac{A\delta D_l}{B K} r_s^{-2} \quad (2.3)$$

In general, for $\alpha > 1$, densification is controlled by the interface reaction, since D_l is relatively high. For $\alpha < 1$, densification is controlled by diffusion, and for $\alpha = 1$ both mechanisms contribute equally to densification [34]. Since the product

of the grain boundary thickness and the diffusion coefficient greatly influences the rate-determining mechanism, δD_l and the interface reaction constant K were examined in more detail.

Because the main impurities in Bayer aluminas are SiO_2 and Na_2O , the Al_2O_3 - SiO_2 - Na_2O ternary phase diagram [?] was utilized to evaluate the effects of dopant type and concentration on solubility of Al_2O_3 in the grain boundary liquid. It is assumed that the system approaches thermodynamic equilibrium upon holding at 1525°C, and thus the equilibrium composition of the liquid at 1525°C can be calculated from the ternary phase diagram (Figure 2.9). For simplification, we considered only Al_2O_3 , SiO_2 and Na_2O for the analysis, and assumed that all impurities/dopants are located in the grain boundaries. It was stated earlier that Na_2O is not soluble in Al_2O_3 , and it has been reported in the literature that SiO_2 segregates at the grain boundaries in Al_2O_3 [35]. Figure 2.9 shows the liquidus projection of the Al_2O_3 - SiO_2 - Na_2O ternary phase diagram. The red solid lines connecting the Al_2O_3 end member to the Na_2O - SiO_2 side are binary cuts through the ternary (isoplethal sections) and correspond to some of the $\text{Na}_2\text{O}/\text{SiO}_2$ ratios investigated in this study. The red dashed line is the isotherm at 1525°C for the part of the phase diagram where α - Al_2O_3 and liquid are in equilibrium. The blue dash-dot line and the green dotted line are eutectic lines along which β - Al_2O_3 or mullite is stable with α - Al_2O_3 and a liquid. The isotherm and the eutectic lines are important for determining the stable phases and the composition of the liquid in the samples. If a binary cut intersects the isotherm (red dashed line) only α - Al_2O_3 and liquid are stable phases at 1525°C and the intersection point determines the composition of the liquid. If a binary cut intersects one of the two marked eutectic lines (blue dash-dot or green dotted) a third phase (β - Al_2O_3 or mullite) is stable in those samples, and the composition of the liquid at 1525°C is determined by the intersection point of the respective intersected eutectic line with the isotherm at 1525°C.

The Al_2O_3 - SiO_2 - Na_2O phase diagram demonstrates that a small amount of liquid is stable at 1525°C for all compositions investigated. Note that these overall compositions are all very close to the Al_2O_3 end member ($\sim 99.8\%$ Al_2O_3) and Na_2O and SiO_2 are insoluble in Al_2O_3 . Isoplethal sections (red solid lines in Figure 2.9) can be used to determine the stability and equilibrium composition of a liquid since the volume fractions of Na_2O and SiO_2 are known. Lambotte and

Chartrand [?] calculated isoplethal sections of the ternary phase diagram, and based on their calculations, the solubility of Al_2O_3 in the liquid at 1525°C in the samples was estimated based on the respective $\text{Na}_2\text{O}:\text{SiO}_2$ ratios (assuming a constant liquid density of 2.45 g/cm [21, 36]). Likewise, the volume fractions of liquid and solid phases can be estimated since the doping and impurity concentrations of SiO_2 and Na_2O are known. Table 2.2 summarizes the stable phases, the liquid compositions, and the total amount of liquid in the as-received and doped samples. Stable liquids at 1525°C are predicted for liquid compositions with $\text{Na}_2\text{O}:\text{SiO}_2$ ratios between 0.25 and 0.5. As described above, for higher Na_2O concentrations in the samples (global $\text{Na}_2\text{O}:\text{SiO}_2$ ratio > 0.5), $\alpha\text{-Al}_2\text{O}_3$, $\beta\text{-Al}_2\text{O}_3$ and a liquid with a $\text{Na}_2\text{O}:\text{SiO}_2$ ratio of 0.5 are stable. For sample compositions with higher SiO_2 concentrations (global $\text{Na}_2\text{O}:\text{SiO}_2$ ratio < 0.25) $\alpha\text{-Al}_2\text{O}_3$, mullite and a liquid with a $\text{Na}_2\text{O}:\text{SiO}_2$ ratio of 0.25 are stable. Since the global $\text{Na}_2\text{O}:\text{SiO}_2$ ratio in most of the samples investigated in this work is either > 0.5 or < 0.25, the liquid in those samples had compositions of 0.5 or 0.25, respectively. As the $\text{Na}_2\text{O}:\text{SiO}_2$ ratio in the liquid increases from 0.25 to 0.5 the solubility of Al_2O_3 in the liquid increases from 18.4 vol.% to 21.6 vol.% [?]. The increased Al_2O_3 solubility leads to higher densification rates and higher densities in $\text{Na}_2\text{O}/\text{SiO}_2$ co-doped samples compared to singly SiO_2 -doped samples, regardless of the rate-limiting process.

Assuming fully dense samples and the liquid volume fractions reported in Table 2.2, we calculated the grain boundary thickness δ using:

$$\delta = 2 \frac{V_g \phi}{S_g (1 - \phi)} \quad (2.4)$$

where ϕ is the liquid volume fraction and V_g and S_g are the volume and the surface area based on the average grain size, respectively. For as-received and singly Na_2O -doped samples the grain boundary thickness is < 0.3 nm for all observed grain sizes. For $\text{Na}_2\text{O}/\text{SiO}_2$ -co-doped samples (603 ppm SiO_2) the grain boundary thickness is between 0.8 and 1.8 nm for grain sizes of 1 μm and 2.5 μm , respectively. The calculated grain boundary thickness of singly SiO_2 -doped samples is similar to that of as-received samples, since mullite is predicted to form in the $\text{Al}_2\text{O}_3\text{-SiO}_2\text{-Na}_2\text{O}$ system for low Na_2O concentrations at 1525°C. However, mullite may not form in Bayer process Al_2O_3 due to the presence of other impurities, such as CaO , which, similar to Na_2O , lowers the eutectic temperature and acts as a network modifier

in the glass. Therefore, the grain boundary thicknesses of singly SiO_2 -doped and $\text{Na}_2\text{O}/\text{SiO}_2$ co-doped samples are expected to be similar at ~ 1.8 nm. The amount of liquid in the samples and, therefore, the grain boundary thickness, is governed mainly by the amount of glass forming species in the samples, i.e. SiO_2 .

The diffusion coefficient of Al^{3+} through the liquid grain boundary phase can be calculated with the Eyring relation

$$D_l = \frac{kT}{\eta\lambda} \quad (2.5)$$

where η is the viscosity of the grain boundary liquid and λ is the jump distance of the diffusion species, taken as the ionic diameter of an Al^{3+} (1.07 Å). Using viscosity data (range of 20 - 400 Pa*s) from the literature [37], we estimated the diffusion coefficients to be $\sim 1 \times 10^{-7}$ and $\sim 5 \times 10^{-9}$ cm 2 /s for $\text{Na}_2\text{O}/\text{SiO}_2$ co-doped and singly SiO_2 -doped samples, respectively.

Although we can calculate values for grain boundary thickness (δ) and viscosity (η), an exact α -ratio cannot be determined using Equation 2.3 because we do not know the interface reaction constant (K). Nevertheless, assuming a reasonable K value from the literature ($K = 5 \times 10^{-8}$ m/s) [34] and assuming that the A/B ratio (A and B being geometrical factors) is on the order of 1, we estimated α to be $\sim 10^{-2}$ and ~ 1 for singly SiO_2 -doped samples (603 ppm SiO_2) and $\text{Na}_2\text{O}/\text{SiO}_2$ co-doped samples (529/603 ppm), respectively. Thus, we conclude that at 1525°C densification of Bayer aluminas with low $\text{Na}_2\text{O}/\text{SiO}_2$ concentration ratios is governed by diffusion, whereas densification of Bayer aluminas with high $\text{Na}_2\text{O}/\text{SiO}_2$ concentration ratios can be governed by either diffusion or interface reaction.

The enhanced densification of $\text{Na}_2\text{O}/\text{SiO}_2$ co-doped samples compared to singly SiO_2 -doped is attributed to two factors; the increased solubility of Al_2O_3 in the liquid grain boundary phase, and the enhanced diffusion of Al^{3+} ($\sim 5 \times 10^{-9}$ to $\sim 1 \times 10^{-7}$ cm 2 /s) through the liquid grain boundary. This effect of enhanced densification of $\text{Na}_2\text{O}/\text{SiO}_2$ co-doped samples compared to singly SiO_2 -doped samples is observed in both the dilatometry curves and the densification kinetics data shown in Figure 2.2 and Figure 2.6, respectively.

It should be noted that a particular challenge for thermal processing studies with soda-based ceramics is Na_2O volatilization at relatively lower temperature than the sintering temperature. Soda by itself is highly volatile at temperatures

< 1000°C and the evaporation of soda from Na₂O containing technical ceramics such as sodium niobates [38] and β -Al₂O₃ during sintering is often reported. For example, β -Al₂O₃ (Na₂O·11Al₂O₃) has an appreciable Na₂O vapor pressure at temperatures > 1400°C [30], and when heated in air to > 1500°C, β -Al₂O₃ converts to α -Al₂O₃ by volatilization of Na₂O [30, 39]. Therefore, Na₂O evaporation from the samples during heating should be considered as samples might have somewhat lower Na₂O concentrations than assumed for the above calculations. Thus, for samples with low Na₂O:SiO₂ ratios, the liquid grain boundary phase may contain somewhat less Na₂O and the grain boundary thickness may be somewhat less than calculated. However, for singly Na₂O-doped samples and for co-doped samples with high Na₂O:SiO₂ ratios (e.g. Na₂O \geq 529 ppm for samples with 603 ppm SiO₂) the composition of the grain boundary liquid and the grain boundary thickness is not expected to change very much if Na₂O volatilizes. Consequently, even with Na₂O volatilization, the proposed sintering mechanisms do not change. The evaporation of Na₂O from Bayer Al₂O₃ samples will be further discussed in future work.

2.5 Summary

High concentrations of Na₂O in Bayer process Al₂O₃ powders inhibit densification in the initial sintering stage and retard densification up to the final sintering stage compared to powders with low Na₂O concentrations. However, Na₂O shows no adverse effect on the final density after longer hold times (\geq 3 h at 1525°C). The addition of SiO₂ to Bayer process Al₂O₃ powders substantially retards densification, starting at \sim 1250°C, and samples containing as much as 603 ppm SiO₂ are 4% less dense than samples containing 103 ppm SiO₂, even after hold times as long as 8 h at 1525°C. Co-doping with Na₂O and SiO₂ increases densification by 1 - 2.5% relative density relative to singly SiO₂-doped samples. The observed differences in sintering behavior can be explained by a liquid phase sintering model. Diffusion and solubility of Al₂O₃ in the SiO₂-based liquid in the grain boundaries is low at the temperatures used in this study, which explains the substantial retardation of densification by SiO₂. As predicted from the phase diagram Na₂O increases the solubility of Al₂O₃ in the siliceous grain boundary phase. As predicted from viscosity data Na₂O enhances diffusion of Al³⁺ through the liquid grain boundary phase. Both factors contribute to the enhanced densification rates of samples with

high $\text{Na}_2\text{O}/\text{SiO}_2$ ratios compared to samples with low $\text{Na}_2\text{O}/\text{SiO}_2$ ratios.

Table 2.1. Physical and chemical characteristics of the as-received Bayer Al₂O₃ powder used in this study.

BET (m ² /g)	7.4
D ₅₀ (μm)	0.4
D ₉₀ (μm)	1.5
	ICP (ppm)
Al ₂ O ₃	99.96 %
SiO ₂	103
Na ₂ O (total)	29
Fe ₂ O ₃	90
CaO	62
TiO ₂	22
MgO	2

Table 2.2. Calculated compositions and amounts of liquid in as-received, singly doped and co-doped samples at 1525°C ($\alpha = \alpha\text{-Al}_2\text{O}_3$, $\beta = \beta\text{-Al}_2\text{O}_3$, L= liquid, M = mullite).

Global dopant concentration		Global Na ₂ O:SiO ₂ ratio	Na ₂ O:SiO ₂ ratio in Liquid	Composition of liquid (mol %)			Amount of liquid (vol. %)	Stable phases
ppm (wt.)	ppm (mol)			Na ₂ O	SiO ₂	Al ₂ O ₃		
Na ₂ O/SiO ₂	Na ₂ O/SiO ₂							
As-received								
29/103	48/175	0.27	0.25	17.9	63.4	19.7	0.03%	$\alpha + L$
154/103-	253/175-							
1029/103	1693/175	1.45-9.67	0.5	26.1	52.3	21.6	0.03%	$\alpha + L + \beta$
29/603	48/1023	0.05	0.25	16.3	65.3	18.4	0.03%	$\alpha + L + M$
154/603	253/1023	0.25	0.25	16.3	65.3	18.4	0.16%	$\alpha + L$
279/603	459/1023	0.45	0.45	24.5	54.6	20.8	0.19%	$\alpha + L$
529/603	870/1023	0.85	0.5	26.1	52.3	21.6	0.22%	$\alpha + L + \beta$
1029/603	1693/1023	1.65	0.5	26.1	52.3	21.6	0.22%	$\alpha + L + \beta$

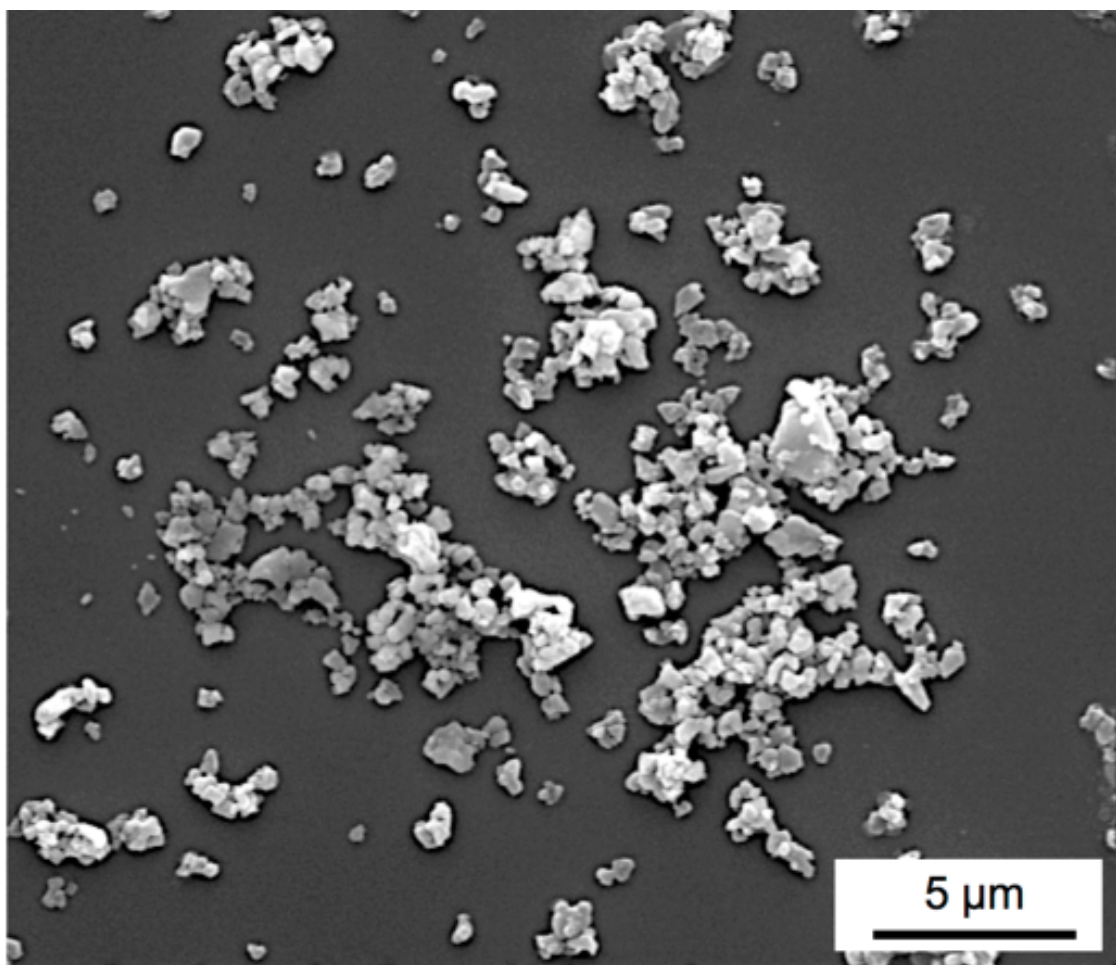


Figure 2.1. SEM image of as-received chemically purified Bayer Al_2O_3 powder used in this study.

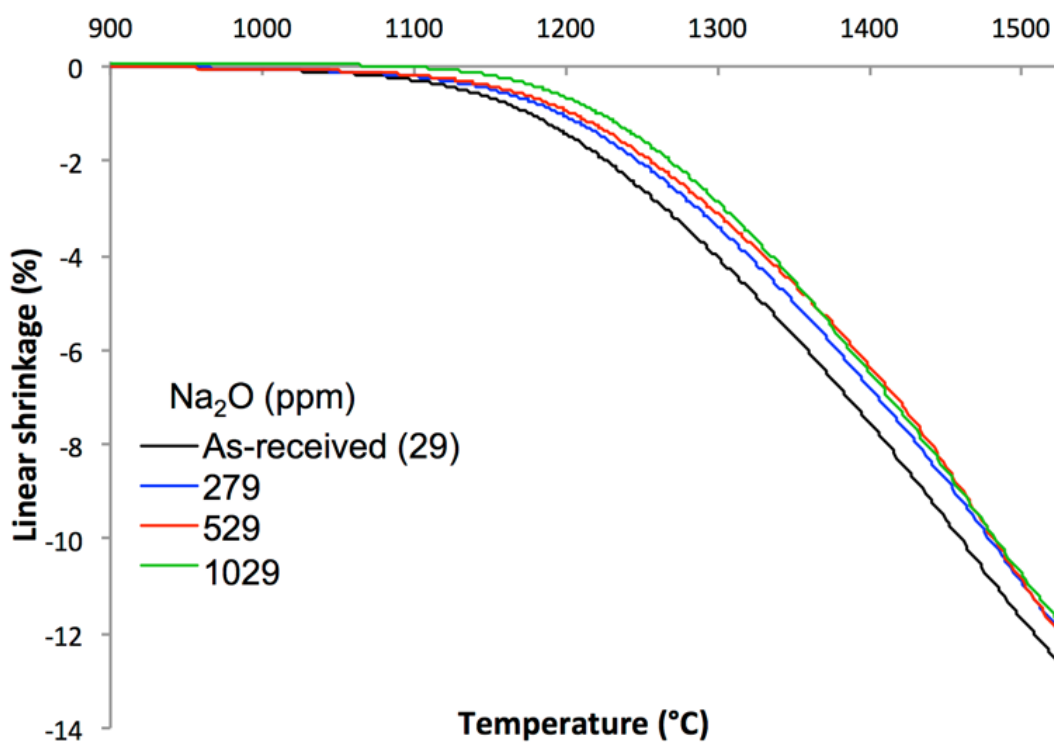


Figure 2.2. Dilatometer curves of as-received and singly Na_2O -doped samples heated at $10^{\circ}\text{C}/\text{min}$ to 1525°C .

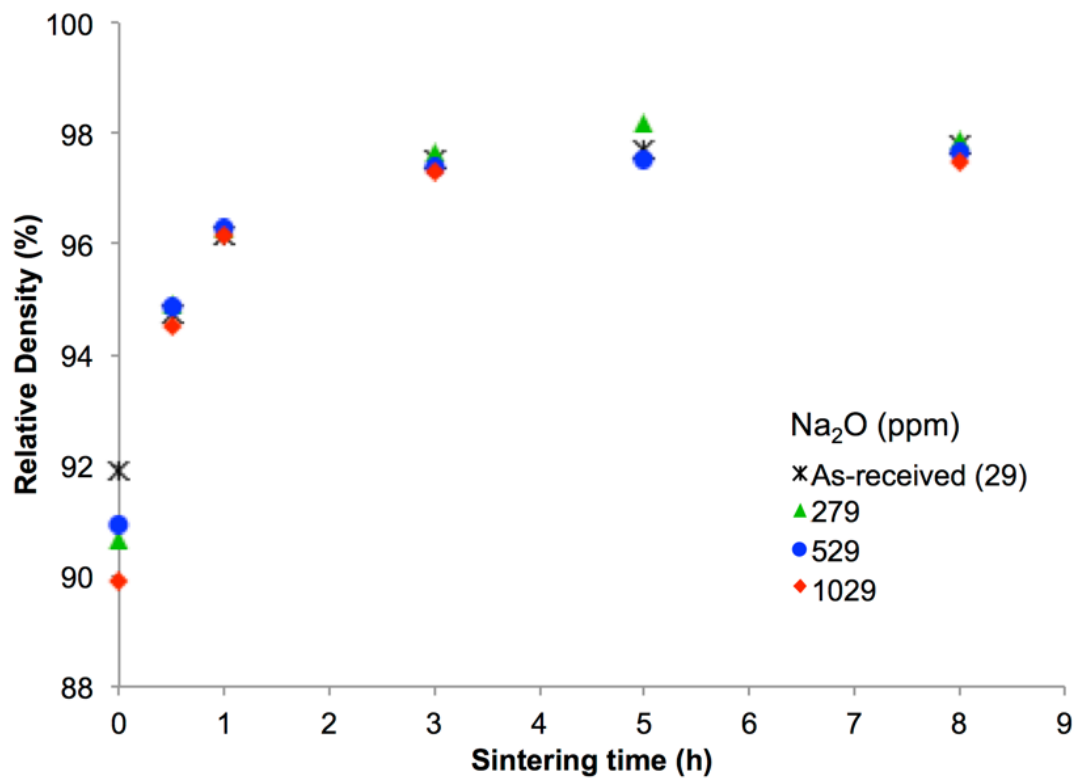


Figure 2.3. Densification kinetics of Bayer Al_2O_3 doped with different Na_2O concentrations and sintered at 1525°C .

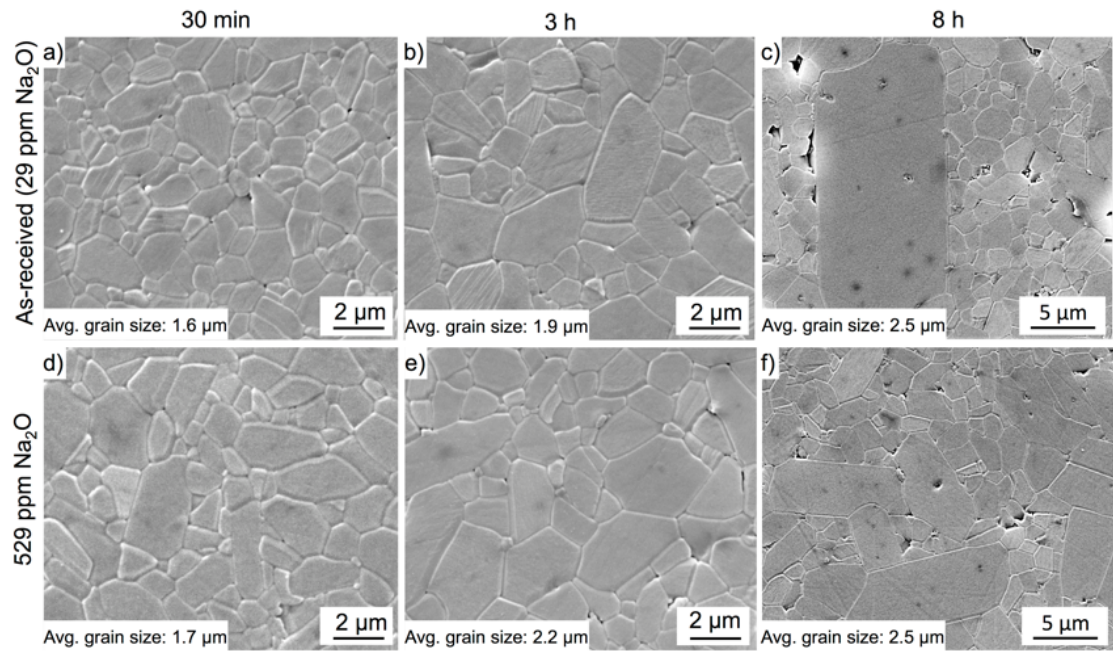


Figure 2.4. Microstructures of as-received and singly 529 ppm Na_2O doped samples after 30 min, 3 h and 8 h at 1525°C.

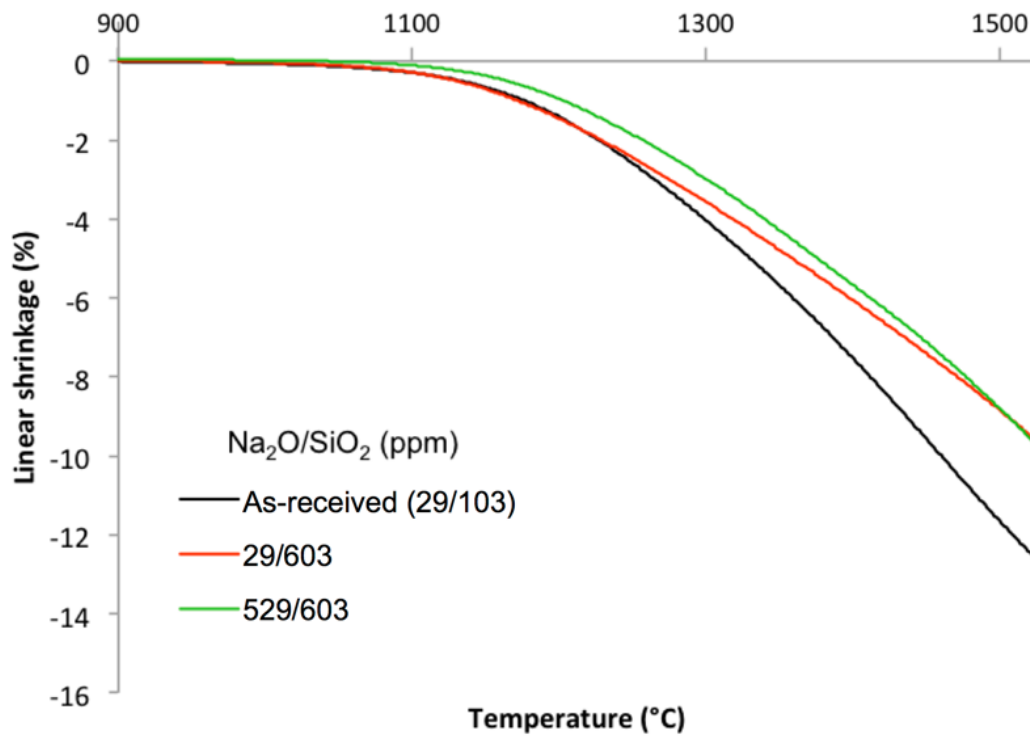


Figure 2.5. Dilatometer curves of as-received, singly SiO₂-doped, and Na₂O/SiO₂-doped Bayer Al₂O₃ heated at 10°C/min to 1525°C.

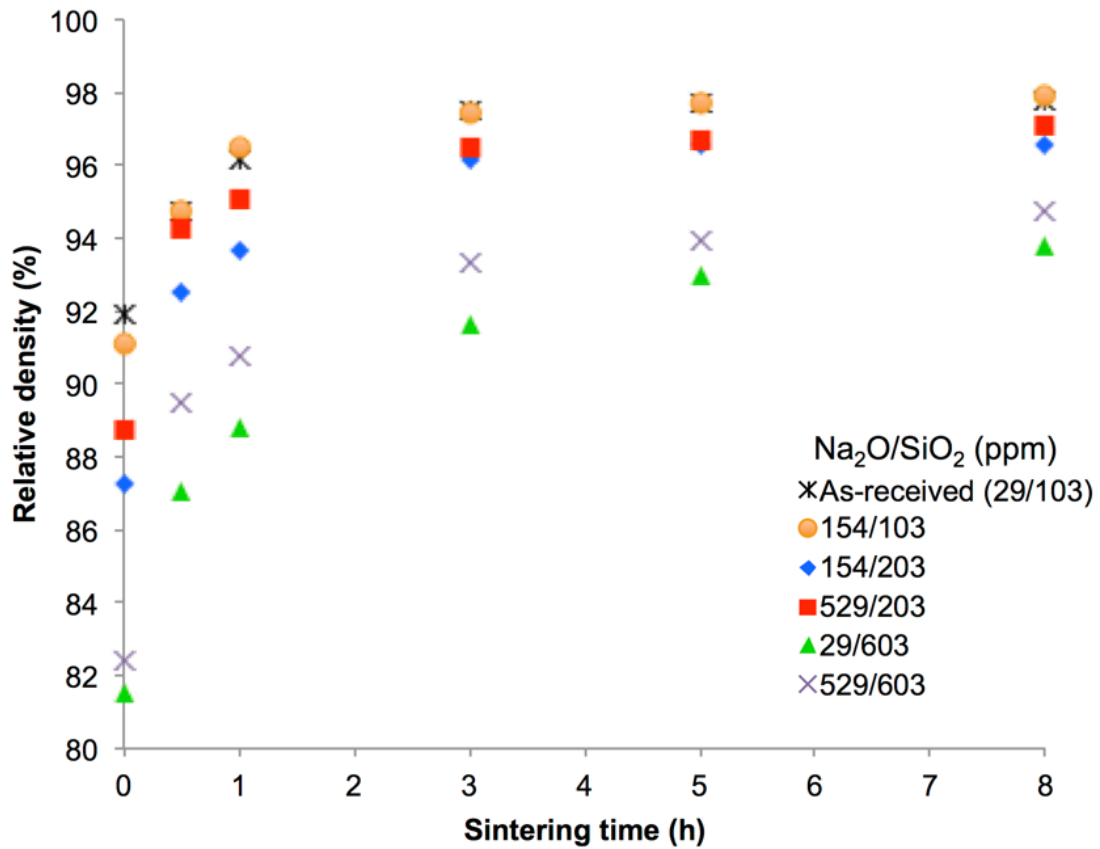


Figure 2.6. Densification kinetics of Bayer Al_2O_3 doped with different concentrations of Na_2O and SiO_2 at 1525°C .

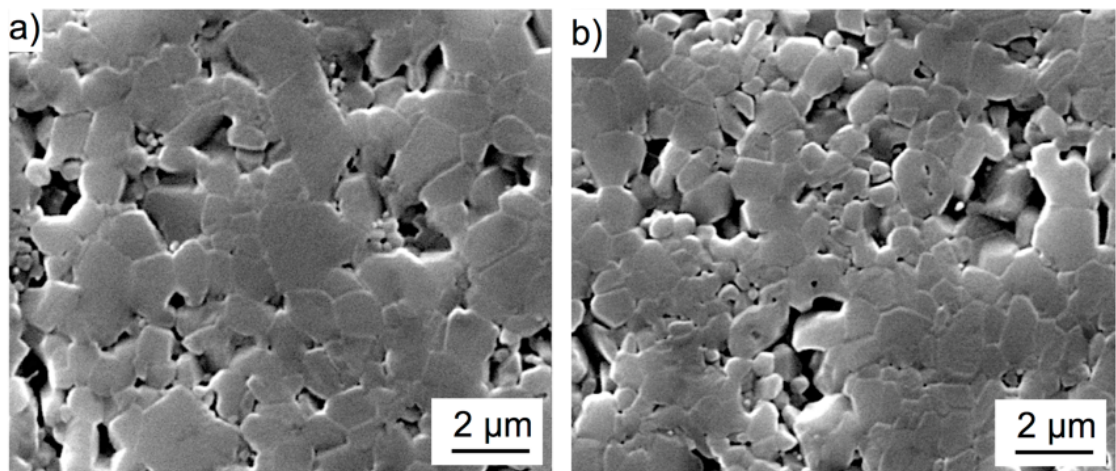


Figure 2.7. Microstructures of Bayer Al_2O_3 doped with a) 603 ppm SiO_2 and b) 529 ppm Na_2O and 603 ppm SiO_2 after heating at 1525°C for 8h.

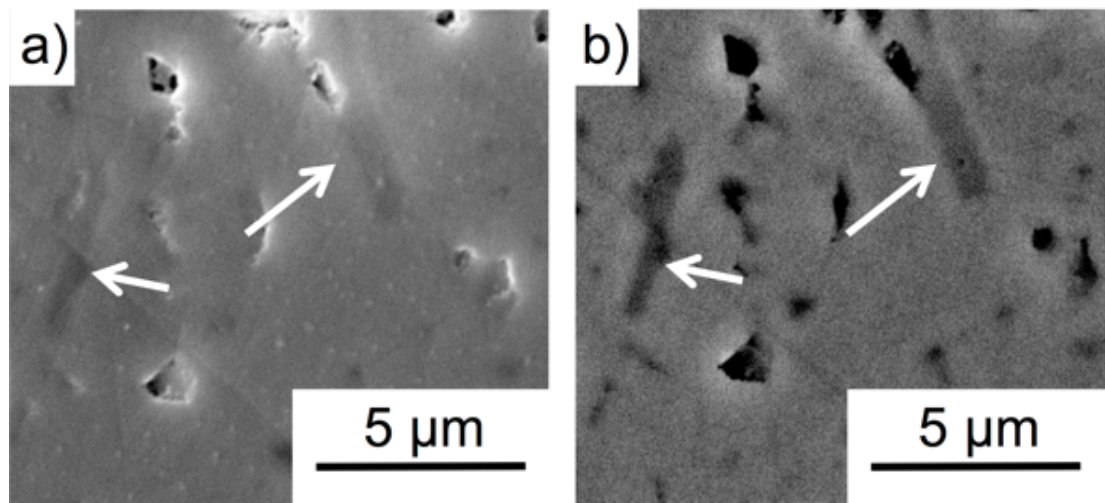


Figure 2.8. Micrographs of a sample doped with 1029 ppm Na_2O after sintering at 1525°C for 3 Åh. The micrographs were recorded using a) a secondary electron detector and b) a backscattered electron detector. The arrows point at the platelet shaped beta alumina grains that form in samples doped with Na_2O . The samples were not thermally etched.

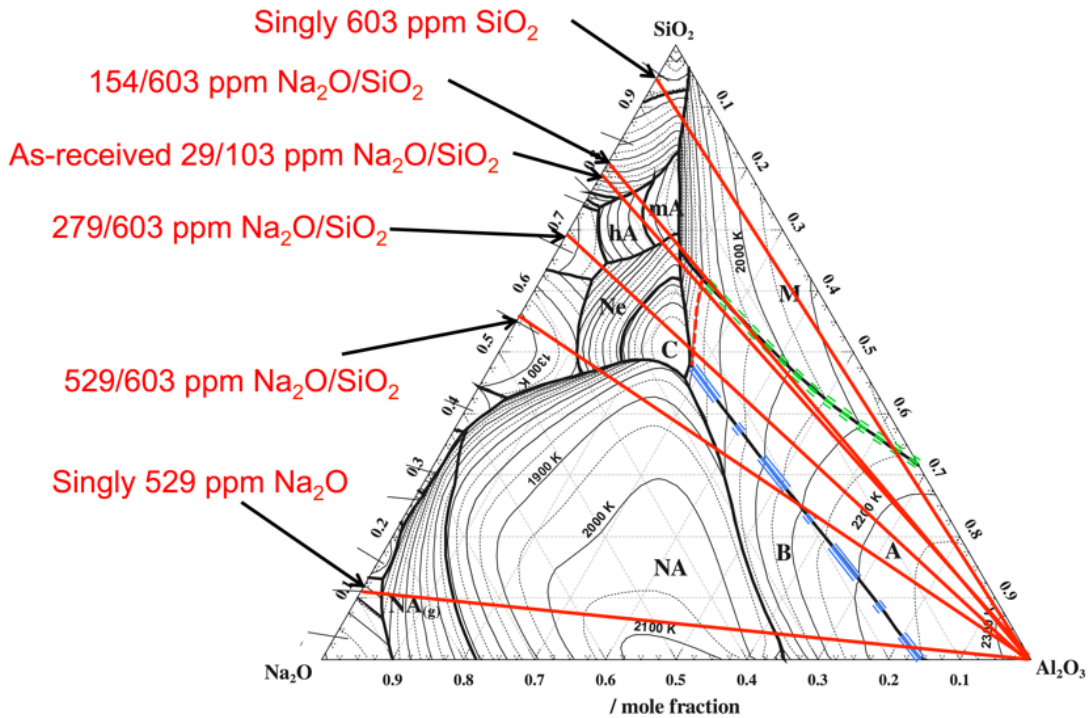


Figure 2.9. Liquidus projection of the Al_2O_3 - SiO_2 - Na_2O ternary phase diagram. The red solid lines are isoplethal cuts representing the samples investigated in this study. The red dashed line is the 1525°C isotherm where $\alpha\text{-Al}_2\text{O}_3$ and liquid are in equilibrium. The blue dash-dot line and green dotted line are eutectic lines at which $\alpha\text{-Al}_2\text{O}_3$ and liquid is in equilibrium with $\beta\text{-Al}_2\text{O}_3$ or mullite, respectively.

Chapter 3 | Powder Chemistry Effects on the Sintering Behavior of MgO- doped Bayer Alumina

3.1 Introduction

Specialty aluminas are generally defined as a calcined or sintered alumina made from a Bayer processed feedstock. These aluminas have specific characteristics to improve their performance in commercial applications, such as defined primary crystal size, surface area, density and shrinkage, and chemical purities in the range of 99.0 - 99.8%. The remaining 1.0 - 0.2% consists of the intentionally added MgO dopant, and impurities such as Na₂O, CaO, Fe₂O₃, and SiO₂ that originate from the bauxite ore or the Bayer process itself. It is well known that trace (ppm) amounts of dopants or impurities can have a significant influence on the sintering of alumina [1, 13, 40]. Since Coble's discovery of MgO doping to produce high-density translucent alumina, there has been high academic and commercial interest in understanding how small concentrations of dopants and impurities characteristic of specialty alumina affect sintering [?, 7, 41–43].

In chapter 2, the influence of Na₂O and SiO₂ on the sintering of MgO-free specialty alumina was investigated [44]. Na₂O was shown to initially retard the densification of MgO-free specialty alumina samples, but no effect was observed after extended sintering time (> 30 min) at 1525°C, whereas the addition of SiO₂ to MgO-free specialty alumina formed a liquid phase and significantly retarded

densification throughout the entire sintering process. Na_2O addition to SiO_2 -doped samples increased the densification rate and degree of densification compared to singly SiO_2 -doped samples. Based on phase equilibria, the solubility of Al_2O_3 in the liquid phase was shown to increase as the Na_2O concentration in the liquid grain boundary phase increases. Furthermore, a higher Na_2O concentration decreases the viscosity of the liquid phase, which further increases the densification rate. Hence, samples with high $\text{Na}_2\text{O}/\text{SiO}_2$ ratios (≥ 0.5) showed higher densities than samples with lower $\text{Na}_2\text{O}/\text{SiO}_2$ ratios.

MgO is commonly added to commercial alumina powders because it is known to improve sintering. Several reasonable mechanistic explanations for the beneficial effect of MgO include solute-drag, particle-pinning, modification of defect chemistry, increase of surface diffusivity, modification of a liquid phase, and modification of interfacial properties [40]. A model that takes into account the redistribution of MgO and SiO_2 during the sintering of high purity alumina was reported by Handwerker et al. [14] They proposed that MgO changes the segregation behavior of glass forming impurities such as SiO_2 by increasing their solubility in Al_2O_3 . This mechanism was supported by the work of Gavrilov et al. [15] who demonstrated by high resolution secondary ion mass spectrometry that the dopants segregate strongly to grain boundaries when high purity Al_2O_3 is singly doped with either SiO_2 or MgO , but show a higher solubility in Al_2O_3 when co-doped with MgO and SiO_2 due to a defect mechanism in which Mg^{2+} and Si^{4+} occupy Al^{3+} sites and compensate for each other's charge and strain. This model is of particular interest since it considers the direct interaction of MgO and SiO_2 ; an impurity known to negatively affect alumina densification.

In this chapter we report how Na_2O and SiO_2 influence the sintering of 99.8 - 99.9% pure specialty alumina doped with 380 ppm MgO . Dilatometry and sintering kinetics of MgO -free specialty alumina samples with similar Na_2O and SiO_2 concentrations from chapter 2 are compared to the present results to identify the stages at which MgO affects densification, and to identify key mechanisms that are responsible for the beneficial effect of MgO on the sintering of specialty alumina [44]. High-resolution transmission electron microscopy (TEM) and energy dispersive spectroscopy (EDS) measurements show the distribution of dopants/impurities on grain boundaries. First-principles calculations based on the density functional theory (DFT) were carried out to estimate the relative thermodynamic stability of

MgO, SiO₂, and MgO+SiO₂ in the alumina lattice.

3.2 Experimental

A chemically purified MgO-doped specialty alumina powder (Almatis, Inc., Leetsdale, PA, USA) was chosen for this study. Earlier we studied the influence of SiO₂ and Na₂O on the sintering of MgO-free specialty alumina using a powder with similar physical and chemical characteristics as the powder used in this study [44]. Since the sample preparation procedures of the two powders were identical, the differences in sintering behavior after doping with similar Na₂O and SiO₂ concentrations should be attributable primarily to the difference in MgO concentration and its cross effects with Na₂O and SiO₂ [44].

Physical and chemical characteristics of the powder are shown in Table 3.1 and Figure 3.1. The powder was doped with up to 1000 ppm Na₂O and 500 ppm SiO₂ using sodium acetate (NaC₂H₃O_{2.3}H₂O, ACS grade, BDH, VWR International LLC, West Chester, PA, USA) and tetraethyl orthosilicate (Si(OC₂H₅)₄), 98%, Aldrich Chemical Company, Inc. Milwaukee, WI, USA), respectively, to obtain chemistries similar to commercial high purity specialty aluminas with different liquid volume fractions and different Na₂O/SiO₂ ratios, as shown in Table 3.2. The detailed doping procedures are described in chapter 2.

Samples with green densities of 59.0 ± 0.5% were fabricated for sintering studies by uniaxial and cold isostatic dry pressing (CIP, Autoclave engineers, Erie, Pa, USA) at 170 MPa and 200 MPa, respectively. The dry pressed cylinders were heated at 10 °C/min to 1525 °C in a thermomechanical analyzer (TMA, Linseis PT1600, Robbinsville, NJ, USA) to record the shrinkage during heating. The kinetics of sintering of samples at 1450 °C and 1525 °C were investigated for up to 8 h. The samples were heated at 10 °C/min to 1200 °C and then at 5 °C/min to the final sintering temperature. The average grain size and density were measured by the linear intercept (ASTM Standard E112-96) [21] and Archimedes methods (ASTM standard B962-15), [20] respectively. The structure and chemistry of grain boundaries were investigated by transmission electron microscopy (TEM) and energy dispersive x-ray spectroscopy EDS using a dual aberration corrected FEI Titan [13] field emission microscope operated at 300 kV and FEI Talos (FEI, Hillsboro, OR, USA) field emission microscope at 200 kV. The EDS on both microscopes is an

FEI Super-X system consisting of four SDDs (Silicon Drift Detectors) with a solid angle of 0.9 sr. The samples for TEM and EDS were air-quenched from the sintering temperature and prepared using a focused ion beam (Quanta 200 3D Dual Beam FIB, FEI, Hillsboro, OR, USA). Grain boundaries were chosen for analysis that were oriented parallel to the TEM beam in order to accurately measure grain boundary widths in the 2D projection images and EDS profiles. Chemical analyses were performed by inductively coupled plasma (ICP) emission spectroscopy (iCap 6000, Thermo Fischer Scientific, Inc., Waltham, MA, USA) after alumina samples were acid digested in a microwave digestion unit equipped with a Teflon sample holder (MARS M, CEM Corp., Matthews, NC, USA).

3.3 Computational Methodology

DFT-based first-principles calculations were carried out at 0 K to investigate the thermodynamic stability of clustered defects in the α -alumina structure. The energy at 0 K without the contribution of the zero-point vibrational energy E_0 was obtained by an equation of state (EOS) fitting using the four-parameter Birch-Murnaghan (BM4) equation as follows [45]:

$$E_0(V) = a + bV^{-\frac{2}{3}} + cV^{-\frac{4}{3}} + dV^{-2} \quad (3.1)$$

where a , b , c , and d are fitting parameters. The EOS fitting is achieved through an energy-volume (E-V) curve of at least 5 different volumes based on the methodology discussed by Shang et al. [45]. The Helmholtz energy $F(V, T)$ can be predicted as a function of temperature T and volume V via [45, 46]:

$$F(V, T) = E_0(V) + F_{vib}(V, T) + F_{T-el}(V, T) \quad (3.2)$$

where F_{vib} is the temperature-dependent vibrational contribution, and F_{T-el} is the thermal electronic contribution. At ambient pressure, the Helmholtz energy of the system is equal to the Gibbs energy.

The vibrational contribution was obtained using the Debye-Grüneisen model [45]:

$$F_{vib}(V, T) = \frac{9}{8}k_B\theta_D(V) - k_BT \left[D \left(\frac{\theta_D(V)}{T} \right) + 3\ln \left(1 - e^{-\theta_D(V)/T} \right) \right] \quad (3.3)$$

where θ_D is the Debye temperature, T the temperature, and $D[\theta_D(V)/T]$ the Debye function. The Debye temperature can be calculated by:

$$\theta_D = s \frac{(6\pi^2)^{\frac{1}{3}} \hbar}{k_B} V_0^{\frac{1}{6}} \left(\frac{B_0}{M} \right)^{\frac{1}{2}} \left(\frac{V_0}{V} \right)^\gamma \quad (3.4)$$

where s is the Debye temperature scaling factor, γ the Grüneisen parameter determined by the pressure derivative of bulk modulus B' , B_0 the equilibrium bulk modulus, M the atomic mass, and V_0 the equilibrium volume. Here, the equilibrium properties V_0 , B_0 , and B' are estimated from the EOS of Eq. 3.1. The methodology by Liu et al. [47] was used to calculate the scaling factor of Al_2O_3 :

$$s(\nu) = 3^{\frac{5}{6}} \left(4\sqrt{2} \left(\frac{1+\nu}{1-\nu} \right)^{\frac{3}{2}} + \left(\frac{1+\nu}{1-\nu} \right)^{\frac{3}{2}} \right)^{-\frac{1}{3}} \quad (3.5)$$

where ν is the Poisson's ratio, which was calculated by Shang et al. [48]. The thermal electronic contribution was estimated based on the electronic density of states and the Fermi-Dirac statistics [46].

In the present work, the Vienna Ab-initio Simulation Package (VASP) was used to perform the first-principles calculations [49]. The projector augmented-wave (PAW) [50, 51] method was utilized to describe the electron-ion interactions with the exchange correlation functional given by the generalized gradient approximation (GGA-PW91) [52]. A sigma value of 0.2 eV and a plane wave energy cutoff of 1.3 times higher than the highest default cutoff were adopted. The Brillouin zone sampling was carried out with Blöchl corrections using a gamma centered Monkhorst-Pack (MP) scheme [51, 53]. The automated k-points grid generator in VASP was employed with a subdivision length of 80. The energy convergence criterion of the electronic self-consistency was set at 10^{-5} eV/atom for all calculations.

The energies of charge, site, and mass balanced defects in α -alumina were calculated for defect clusters, i.e. the defects are located next to each other, since this has been shown to be the most stable configuration [54]. The geometric arrangements of each of the clusters were chosen based on previous computational work. Multiple authors showed that a 30-40 atom supercell of Al_2O_3 is sufficient to calculate non-charged defects [54–58]. Multiple authors have studied charged and clustered defects in Al_2O_3 [54–58]. They showed that different geometric arrangements and supercell size result in little difference in energy and that the

impurity atoms prefer to be clustered due to the binding energy [54–58]. Using this methodology, supercells were generated in the present work with Mg and/or Si clustered, i.e. the Mg-cluster having two Mg atoms substituted for two Al atoms and an oxygen vacancy as nearest neighbors, the Si-cluster having three Si atoms substituted for three Al atoms and an Al vacancy, and the Mg+Si-cluster having one Mg and one Si substituted for two Al atoms.

3.4 Sintering and Microstructure Analysis

In chapter 2, it was shown that a glass phase can form during sintering of specialty alumina. Table 3.2 shows the amounts of liquid in the samples at 1525 °C estimated from the $\text{Al}_2\text{O}_3\text{-Na}_2\text{O}\text{-SiO}_2$ and $\text{Al}_2\text{O}_3\text{-MgO}\text{-SiO}_2$ phase diagrams based on the amount of SiO_2 , Na_2O and MgO [59]. It can be seen that the glass volume fraction increases from 0.03 vol.% for SiO_2 concentrations of 82 ppm to 0.21 vol.% for SiO_2 concentrations of 582 ppm at 1525 °C.

Figure 3.2 shows the dilatometry curves of MgO-doped and MgO-free [44] samples with different Na_2O and SiO_2 concentrations heated at 10 °C/min to 1525°C. For samples with SiO_2 concentrations of 582 ppm the estimated amount of liquid increases from 0.18 vol.% to 0.21 vol.% during heating from 1250 °C to 1525 °C, and for samples with 82 ppm SiO_2 the amount of liquid phase is estimated from the phase diagram to increase from 0.026 vol.% to 0.030 vol.% during heating from 1250 °C to 1525 °C.

Figure 3.2a shows that the onset of densification of MgO-doped specialty alumina is shifted to higher temperatures for samples with higher Na_2O concentrations. Samples with 560 ppm Na_2O shrink 1% less than samples with 60 ppm Na_2O after heating to 1525 °C. In both the MgO-doped and the MgO-free powders, higher SiO_2 concentrations retard densification at ~1250 °C. However, the retardation caused by higher SiO_2 concentrations is less severe in the MgO-doped powder than in the MgO-free powder; e.g. already at 1300 °C, MgO-doped powder samples with 582 ppm SiO_2 (after the addition of 500 ppm SiO_2) shrink 0.2% less and are 0.5% less dense than samples with 82 ppm SiO_2 , whereas samples of the MgO-free powder with 603 ppm SiO_2 shrink 0.5% less and are 3.2% less dense than samples with 103 ppm SiO_2 . After reaching 1525 °C the dilatometry curves show that MgO-doped samples with 582 ppm SiO_2 (0.21 vol.% glass) shrink 1.8% less and

are 5.4% less dense than MgO-doped samples with 82 ppm SiO₂ (0.03 vol.% glass). In contrast, the retardation of densification caused by the addition of 500 ppm SiO₂ to the MgO-free powder results in 3.0% less linear shrinkage and 8.7% lower relative densities after heating to 1525 °C. MgO-doped (380 ppm) powder samples with 560 ppm Na₂O and 582 ppm SiO₂ shrink ~2.5% less than samples with 60 ppm Na₂O and 82 ppm SiO₂ after reaching 1525 °C, and MgO-free powder samples with 529 ppm Na₂O and 603 ppm SiO₂ shrink ~3.0% less than samples with 29 ppm Na₂O and 103 ppm SiO₂ after reaching 1525 °C.

Figure 3.3a and b show how the sintering kinetics of MgO-doped and MgO-free [44] alumina are affected by Na₂O and SiO₂ after heating at 1450 °C and 1525 °C for up to 8 h. The density of samples with higher SiO₂ concentrations, i.e. higher glass concentrations, is lower for all hold times at 1450 °C and 1525 °C. At 1450 °C MgO-doped powder samples with 0.19 vol.% glass phase (582 ppm SiO₂) are 6-7% less dense than samples with 0.027 vol.% glass phase (82 ppm SiO₂), for all hold times (Figure 3.3a). At 1525 °C MgO-doped powder samples with 0.21 vol.% glass phase are ~11% and ~2% less dense than samples with 0.03 vol.% glass phase after heating for 0 h and 8 h, respectively, and samples with 0.03 vol.% glass phase reach densities >98% after 1 h, whereas samples with 0.066 and 0.21 vol.% glass phase are only ~96% and ~94% dense, respectively (Figure 3.3b).

The effect of Na₂O concentration on densification strongly depends on glass phase concentration. In all samples a higher Na₂O concentration initially retards densification. For example, after 0 h at 1450 °C the relative density of samples with 0.03 vol.% glass phase and 560 ppm Na₂O is ~3% lower than the relative density of samples containing the same amount of glass phase and 60 ppm Na₂O. However, there is no difference in sintered density after 3 h at either 1450 °C or 1525 °C. For samples with higher glass phase concentrations (e.g., 0.21 vol.%) the effect of Na₂O on the densification is not straightforward, due to the changing Na₂O/SiO₂ ratio from 0.1 to 0.9 (Table 3.2). Samples with 0.21 vol.% glass phase and Na₂O/SiO₂ ratios of 0.9 are 1-2% denser than samples with 0.21 vol.% glass phase and Na₂O/SiO₂ ratios of 0.1. However, after 30 min at 1525 °C the relative density of samples with 0.21 vol.% glass phase and Na₂O/SiO₂ ratios of 0.9 in the glass phase is 0.9% lower than the relative density of samples with 0.21 vol.% glass phase and Na₂O/SiO₂ ratios of 0.1 in the glass phase, and after 1 h or longer at 1525 °C there is no difference in relative density. Samples with 0.066 vol.% glass

phase are 98.3 - 98.6% dense after 8 h at 1525 °C, and samples with 0.21 vol.% glass phase are 97.1% - 97.5% dense after 8 h at 1525 °C.

Comparing the as-received MgO-free and MgO-doped powders with 0.03 vol.% glass phase shows that doping with 380 ppm MgO leads to 1% higher densities for all hold times at 1525 °C (Figure 3.3b and c) [44]. After 8 h at 1525 °C the MgO-doped samples with 0.21 vol.% glass phase are ~2% less dense than samples with 0.03 vol.% glass phase, whereas the addition of 500 ppm SiO₂ (total of 603 ppm SiO₂ and 0.22 vol.% glass) to the MgO-free powder leads to ~4% less dense samples [44]. MgO-free and MgO-doped specialty alumina samples containing 0.22 and 0.21 vol.% glass phase, respectively, and global Na₂O/SiO₂ ratios of 0.9 show initial retardation of densification compared to samples with Na₂O/SiO₂ ratios of 0.1, but have higher densities than samples with Na₂O/SiO₂ ratios of 0.1 after further heating. This increased densification can be explained by the increased solubility of Al₂O₃ into the liquid grain boundary phase and the higher diffusivity (lower viscosity of the grain boundary phase) as the Na₂O/SiO₂ ratio increases [34, 44]. However, after hold times of 1 h or longer at 1525 °C, MgO-free powder samples with 0.22 vol.% glass phase and Na₂O/SiO₂ ratios of 0.9 are 1% denser than samples with 0.22 vol.% glass phase and Na₂O/SiO₂ ratios of 0.1, whereas MgO-doped powder samples with 0.21 vol.% and Na₂O/SiO₂ ratios of 0.9 have the same densities as samples with 0.21 vol.% glass phase and Na₂O/SiO₂ ratios of 0.1.

The microstructures of samples with different vol.% glass phase and different Na₂O/SiO₂ ratios heated at 1525 °C for 8 h are shown in Figure 3.4. Samples with 60 ppm Na₂O show mostly equiaxed grains, regardless of the glass phase concentration in the samples (Figures 3.4a and c). Samples with 560 ppm Na₂O (Figures 3.4b and d) show more faceted α-Al₂O₃ grains and appear to have a wider grain size distribution than samples with 60 ppm Na₂O. These effects are more pronounced in samples with higher glass concentrations. The grain sizes of samples with 0.21 vol.% glass are less than the grain sizes of samples with 0.03 vol.% glass phase.

The average grain sizes of samples with different vol.% glass phase and different Na₂O/SiO₂ ratios are plotted as a function of relative density in Figure 3.5. Grain growth starts when the final sintering stage is reached, between 85 and 92% relative density. Samples with 0.03 vol.% glass phase and 60 ppm Na₂O show a three-fold

increase in grain size, from $0.5 \mu\text{m}$ to $\sim 1.5 \mu\text{m}$, when the relative density increases from 68% to 99%, and samples with 0.03 vol.% glass phase and 560 ppm Na_2O have a somewhat larger grain size of $2.2 \mu\text{m}$ at 99% relative density. When relative densities of $\sim 99\%$ are reached in samples with 0.03 vol.% glass, the grain size increases to $3.1 - 3.4 \mu\text{m}$ when heated at 1525°C for 8 h. Samples with higher glass concentrations have a similar trajectory up to 92% density. However, at densities $>92\%$ grain growth is enhanced in samples with higher glass concentrations, and at 97 - 97.5% density higher glass phase concentrations of 0.21 and 0.17 vol.% lead to a larger grain size of 2.6 and $2.4 \mu\text{m}$, respectively, compared to samples with 0.03 vol.% glass phase ($\sim 1.5 \mu\text{m}$ grain size).

3.5 Mechanistic Interpretation

If the mechanism of MgO increasing the solubility of SiO_2 in alumina, as proposed by Handwerker et al., [14] is responsible for the improved sintering behavior of alumina, then the amount of liquid phase in MgO -doped alumina should be less than calculated and less than in MgO -free samples, and, the grain boundary thickness in MgO -doped alumina should be less than in MgO -free powder. The reduced grain boundary thickness in MgO -doped alumina should lead to a change in grain boundary chemistry and different sintering behavior after this co-dissolution has occurred compared to MgO -free alumina.

Comparing the dilatometry curves and sintering kinetics of MgO -doped and MgO -free specialty alumina powders with different chemistries indicates that there are two stages at which MgO affects densification. At 1250°C increased glass phase content retards densification, and at the same stage there is an enhancement of densification due to MgO . This suggests that there is a direct interaction between the glass phase and MgO at this stage, where MgO mitigates the negative effect of the glass phase, probably by modifying the properties of the liquid grain boundary phase. The Al_2O_3 - SiO_2 - MgO phase diagram suggests that MgO increases the solubility of Al_2O_3 in the liquid, and MgO can lower the viscosity of the glass melt, [37] which results in higher diffusion coefficients. The enhanced diffusion associated with the lower viscosity and higher solubility of Al_2O_3 in the glass phase can explain why MgO positively affects the sintering of alumina at stages when SiO_2 would negatively affect densification.

The second stage at which MgO affects densification is after 1 h at 1525 °C. MgO-free powder samples with 0.22 vol.% glass phase and Na₂O/SiO₂ ratios of 0.9 have 1-2% higher relative densities than samples with 0.22 vol.% glass phase and Na₂O/SiO₂ ratios of 0.1 for all hold times at 1525 °C. In previous work we calculated an expected grain boundary thickness of 1.3 nm for samples with 0.22 vol.% glass phase after 3 h at 1525 °C, based on the observed grain size of 1.6 μm. The addition of 500 ppm Na₂O increases the Na₂O/SiO₂ ratio from 0.1 to 0.9, which modifies the liquid grain boundary phase and enhances densification [44]. Figure 3.6 shows a high-resolution TEM image of a grain boundary of a MgO-free powder [44] sample (2 ppm MgO) with 0.22 vol.% glass phase and a Na₂O/SiO₂ ratio of 0.9 after 3 h at 1525 °C. It can be seen that the measured grain boundary thickness of 1.7 nm is close to the grain boundary thickness calculated based on the amount of glass phase in the sample. MgO-doped powder samples with 0.21 vol.% glass phase and Na₂O/SiO₂ ratios of 0.9 have 1-2% higher densities than samples with 0.21 vol.% glass phase and Na₂O/SiO₂ ratios of 0.1 for most hold times at 1450 °C and for hold times < 30 min at 1525 °C. This difference in densification behavior is similar to the densification behavior of MgO-free powder samples, which suggests the presence of a liquid phase that is modified by Na₂O, as seen in the MgO-free alumina samples.

Figure 3.7a shows a high resolution TEM image of a grain boundary in an MgO-doped alumina sample with 0.21 vol.% glass phase and a Na₂O/SiO₂ ratio of 0.9 after 0 h at 1525 °C. The measured grain boundary thickness of ~1.4 nm for this sample is in agreement with the theoretically estimated [44] grain boundary thickness. However, after 1 h or longer at 1525 °C, samples with 0.21 vol.% glass and Na₂O/SiO₂ ratios of 0.9 have the same densities as samples with 0.21 vol.% glass and Na₂O/SiO₂ ratios of 0.1, and the grain boundary thicknesses of those samples after 3 h at 1525 °C are ~0.3 nm (Figure 2.7b) and substantially thinner than the calculated grain boundary thicknesses of 1.4 nm.

The thinner grain boundary suggests that the addition of MgO causes a reduction of the amount of liquid phase in the grain boundaries after longer time at 1525 °C. In the literature it is reported that excess liquid phase, after an equilibrium grain boundary thickness [60] is reached, can accumulate in triple pockets. However, we did not observe any triple pockets in the 380 ppm MgO-doped samples with 0.21 vol.% glass. Therefore, the impurities and dopants that formed the liquid

phase after 0 h have to be distributed elsewhere in the sample after 3 h at 1525 °C. Since SiO_2 -containing second phases, such as mullite or cordierite, were not observed in the samples, we hypothesize that SiO_2 and MgO form a solid solution in α -alumina, as proposed by Handwerker et al. [14]. This co-dissolution mechanism would significantly reduce the total amount of SiO_2 and, therefore, the liquid phase content in the samples and in the grain boundaries.

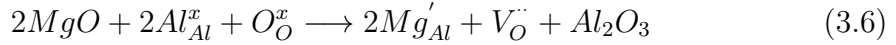
The EDS maps in Figure 2.8 show the distribution of Si around a grain boundary in MgO -doped samples with a calculated glass concentration of 0.21 vol.% after 0 h and 3 h at 1525 °C. Figure 2.9 shows the corresponding EDS line scans for Si and Mg across the grain boundaries. It can be seen that after 0 h at 1525 °C SiO_2 and MgO are strongly concentrated in the grain boundaries, and a chemical grain boundary thickness, δ_{chem} , of ~ 1.7 nm is estimated (Figures 2.8a and 2.9a), which is close to the structural grain boundary thickness of 1.4 nm measured from the high resolution TEM image (Figure 2.7a). After 3 h at 1525 °C MgO and SiO_2 are still concentrated on the grain boundary, however, the chemical grain boundary thickness, δ_{chem} , is ~ 3.2 nm (Figure 2.8b and 2.9b) and substantially thicker than the observed structural grain boundary thickness, δ_{str} , of ~ 0.3 nm (Figure 2.7b). This difference in structural and chemical grain boundary thickness after 3 h supports the argument that MgO and SiO_2 form a solid solution in the alumina lattice in the near grain boundary region. If we assume that equal amounts of MgO and SiO_2 dissolve into the alumina lattice to form the proposed defect complex, and that all MgO in the sample is consumed by this process, then 380 ppm SiO_2 must be removed from the amorphous grain boundary phase. This would leave 202 ppm SiO_2 in the grain boundaries to form the amorphous film with a calculated grain boundary thickness of 0.5 nm, which is close to the observed grain boundary thickness of 0.3 nm [44].

To further evaluate whether MgO and SiO_2 form a solid solution in α -alumina we conducted first-principles calculations based on density functional theory to gain insight into the thermodynamic stability of Mg^{2+} and Si^{4+} by themselves and together in the α -alumina structure. To ensure the accuracy of the calculations, the lattice parameters and energy of the α -alumina structure without any substitutions are compared with previous experiments and calculations in Table 3.3. It can be seen that the calculated lattice parameters match well with experimental values and lattice parameters from previous first-principles calculations [54, 61–65]. The

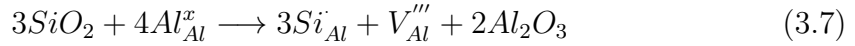
difference between the present and past first-principles calculations can be attributed to the different input parameters used.

We calculated the energy of a unit cell of the $\hat{\text{I}}$ -alumina structure with substitutions according to the following balanced equations:

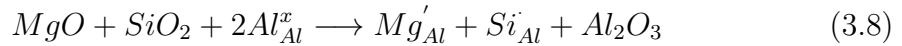
Mg-Cluster:



Si-Cluster:



Mg+Si-Cluster:



Defect simulations of aliovalent cation substitutions in alumina [54] showed that the dominant compensation mechanisms for Mg^{2+} and Si^{4+} by themselves in alumina are the formation of oxygen and aluminum vacancies, respectively (Eq.3.6 and 3.7). In Eq. 3.8 Mg^{2+} and Si^{4+} compensate for each other's charge and the formation of vacancies or interstitials is unnecessary to account for dissolution in the alumina lattice. The calculations were carried out for clustered defects since they are lower in energy than isolated defects [54]. The structures were relaxed and the formation energies as a function of temperature with bulk Al_2O_3 as the reference state are plotted in Figure 3.10. It can be seen that the formation energy for the Mg+Si-cluster, $E_{\text{Form}}^{\text{Mg+Si}}$, is lower than the formation energies of the Mg-cluster, $E_{\text{Form}}^{\text{Mg}}$, and the Si-cluster, $E_{\text{Form}}^{\text{Si}}$, which indicates that the Mg+Si-cluster is more stable than the Mg-cluster and the Si-cluster. Since two Mg^{2+} ions and three Si^{4+} ions are necessary to form the Mg-cluster and Si-cluster, respectively, but only one Mg^{2+} and one Si^{4+} are required to form the Mg+Si-cluster, the formation energies of the clusters can be compared by

$$\Delta E_{\text{Form}} = E_{\text{Form}}^{\text{Mg+Si}} - \left(\frac{1}{3}E_{\text{Form}}^{\text{Si}} + \frac{1}{2}E_{\text{Form}}^{\text{Mg}} \right) \quad (3.9)$$

The formation energy difference, ΔE_{Form} , is plotted in Figure 3.10 and it can be

seen that ΔE_{Form} is negative at all temperatures, which means that the Mg+Si-cluster is more energetically favored to form than the Mg-cluster or Si-cluster. This indicates that MgO and SiO₂ have a higher co-solubility in α -alumina than MgO or SiO₂ by themselves. In α -alumina the Al³⁺ cation sites are 6-fold coordinated and Al³⁺ has an effective ionic radius of 53.5 pm, while the radii of Mg²⁺ and Si⁴⁺ are 72 pm and 40 pm, respectively. Therefore, Mg²⁺ and Si⁴⁺ can compensate for each other's size and charge difference relative to Al³⁺ in the α -alumina lattice, which explains the lower energy of the Mg+Si-cluster. The stable phases for MgO and/or SiO₂ and Al₂O₃ are spinel, cordierite, and mullite. However, we hypothesize that if both MgO and SiO₂ are present at low concentrations, then it is more favorable for MgO and SiO₂ to form a solid solution in the α -alumina structure than to form a second phase or remain in the grain boundaries as a siliceous liquid phase.

The described mechanism could also influence the distribution of other oxides in the samples, such as Fe₂O₃, CaO, and Na₂O. Figure 3.11 shows the element distribution obtained from EDS of two grain boundaries in samples sintered at 1525 °C for 0 h and 3 h, respectively. Figures 3.11a and e show the segregation of MgO to the grain boundaries after 0 h and 3 h, respectively, and it can be seen that after 0 h at 1525 °C Mg is more strongly concentrated in the grain boundary than after 3 h at 1525 °C, due to the mechanism described above. From Figures 3.11b and f it can be seen that there is no segregation of Fe₂O₃ and we believe that Fe₂O₃ is in solid solution in the alumina lattice, [54] since the Al₂O₃-Fe₂O₃ phase diagram shows considerable solubility [66]. Figures 3.11c, d, g, and h show that there is a slightly higher Na and Ca signal coming from the grain boundaries, indicating that Na and Ca segregate to the grain boundaries and are components of the liquid grain boundary phase. Ca is more concentrated in the grain boundary after 3 h at 1525 °C, due to the narrower grain boundary thickness (Figure 3.7b).

It can be seen that the Na signal after 0 h at 1525 °C (Figure 3.11c) shows a slight segregation of Na to the grain boundary, but after 3 h at 1525 °C (Figure 3.11g) no segregation can be observed. It should also be noted that it is challenging to detect Na using EDS since the Na signal disappears quickly after the high-voltage electron beam is focused on the grain boundary. Therefore, we believe that there is still Na on the grain boundaries, even though the EDS map does not show an increased Na signal. However, since the Na signal is lower, we believe that after 3 h at 1525 °C there is less Na₂O on the grain boundaries than after 0 h at 1525 °C. The

reduced amount of Na might be a result of volatilization of Na_2O during sintering. Figure 3.12 shows the influence of sintering time and temperature on the Na_2O concentration, obtained by ICP analysis, during sintering for samples with target concentrations of 560 ppm Na_2O . It can be seen that there is no observable Na_2O loss as a function of temperature up to 1525 °C (Figure 3.12a), but after heating to 1600 °C there is a loss of ~200 ppm or a ~35% decrease in Na_2O concentration. After sintering at 1525 °C for 30 min the Na_2O concentration decreases by about 200 ppm, but remains constant at ~350 ppm when heated to 1525 °C for up to 8 h (Figure 3.12b). Between 1300 °C and 1525 °C the Na_2O concentration is constant at ~510 ppm, which is 50 ppm below the target level. The lower Na_2O concentration might be due to volatilization at earlier stages. During heating at 1525 °C Na_2O loss can be observed between 0 and 30 min hold time, which can explain the lower Na signal in Figure 3.11g.

As explained earlier, the described dissolution of MgO and SiO_2 into the alumina lattice reduces the amount of glass phase in the grain boundaries. Since only SiO_2 is removed from the glass phase and other components of the glass phase, such as CaO and Na_2O remain, the grain boundaries can supersaturate. This can eventually lead to the nucleation of second phases, which was observed for samples with lower SiO_2 concentrations of 82 and 182 ppm.

3.6 Summary and Conclusion

The effect of MgO on the sintering of specialty alumina powders with different chemistries was analyzed by comparing the sintering kinetics of MgO -free and MgO -doped specialty aluminas with different impurity levels and ratios of Na_2O and SiO_2 . TEM images of grain boundaries shows that the grain boundary thickness of MgO -doped specialty alumina is reduced during densification at 1525 °C and are thinner than observed in MgO -free specialty alumina. EDS analysis suggests that MgO and SiO_2 have an increased co-solubility in the alumina lattice when present together. This co-dissolution mechanism was supported by DFT-based first-principles calculations showing that the formation energy of MgO and SiO_2 together in the alumina lattice is lower than the formation energies of MgO or SiO_2 by themselves in the alumina lattice. The reduced amount of SiO_2 on the grain boundaries of MgO -doped alumina leads to enhanced densification compared to

MgO-free alumina because SiO_2 has been shown to retard densification.

The present study supports the hypothesis of Handwerker et al. [14] and high resolution SIMS observations of Gavrilov et al. [15] that the key mechanism responsible for the beneficial effect of MgO on the sintering of alumina is the reduction of amorphous phase in the grain boundaries by increasing the solubility of SiO_2 in the alumina lattice.

Table 3.1. Physical and chemical characteristics of the as-received 380 ppm MgO-doped specialty alumina powder used in this study.

BET (m^2/g)	7.3
D_{50} (μm)	0.4
D_{90} (μm)	1.4
	ICP (ppm)
Al_2O_3	99.92 %
SiO_2	82
Na_2O	60
Fe_2O_3	140
CaO	51
TiO_2	8
MgO	380

Table 3.2. Calculated compositions and amounts of liquid in 380 ppm MgO-doped specialty alumina samples of different chemistries at 1450°C and 1525 °C.

Na ₂ O/SiO ₂ concentration		Global Na ₂ O/SiO ₂ ratio	Na ₂ O:SiO ₂ ratio in the liquid	Vol. % of liquid in sample	
ppm by wt.	ppm by mole			1450 °C	1525 °C
60/82 - 560/82	99/139 - 921/139	0.7 - 6.6	0.5	0.027	0.030
185/182 - 560/182	304/309 - 921/309	1.0 - 3.0	0.5	0.060	0.066
60/582	99/987	0.1	0.1	0.19	0.21
560/582	921/987	0.9	0.5	0.19	0.21

Table 3.3. Lattice parameters and equilibrium energy (E_0) compared to previous first-principles and experimental values.

Reference	E_0 (eV/atom)	a (Å)	b (Å)	c (Å)
This work	-7.48	4.76	4.76	12.99
Calc [61–65]	-7.48	4.78	4.78	13.00
Expt [54]		4.76	4.76	13.00

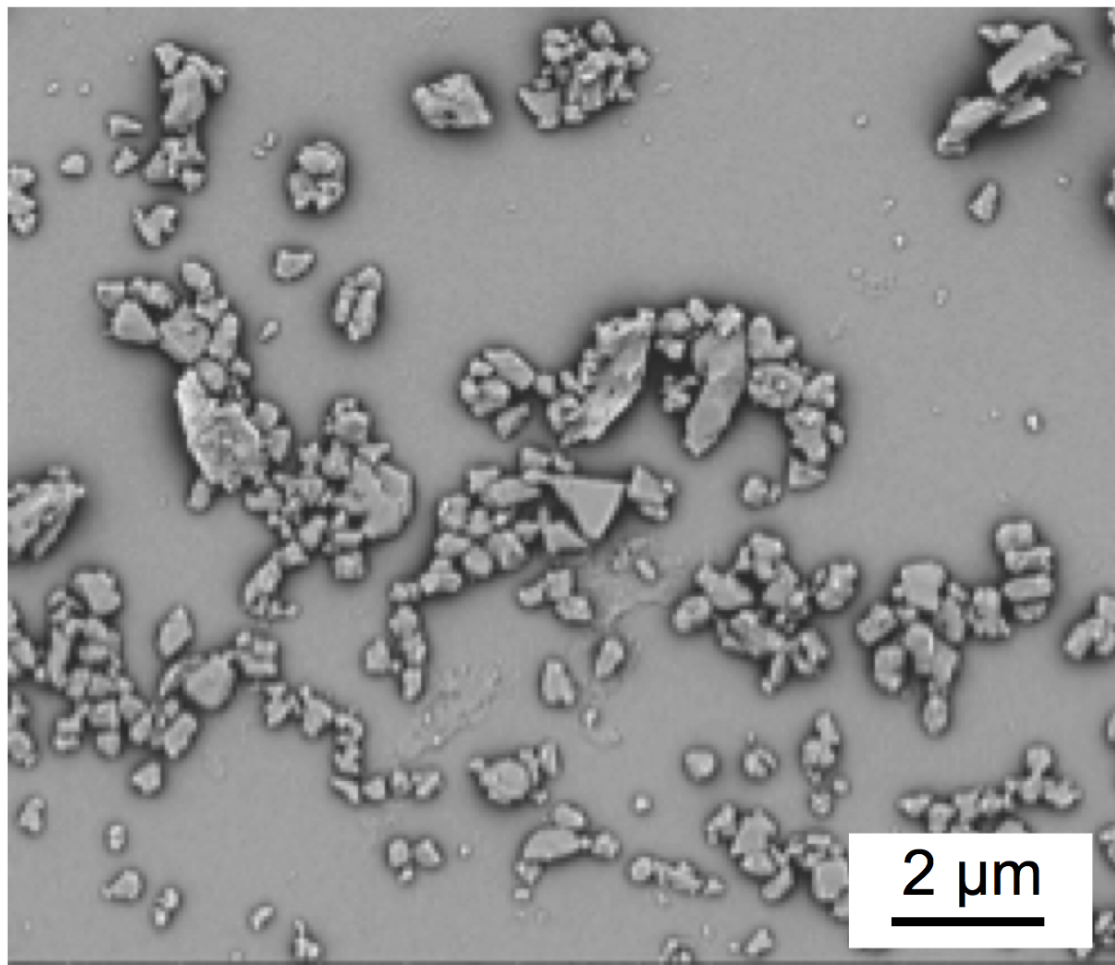


Figure 3.1. SEM image of 380 ppm MgO-doped specialty alumina powder used in this work.

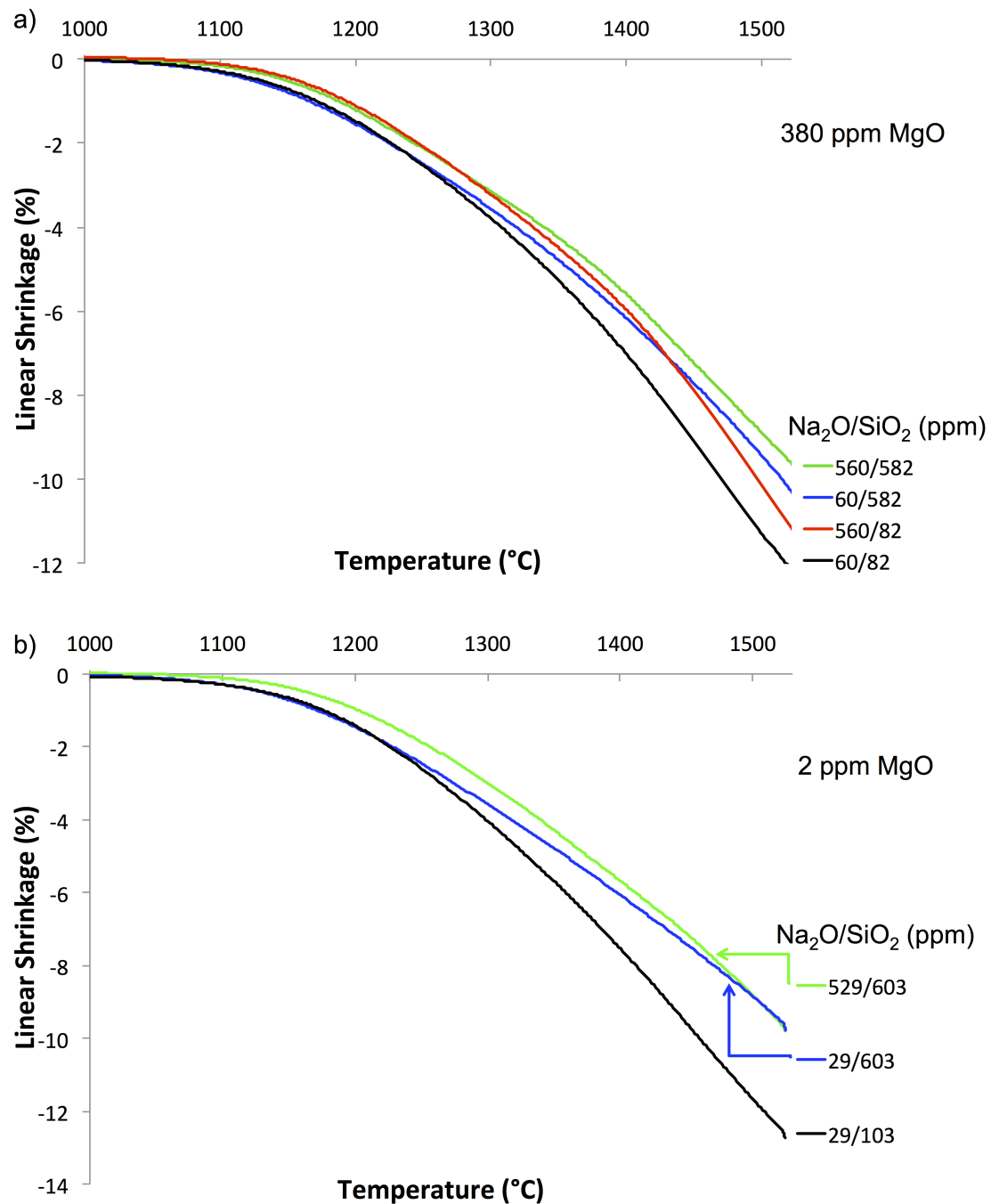


Figure 3.2. Dilatometer curves of a) 380 ppm MgO-doped and b) MgO-free [1] specialty alumina samples with different $\text{Na}_2\text{O}/\text{SiO}_2$ levels heated at 10°C/min to 1525°C.

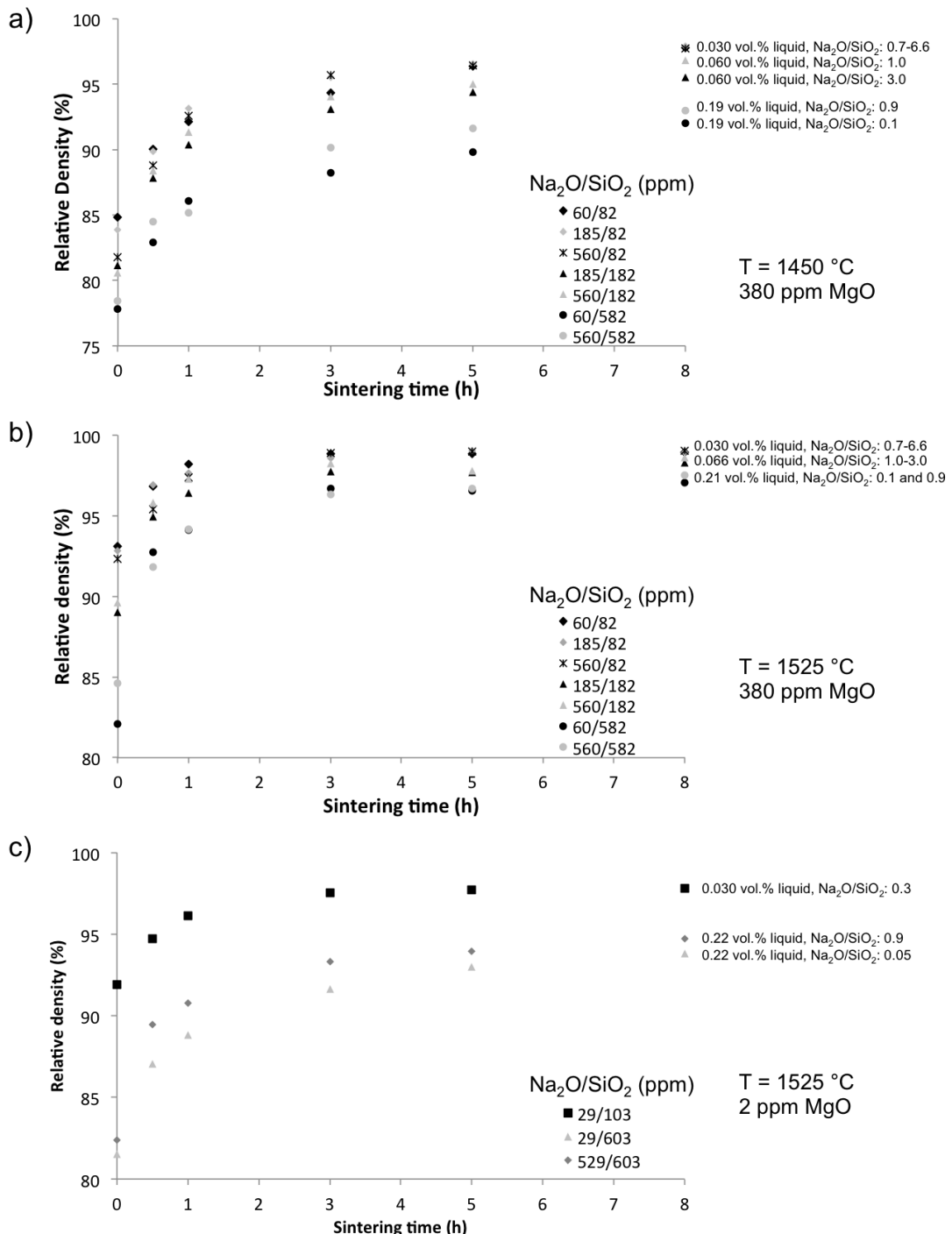


Figure 3.3. Densification kinetics of specialty processed alumina containing different amounts Na_2O and SiO_2 and a) 380 ppm MgO sintered at 1450°C , b) 380 ppm MgO sintered at 1525°C , and c) 2 ppm MgO sintered at 1525°C [1].

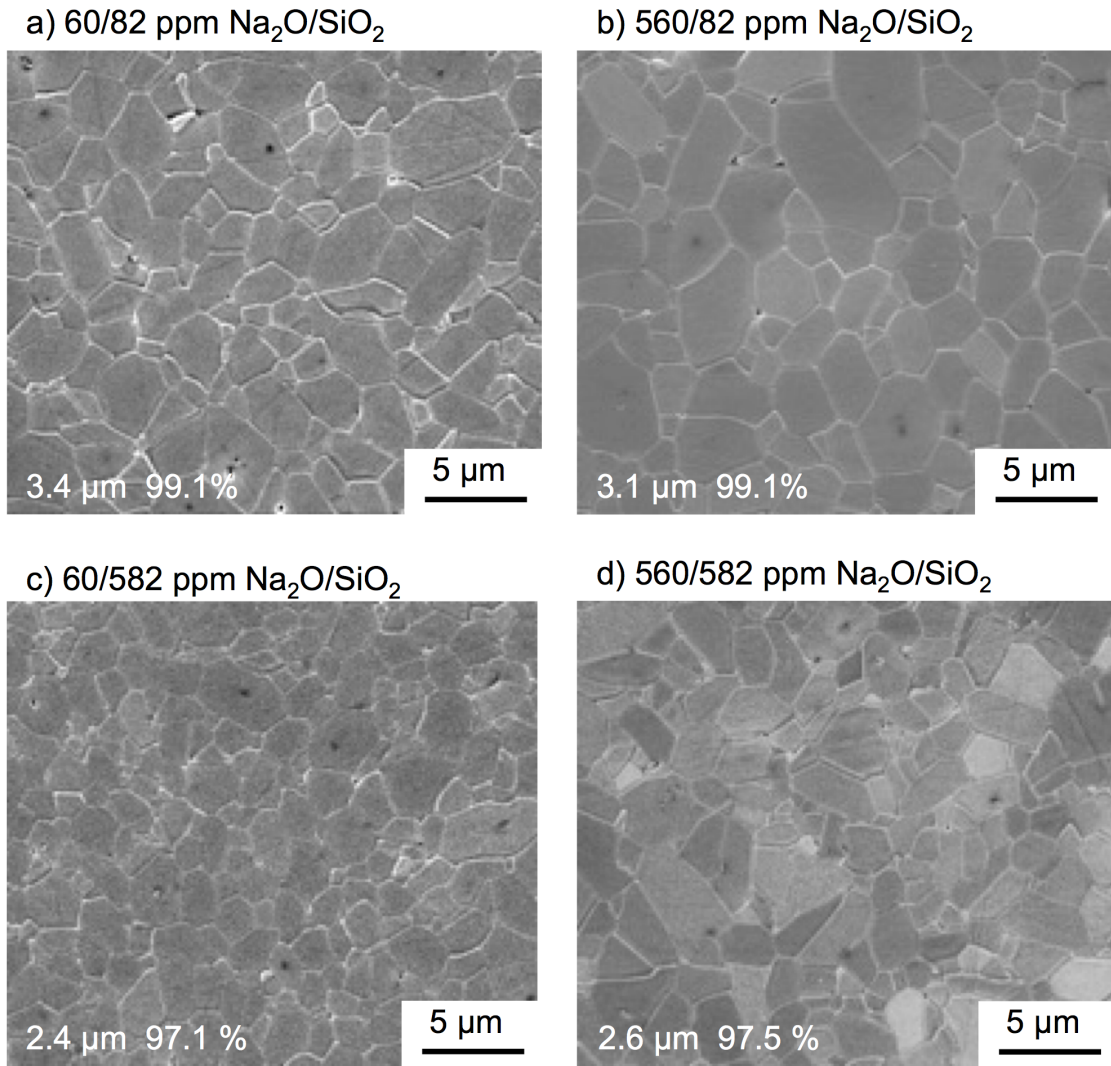


Figure 3.4. Microstructures of 380 ppm MgO-doped specialty alumina samples with different Na_2O and SiO_2 concentrations sintered at 1525°C for 8 h.

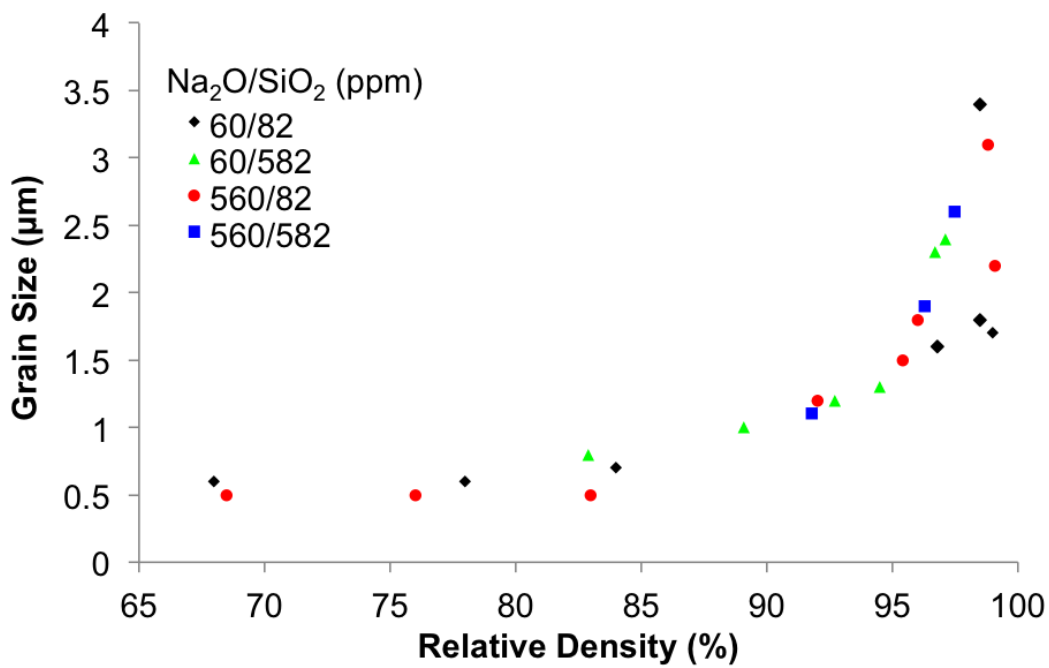


Figure 3.5. Sintering trajectories (grain size vs. relative density) for 380 ppm MgO-doped specialty alumina samples with different Na₂O and SiO₂ concentrations.

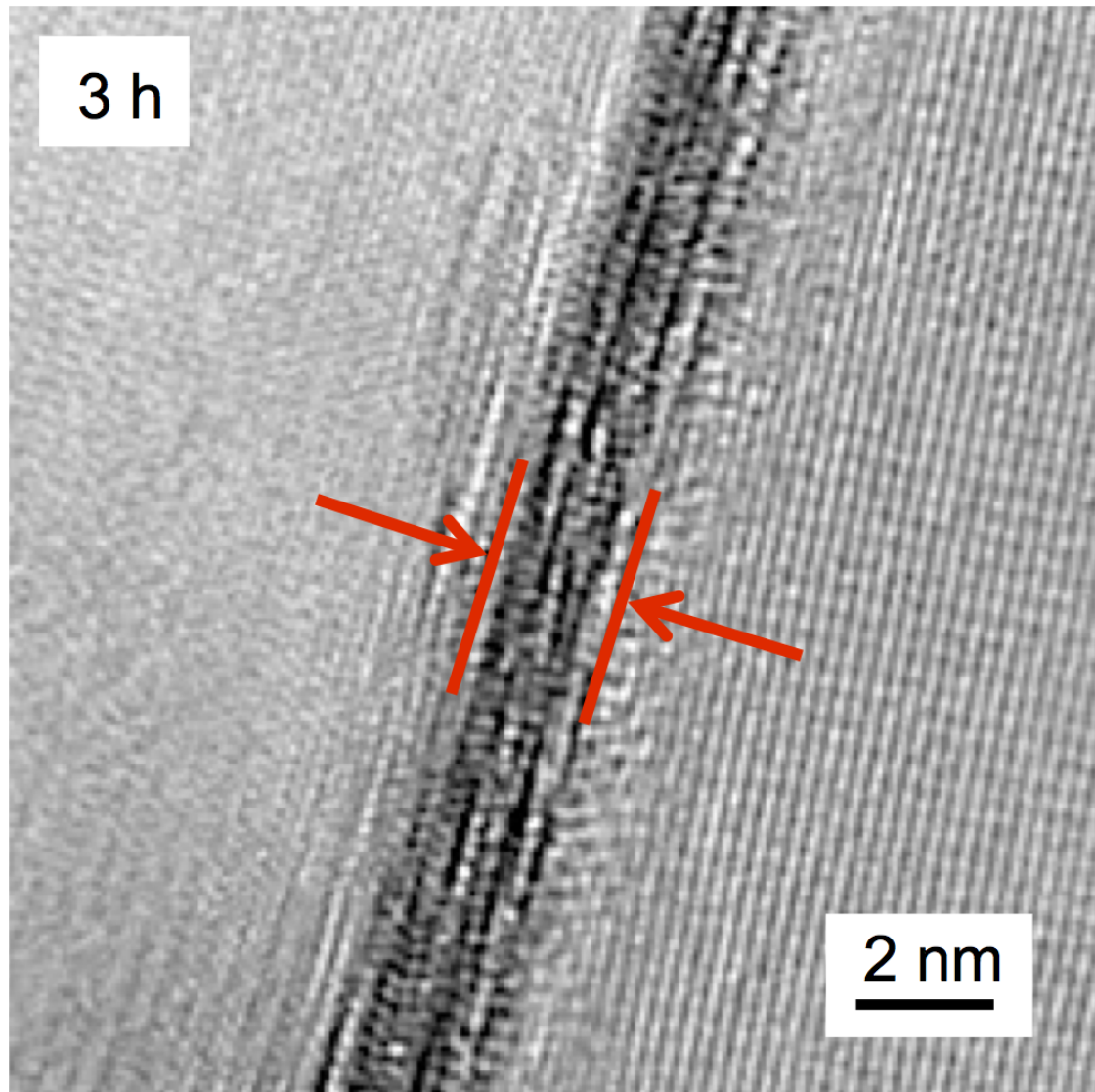


Figure 3.6. Grain boundary of a sample containing 529 ppm Na₂O, 603 ppm SiO₂, and 2 ppm MgO after 3 h at 1525°C.

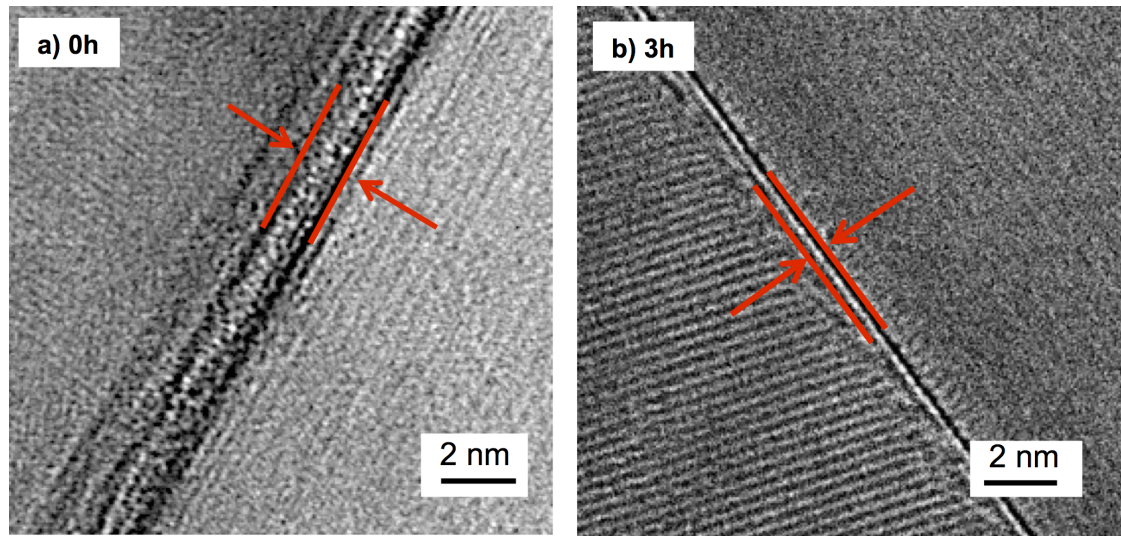


Figure 3.7. Grain boundaries of samples containing 560 ppm Na₂O, 582 ppm SiO₂, and 380 ppm MgO after a) 0 h and b) 3 h at 1525°C.

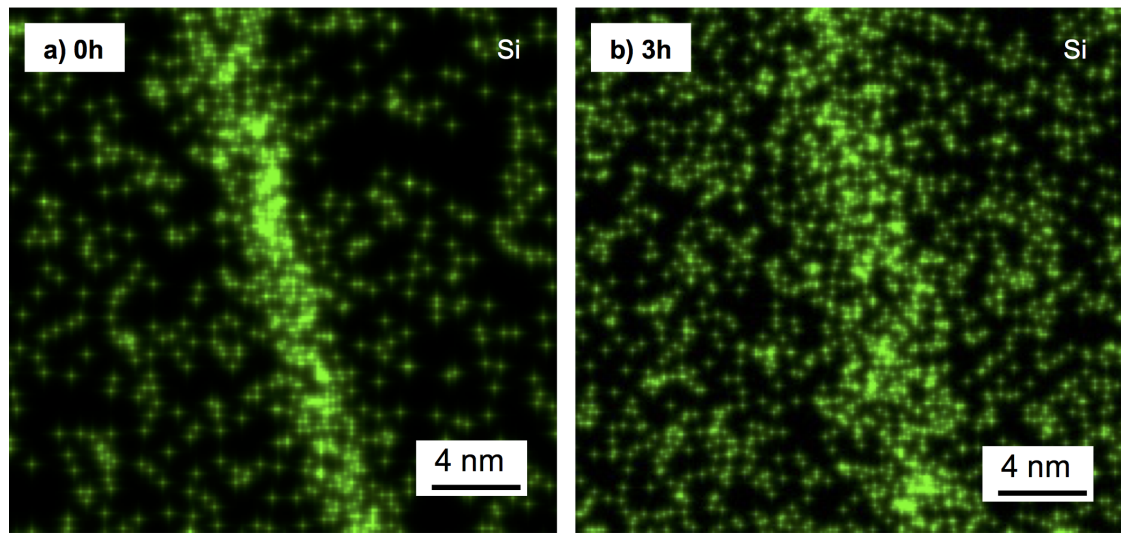


Figure 3.8. EDS of grain boundaries of samples containing 560 ppm Na₂O, 582 ppm SiO₂, and 380 ppm MgO after a) 0 h and b) 3 h at 1525°C showing the Si distribution. After 0 h Si shows a stronger segregation to the grain boundaries than after 3 h.

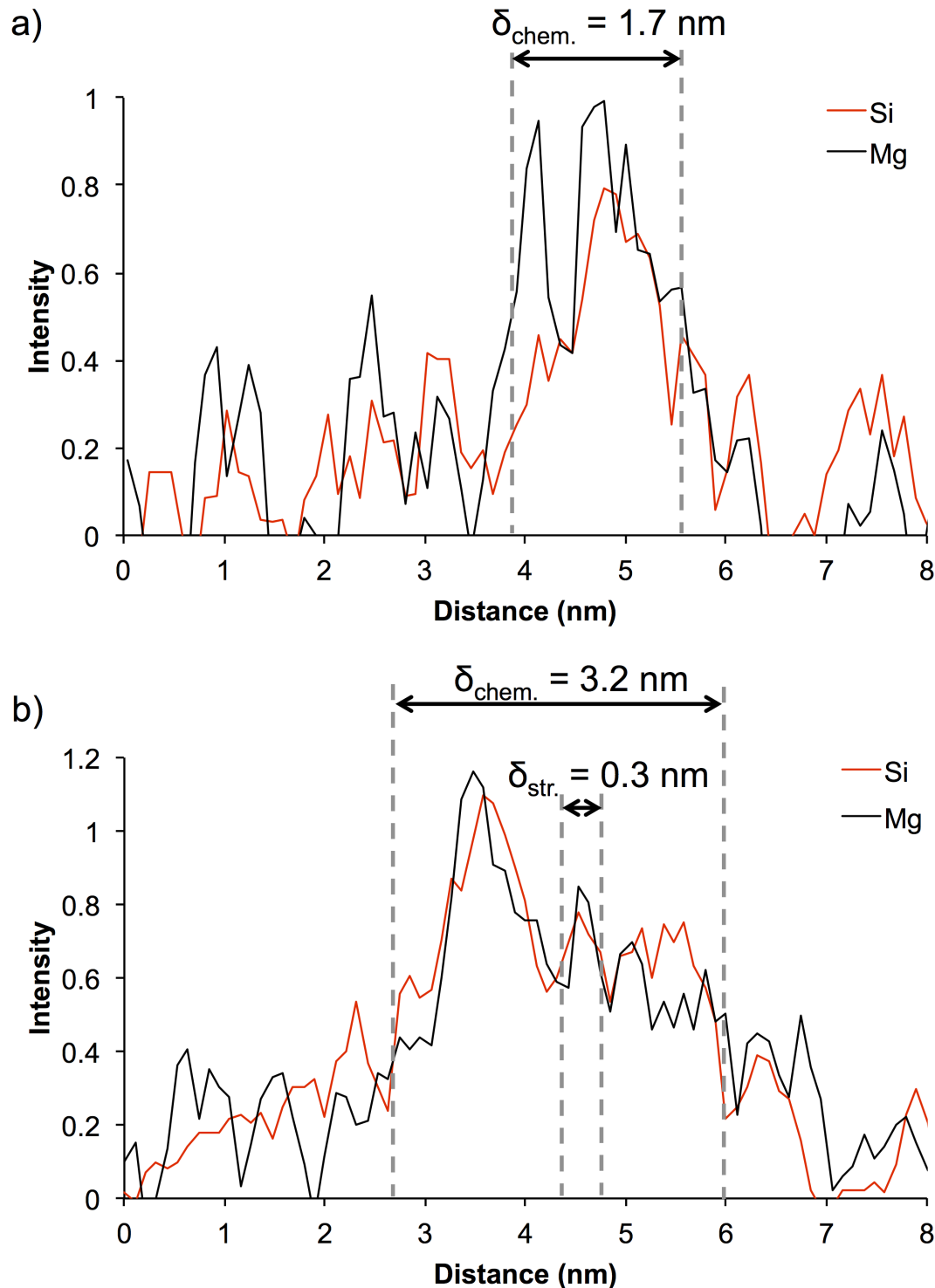


Figure 3.9. EDS line scan across a grain boundary of a sample containing 560 ppm Na₂O, 582 ppm SiO₂, and 380 ppm MgO after sintering at 1525°C for a) 0 h and b) 3 h.

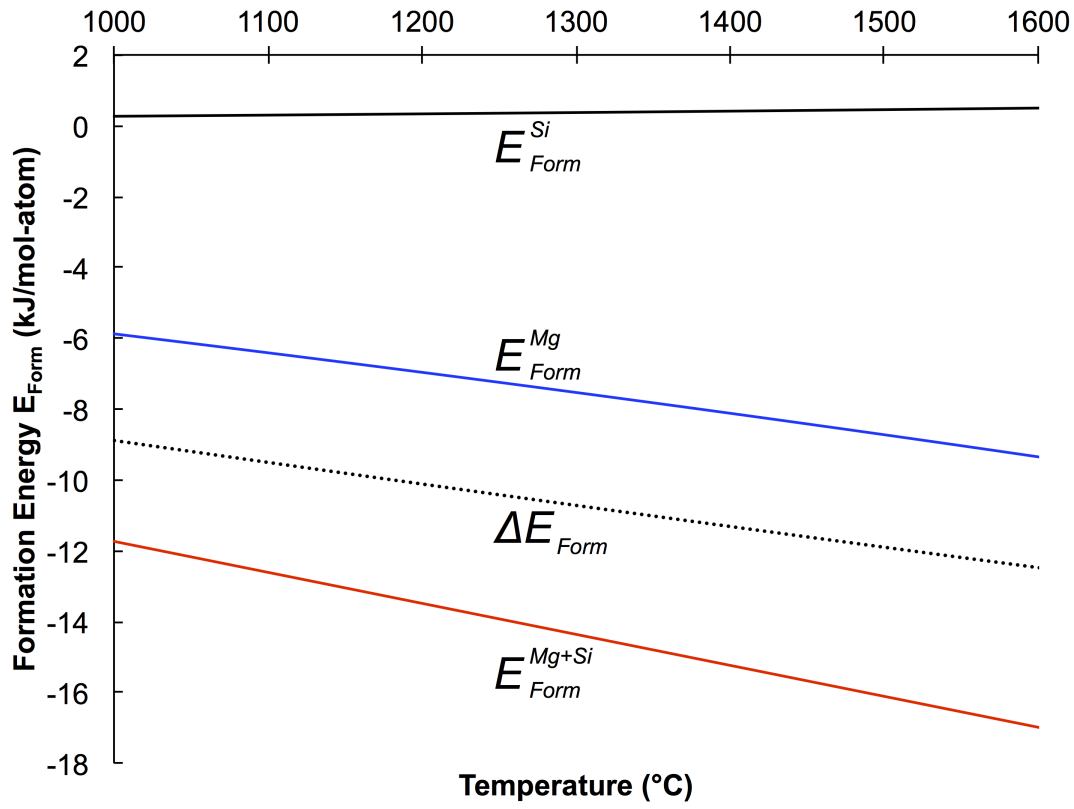


Figure 3.10. Comparison of the formation energy of alpha-Al₂O₃ with an Mg-cluster (E_{Form}^{Mg}), Si-cluster (E_{Form}^{Si}) and Mg+Si-cluster (E_{Form}^{Mg+Si}) as a function of temperature. The formation energy difference (ΔE_{Form}) between the structures was calculated from Eq. REF to compare the formation energy values and show that it is energetically favorable to form Mg+Si-clusters over Si-clusters and Mg-clusters.

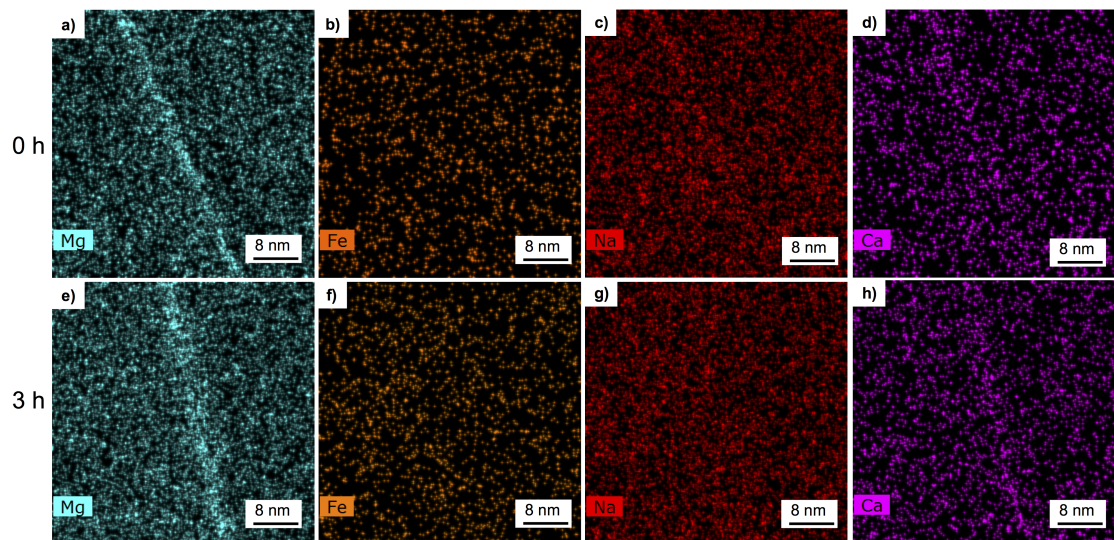


Figure 3.11. EDS maps of different oxides in 380 ppm MgO-doped specialty alumina samples after sintering at 1525°C for a-d) 0 h and e-h) 3 h.

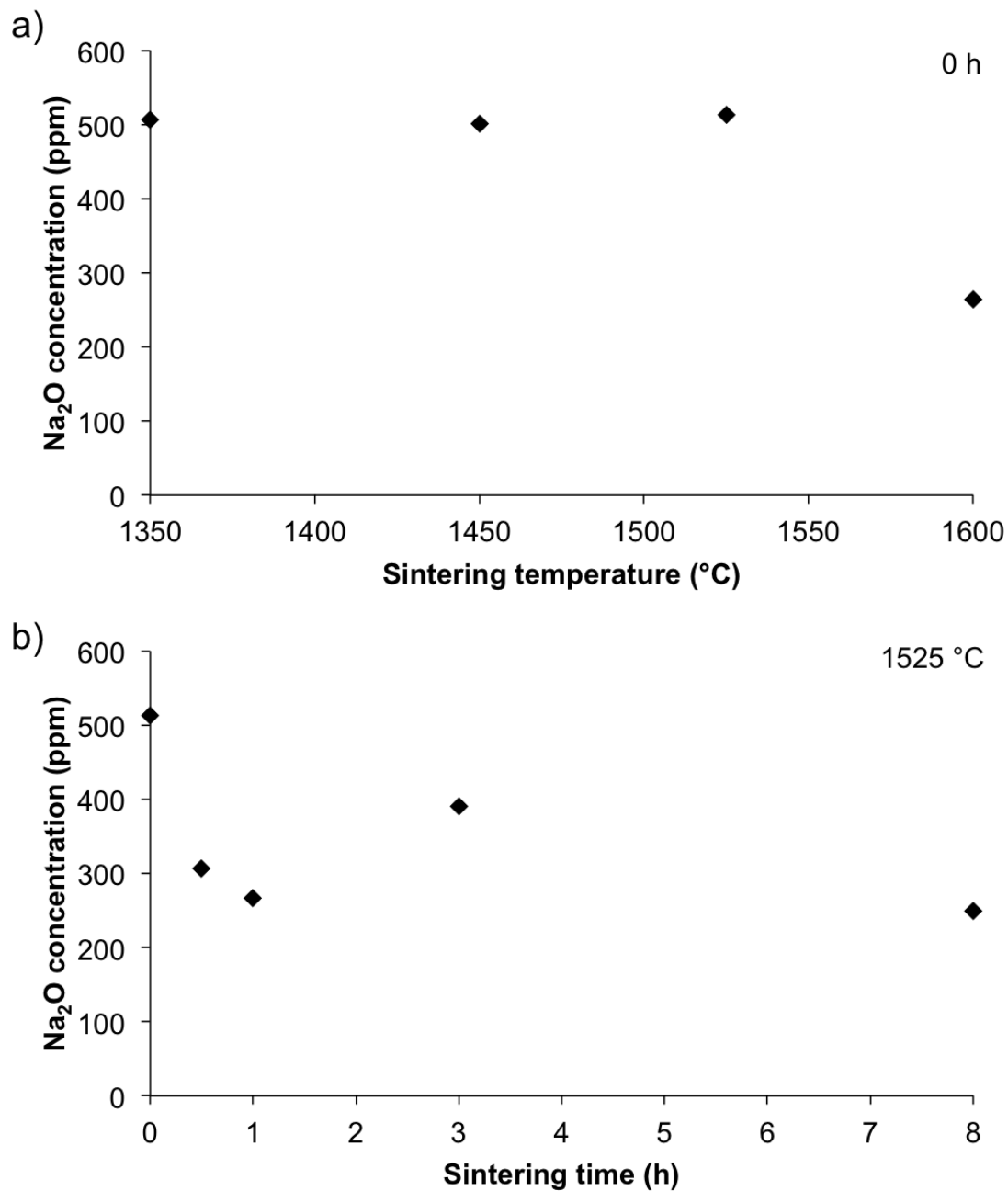


Figure 3.12. Na_2O concentration (ICP measurements) of 380 ppm MgO-doped specialty alumina samples with 560 ppm Na_2O as a) function of sintering temperature and b) as a function of sintering time at 1525°C .

Chapter 4

Dynamic development of nanometer scale grain boundaries during liquid phase sintering

4.1 Introduction

During sintering of ceramics insoluble impurities and dopants can accumulate in the grain boundaries and form an amorphous grain boundary film that significantly influences the sintering behavior and properties of ceramics. Recently, it has been established that grain boundaries in fully dense microstructures can possess different characteristics, depending on chemistry and temperature. Based on their structure and thickness, grain boundaries have been classified into different types of thermodynamically stable complexions [67]. The type of complexion strongly affects transport kinetics and determines the mobility of a grain boundary, and if multiple complexions coexist at a time, multi-modal grain-size distributions and anisotropic microstructures can develop. One class of grain boundaries that is well investigated in dense ceramics are intergranular films (IGF), since they are often observed in a variety of systems such as Si_3N_4 , SiC , and Al_2O_3 [60,68]. IGFs are amorphous grain boundary films with an equilibrium thickness of typically 1-2 nm. Clarke et al. showed that the equilibrium film thickness results from a balance of attractive and repulsive interparticle forces, similar to those seen in colloidal systems [68,69].

In classical sintering theories the differences in grain boundary structures are

considered by distinguishing between solid state and liquid phase sintering with fundamental differences in their respective sintering mechanisms. Solid state sintering occurs by solid state diffusion throughout the entire sintering process. During initial stage sintering surface diffusion leads to the formation of necks between particles. Most of the densification up to $\sim 92\%$ occurs during intermediate stage, where grain boundaries between particles and pore channels along the grain edges form. At densities $>92\%$ the pore channels close and isolated pores first form and are then eliminated during final stage sintering. The dominant diffusion mechanisms during intermediate and final stage sintering are volume and grain boundary diffusion, which can be affected by solute segregated to the grain boundaries [67].

In contrast, for liquid phase sintering [70] the particle compact is penetrated by a liquid film and during the initial sintering stage the powder compact begins to densify by particle rearrangement after the liquid phase has formed. Further densification during intermediate and final stage sintering is controlled by a solution-precipitation mechanism, where the particles of the sinter are dispersed in a liquid glass matrix, and material from the grain boundary area dissolves into the liquid grain boundary phase and diffuses to the particle necks, where it precipitates, leading to a particle contact flattening and densification.

Additional models were developed in the literature that account for the liquid phase redistribution during densification. For example, a number of models describe the filling of pores during liquid phase sintering due to capillarity [71, 72]. However, the existing models in the literature that address liquid phase redistribution typically deal with liquid concentrations of at least a few volume percent. In this case it can be assumed that the concentration of liquid phase is high enough to form a continuous liquid film of equilibrium thickness [60, 68, 69] in the grain boundaries and that excess liquid phase accumulates in necks, pores and glass pockets. For example, Svoboda et al. [73] assumed a constant equilibrium intergranular film thickness of 1.5 nm when they developed their liquid phase sintering model, and Kwon and Messing [34] estimated a grain boundary thickness of ~ 1 nm based on a squeeze film analysis.

The redistribution of liquid phase becomes more complicated as the liquid phase concentration in a sinter is reduced, for example to concentrations <0.2 vol.%. In this case the glass phase concentration could be insufficient to form a liquid

film of equilibrium thickness, and if the glass phase concentration is low enough the grain boundaries may be considered rather solid than liquid, which changes the sintering model that can be applied. This case is interesting specifically in commercial powders used in industry, since they typically contain higher impurity levels than the ultra-high purity powders studied in academia. For example, most fundamental research on alumina uses ultra-high purity aluminas of >99.99% Al₂O₃ and, therefore, sintering is analyzed using solid state sintering models. In contrast commercial alumina powders are typically produced by the Bayer process and are ~99.8% pure with ppm levels of Na₂O, SiO₂, CaO, and Fe₂O₃, and added MgO as a sintering additive. The concentration and ratios of these impurities and additives can vary substantially by the commercial grade and can form a small amount of liquid phase. Despite considerable interest no research has been done on determining what volume fraction of liquid phase is necessary to consider grain boundaries liquid and when to apply a liquid phase sintering model in such a system.

Concentration, chemistry, and distribution of a liquid phase change during densification as a result of increasing temperature during heating and as a result of changing grain boundary area during densification and grain growth. This implies that grain boundaries undergo a dynamic change in physical and chemical character during densification. This dynamic change in chemistry and structure and possible transitions of grain boundaries from solid to liquid or vice versa can significantly impact densification as densification typically occurs via grain boundary diffusion. While most liquid phase sintering models imply that grain boundaries may change during densification, no work has been done on identifying these changes.

In this work we develop a model to predict the dynamic development of grain boundaries from initial to final stage sintering as a function of chemical and physical parameters of a sintering powder. The predicted grain boundary thicknesses are compared with grain boundaries examined by high-resolution TEM.

4.2 Experiment

Two chemically purified Bayer process alumina powders (Almatis, Inc., Leetsdale, PA, USA) were chosen for study. Powder characteristics and experimental details are described in previous chapter [44]. The main difference between the two

powders are the MgO concentrations of 2 ppm (MgO-free powder) and 380 ppm (MgO-doped powder), respectively. The powders were doped with up to 1000 ppm Na₂O and 1000 ppm SiO₂ using sodium acetate (NaC₂H₃O₂*3H₂O, ACS grade, BDH, VWR International LLC, West Chester, PA, USA) and tetraethyl orthosilicate (Si(OC₂H₅)₄, 98%, Aldrich Chemical Company, Inc. Milwaukee, WI, USA), respectively, to obtain chemistries similar to commercial high purity Bayer aluminas at different glass concentrations. Samples with green densities of 59.0 ± 0.5% were fabricated for sintering studies by uniaxial and cold isostatic dry pressing (CIP, Autoclave engineers, Erie, Pa, USA) at 170 MPa and 200 MPa, respectively. The dry pressed cylinders were heated at 10°C/min to 1525°C in a thermomechanical analyzer (TMA, Linseis PT1600, Robbinsville, NJ, USA) to record the shrinkage during heating. Samples were heated at 10°C/min to 1200°C and then at 5°C/min to 1525°C for different hold times. Microstructure and density were measured by the linear intercept (ASTM Standard E112-96) [21] and Archimedes methods (ASTM standard B962-15), [20] respectively. The structure and chemistry of grain boundaries were investigated by transmission electron microscopy (TEM) and energy dispersive x-ray spectroscopy (EDS) using a dual aberration corrected FEI Titan [69] field emission microscope operated at 300 kV and FEI Talos (FEI, Hillsboro, OR, USA) field emission microscope at 200 kV. The EDS on both microscopes is an FEI Super-X system consisting of four SDDs (Silicon Drift Detectors) with a solid angle of 0.9 sr ad. The samples for TEM and EDS were air-quenched from the sintering temperature and prepared using a focused ion beam (Quanta 200 3D Dual Beam FIB, FEI, Hillsboro, OR, USA). Grain boundaries were chosen for analysis that were oriented parallel to the TEM beam in order to accurately measure grain boundary thicknesses in the 2D projection images and EDS profiles.

4.3 Grain boundary thickness in MgO-free alumina

The development of the grain boundary thickness during densification is described for MgO-free powder samples with 529/103 ppm Na₂O/SiO₂, 529/203 ppm Na₂O/SiO₂, and 529/603 ppm Na₂O/SiO₂. As shown in the previous chapter, the main difference of the samples is the concentration of glass phase that forms. The liquidus projection of the Al₂O₃-Na₂O-SiO₂ phase diagram [73] was used to

predict the equilibrium composition of the glass phase during heating as a function of temperature [44], and based on the concentration of Na₂O and SiO₂ the glass phase concentration $\phi(T)$ was estimated as a function of temperature, as shown in Figure 4.1.

The liquid glass is expected to accumulate in particle contacts due to capillary forces [72], and during densification it is assumed that the liquid phase accumulates in the grain boundaries until an equilibrium film thickness [60] is reached. After this equilibrium thickness is reached it is assumed that the excess liquid phase accumulates in the particle necks. The fraction of a particle/grain surface that is in contact with another particle/grain, i.e. the fraction of grain boundary area, increases with increasing density [74]:

$$\alpha(\rho) = 1 - r(\rho) \left(1 - \frac{\rho}{100}\right)^{\frac{1}{2}} \quad (4.1)$$

where r is a factor between 1.4 and 1.7, depending on the relative density. With these assumptions the grain boundary thickness based on the amount of impurities in the samples can be estimated by:

$$\delta = 2 \frac{V_g \phi(T)}{S_g (1 - \phi(T)) \alpha(\rho)} \quad (4.2)$$

where V_g and S_g are the average volume and average surface area of a particle/grain. The parameters of this equation are specific to the system investigated and change during sintering.

If the calculated grain boundary thickness is smaller than a monolayer, e.g. the size of a SiO₄⁴⁻ tetrahedron (~ 0.3 nm), the liquid phase concentration in the sample is not high enough to form a liquid grain boundary phase, assuming a homogeneous distribution of the liquid phase in the sample. We assume that a grain boundary thickness > 0.6 nm, i.e. a bilayer of SiO₄⁴⁻ tetrahedra, is necessary to consider the grain boundary liquid or liquid like. For calculated grain boundary thicknesses > 0.6 nm the grain boundary thickness is assumed to be limited by an equilibrium film thickness, if the concentration of the liquid phase is high enough to form an amorphous film of equilibrium thickness. If the concentration of the liquid phase is not high enough to form an amorphous film of equilibrium thickness, the grain boundary thickness is limited by the concentration of glass phase in the sample.

Dilatometry was used to determine the development of relative density as a

function of temperature (Figure 4.2), assuming isotropic shrinkage of the samples. Now the increase in liquid phase concentration can be expressed as a function of relative density, as seen in Figure 4.3. V_g and S_g were estimated using the average particle/grain size determined from micrographs, assuming spherical particles of the same size, and using the sintering trajectories shown in Figure 4.4, V_g and S_g can be expressed as a function of relative density. The grain boundary thickness can be calculated as a function of relative density since all parameters in Eq. 4.2 can be expressed as a function of the relative density.

4.4 The equilibrium film thickness model

In 1987 Clarke proposed a model to calculate the equilibrium grain boundary thickness based on the equilibrium between attractive van der Waals and capillary pressures (P_{vdW} and P_C) and repulsive electric double layer and structural disjoining pressures (P_{ELD} and P_{ST}) [68, 69]:

$$P_{vdW} + P_C = P_{ELD} + P_{ST} \quad (4.3)$$

The van der Waals pressure is given by

$$P_{vdW} = \frac{H}{6\pi h^3} \quad (4.4)$$

where h is the grain boundary thickness and H is the Hamaker constant, which can be estimated by:

$$H = \frac{3}{4}kT \left(\frac{\varepsilon_\alpha - \varepsilon_\beta}{\varepsilon_\alpha + \varepsilon_\beta} \right)^2 + \frac{3\pi\hbar v}{8\sqrt{2}} \frac{(n_\alpha^2 - n_\beta^2)^2}{(n_\alpha^2 + n_\beta^2)^{\frac{3}{2}}} \quad (4.5)$$

where k is the Boltzmann constant, T is the absolute temperature, ε_α and ε_β are the dielectric constants of the ceramic and the glass phase, respectively, and n_α and n_β are the refractive indices of the ceramic and the glass phase, respectively.

In Clarke's original work the capillary pressure was assumed to be constant, which is a valid assumption for samples at constant densities. However, during densification the capillary pressure changes and can be estimated by [34]:

$$P_C = \frac{\left(0.59 - 0.79(1-\rho)^{\frac{1}{2}}\right)\rho^{\frac{1}{3}}}{0.39(1-\rho)^{\frac{1}{2}}\left(0.59 - 0.39(1-\rho)^{\frac{1}{2}}\right)} \frac{\gamma_{lv}}{r_s} \quad (4.6)$$

where γ_{lv} is the surface tension of the liquid, r_s is the particle radius, and ρ is the relative sintered density.

The structural disjoining force is given by [69]:

$$P_{ST} = -\alpha\tau_0^2 \left(\sinh^2\left(\frac{h}{2X}\right)\right)^{-1} \quad (4.7)$$

where a is a constant that can be approximated by the heat of fusion, τ_0 is a coefficient for the degree of ordering between 0 and 1, and X is a structural correlation length. The electric double layer force is given by [68]

$$P_{ELD} = \frac{16kT}{z^2\pi b_L h^2} \left(\tanh\frac{ze\psi_s}{4kT}\right)^2 (\kappa h)^2 e^{(-\kappa h)} \quad (4.8)$$

where z is the ion charge and e is the proton charge. The Bjerrum length b_L and the inverse of the Debye length κ are given by [68]

$$b_L = \frac{e^2}{4\pi\epsilon_\beta\epsilon_0 kT} \quad (4.9)$$

and [75]

$$\kappa = \sqrt{\frac{2N_A I e^2}{\epsilon_\beta\epsilon_0 kT}} \quad (4.10)$$

where N_A and I are the Avogadro's number and the ionic strength of the liquid, respectively.

4.5 Calculation of the theoretical Equilibrium Film Thicknesses

To calculate the equilibrium film thickness for alumina samples, the contributions P_{vdW} , P_C , P_{ELD} , and P_{ST} were calculated using parameters from the literature. The van der Waals pressure was estimated using Eq. 4.3 and 4.4 for a liquid sodium aluminosilicate glass film ($\epsilon_\beta = 10$ [76], $n_\beta = 1.51$ [36]) located between

two flat alumina surfaces ($\varepsilon_\alpha = 11.6$, $n_\alpha = 1.752$) [69]. The capillary pressure was calculated as a function of the relative density and grain size from the sintering trajectories shown in Figure 4.2, using Eq. 4.6, assuming a surface tension of the sodium aluminosilicate glass of $\gamma_{glass} = 387 \text{ N/m}$ [77]. The structural disjoining pressure was calculated using the heat of fusion of carnegieite (35.8 J/cm^3) for the constant a , and a structural correlation length of 0.3 nm (approximate size of a SiO_4^{4-} tetrahedron). The heat of fusion of carnegieite was chosen since its chemical composition is close to the chemical composition of the grain boundary phase investigated here. It is reported in the literature that considerable ordering of intergranular films can extend up to 1.5 nm into the intergranular film before they can be assumed completely amorphous [78]. Therefore, a high ordering factor of 0.75 was assumed.

The electric double layer pressure was calculated as a function of film thickness h using Eq. 4.8-4.10, with $z = 1$ (Na^+ ion charge) and $\varepsilon_\beta = 10$. The electrostatic potential ψ_s and ionic strength I are difficult to estimate, since they are not reported in the literature for the present system. Literature reports estimating equilibrium film thicknesses based on Clarke's model assume values for ψ_s within a reasonable range of up to 1.5 V [68, 79]. In this work we attempt to estimate ψ_s and I based on the composition and structure of sodium aluminosilicate glass. It is reported in the literature [80] that all Al^{3+} ions in sodium aluminosilicate glasses are in tetrahedral coordination if $\text{Na}/\text{Al} \geq 1$, and the local charge deficit of an AlO_4^{5-} tetrahedron (compared to the SiO_4^{4-} tetrahedron) is compensated by an associated Na^+ . Excess Na^+ ions that are not required for this charge compensation act as network modifiers in the glass. For $\text{Na}/\text{Al} < 1$, there are not enough Na^+ ions to stabilize all Al^{3+} ions in tetrahedral coordination, and excess Al^{3+} ions can form triclusters or are in octahedral coordination [80].

In this model we assume for $\text{Na}/\text{Al} > 1$ in the glass that Na^+ ions compensating the charge of an AlO_4^{5-} tetrahedron are not mobile due to electrostatic attraction between the charged AlO_4^{5+} tetrahedron and the Na^+ ion, whereas excess Na^+ ions are assumed to be available as charge carriers. For the samples investigated here an I of 2.25 mol/l was calculated. If we assume that a fraction f_{cc} of the charge carriers segregate to the immediate particle/grain surface, a charge carrier density σ can be calculated by

$$\sigma = \frac{(c_{Na} - c_{Al}) f_{cc} V_{glass} N_A}{V_m \pi d^2} \quad (4.11)$$

where c_{Na} and c_{Al} are the concentration of Na^+ and Al^{3+} ions in the glass, respectively, V_{glass} is the volume of glass around one particle/grain, V_m is the molar volume of the glass, and d is the particle/grain diameter. The electrostatic potential can then be calculated by [68]:

$$\psi_s = \sinh^{-1} \left(\frac{\sigma 2\pi z e b_L}{\kappa} \right) \frac{2kT}{ze} \quad (4.12)$$

The composition of the glass phase in the samples estimated from the phase diagram changes during heating, and consequently the Na/Al ratio changes as shown in Figure 4.5. ψ_s changes during heating because of the changing charge carrier concentration, the increasing grain boundary area, and the increasing grain size during densification. Figure 4.6 shows the change in ψ_s during heating, assuming a glass density of 2.45 g/cm³ and 75% of the charge carriers segregate to the particle/grain surface ($f_{cc} = 0.75$). The estimated values for ψ_s are reasonable when compared to ψ_s values used in the literature [68].

Figure 4.7 shows the individual contributions to the equilibrium film thickness plotted as a function of film thickness for a sample with 529 ppm Na_2O and 603 ppm SiO_2 at 1525°C and a relative density of 93%. It can be seen that the net pressure, i.e. the sum of the acting pressures, is 0 MPa for a film thickness of 1.7 nm, which corresponds to the equilibrium film thickness. From the above discussion it is apparent that P_{vdW} , P_{CP} , and P_{ELD} change during densification. The film thickness at which the net pressure is 0 MPa (i.e., the equilibrium film thickness) was calculated for samples at different relative densities during the sintering process, and the calculated equilibrium film thicknesses are shown in Figure 4.8. It should be noted that P_{vdW} and P_C are a function of temperature, since the parameters they are calculated from are functions of temperature, glass composition, refractive indices, dielectric constants, and surface tension. However, investigations showed that the changes in P_{vdW} and P_C due to the changing temperature are insignificant, and therefore, these contributions were assumed to be constant. Figure 4.8 shows that the equilibrium film thickness does not depend on the amount of glass phase, but decreases as a function of relative density from 2.2 nm at ~60% relative density to 1.6 nm at 98% relative density, as seen in Figure 4.7.

It is interesting to note that for film thicknesses > 1 nm P_C and P_{ST} control the equilibrium thickness, and the contributions from P_{vdW} and P_{ELD} are negligible. At film thicknesses > 1 nm P_{ST} is not expected to change as a function of density, and, therefore, the equilibrium thickness during densification is governed by the change in P_C . For film thicknesses < 1 nm P_{ELD} , P_{ST} , and P_{vdW} significantly contribute to the force balance and P_C is negligible.

Figure 4.9 shows plots of the development of the grain boundary thickness as a function of relative density for different glass concentrations. The trajectory of the equilibrium film thickness (see also Figure 4.8) represents the grain boundary thickness if enough glass phase is present to form a film with equilibrium thickness. The three trajectories labeled with 529/103 ppm Na₂O/SiO₂, 529/203 ppm Na₂O/SiO₂, and 529/603 ppm Na₂O/SiO₂ are the estimated grain boundary thicknesses based on the amount of glass phase that is present in the samples. For all glass concentrations, the grain boundary thickness first decreases during initial and intermediate stage sintering. This decrease in grain boundary thickness is due to the increase in grain boundary area with increasing relative density, since the liquid glass phase is distributed over a larger grain boundary area. At the end of the intermediate sintering stage and during final stage sintering grain growth begins, which results in a reduction of the grain boundary area and, therefore, an increase in grain boundary thickness.

For samples with 529/103 ppm Na₂O/SiO₂ and 529/203 ppm Na₂O/SiO₂ the grain boundary thicknesses determined from the amount of glass phase are less than the equilibrium film thickness, and therefore, the grain boundary thickness is limited by the amount of glass phase in the sample. For samples with 529/603 ppm Na₂O/SiO₂ the glass phase concentration in the sample is close to the glass phase concentration necessary to form a film of equilibrium thickness, and the grain boundary thickness is limited by the amount of glass phase or the equilibrium film thickness, depending on the relative density. For samples with higher glass concentrations, the grain boundary thickness is determined by the equilibrium film thickness.

4.6 High-resolution TEM

The predicted grain boundary thicknesses were compared to grain boundary thicknesses measured from high-resolution TEM images of samples with different glass concentrations. Figure 4.10 shows high resolution TEM images of the grain boundaries of samples with 0.066 vol.% (529/203 ppm Na₂O/SiO₂), 0.21 vol.% (529/603 ppm Na₂O/SiO₂), and 0.36 vol.% glass phase (1000/1000 ppm Na₂O/SiO₂) after 3 h at 1525°C. The thicknesses of the amorphous grain boundary as measured from the TEM images are 1.0 nm, 1.7 nm and 1.9 nm, respectively.

As seen in Figure 4.9 the measured grain boundary thicknesses agree well with the predicted grain boundary thicknesses. For a sample of 96% relative density and 0.073 vol.% glass phase the predicted grain boundary thickness is 0.9 nm, and the measured grain boundary thickness is 1.0 nm (Figure 4.10a). The equilibrium grain boundary thickness for this sample is 1.6 nm, however, the glass phase concentration is only high enough to form a 1.0 nm thick film. For the sample with 0.21 vol.% (529/603 ppm Na₂O/SiO₂) and a relative density of 93% the measured grain boundary thickness of 1.7 nm agrees well with the estimated equilibrium film thickness of 1.7 nm. The glass phase concentration in this sample is high enough to form a film with a thickness of ~2.2 nm, however, the grain boundary thickness is limited by the equilibrium film thickness. For samples with even higher glass concentrations of 0.36 vol.% the glass phase concentration is high enough to form a grain boundary thickness > 3.5 nm, however, the grain boundary thickness determined by TEM is 1.9 nm, which is close to the value of the equilibrium film thickness of 1.7 nm.

Figure 4.9d shows a sample with 0.03 vol.% glass phase (29/103 ppm Na₂O/SiO₂). There is no amorphous film in the grain boundaries because for samples with low SiO₂ concentrations such as 103 ppm the theoretically predicted grain boundary is less than a monolayer, and the amount of SiO₂ is insufficient to form a continuous amorphous film in the grain boundaries. However, EDS analysis shows that there is still SiO₂ segregated to the grain boundaries. Note that the maximum sintering temperature of the samples in this work is 1525°C. At higher sintering temperatures a higher glass phase concentration is expected, and, therefore, thicker grain boundaries would be observed.

4.7 The effect of changes in powder chemistry

4.7.1 Na₂O/SiO₂ ratio

For the results above a Na₂O/SiO₂ ratio ≥ 0.5 in the sample was assumed, which results in a Na₂O/SiO₂ ratio of 0.5 in the glass phase. For Na₂O/SiO₂ ratios < 0.5 the composition of the glass phase is expected to change, and consequently the grain boundary thickness is expected to change as a function of chemistry.

Figure 4.11 shows a high resolution TEM image of a grain boundary of a sample containing 0.17 vol.% glass phase (29/603 ppm Na₂O/SiO₂) and a molar Na₂O/SiO₂ ratio of 0.1 after 3 h at 1525°C, and the measured grain boundary is ~ 1.0 nm thick. Based on the amount of impurities a grain boundary thickness of 2.2 nm is expected in those samples, which indicates that for this chemical composition an equilibrium grain boundary thickness [60] is reached at ~ 1.0 nm. Investigations on how the capillary pressure and van der Waals pressure change as a result of the changed glass chemistry show that the differences in the resulting pressures are negligible. Therefore, the reduction can be attributed to a reduction in the repulsive P_{ST} and P_{ELD} .

The Na/Al ratio in the glass phase of the sample with 29/603 ppm Na₂O/SiO₂ is < 1 , and all Na⁺ ions are assumed to stabilize Al³⁺ ions in tetrahedral coordination. Therefore, no Na⁺ ions are available as charge carriers, and P_{ELD} is assumed to be zero. If P_{ELD} is assumed to be zero and P_{ST} is the same as for higher Na₂O/SiO₂ ratios, the change in equilibrium film thickness is < 0.1 nm. This confirms the earlier conclusion that P_{ST} is the dominant repulsive pressure at film thicknesses ≥ 1 nm, and that P_{ELD} is insignificant for the equilibrium grain boundary thicknesses investigated here. This means P_{ST} has to decrease as the Na₂O/SiO₂ ratio in the sample decreases. Computer simulations showed that the ordering of sodium silicate glass between two alumina surfaces increases with increasing Na₂O/SiO₂ ratio [81]. Therefore, it is reasonable to assume a lower ordering parameter τ_0 for the sample with a molar Na₂O/SiO₂ ratio of 0.1. For example, if an ordering parameter of 0.25 is assumed the calculated equilibrium film thickness is ~ 1.0 nm for samples with a relative density of 93%, which is close to the observed grain boundary thickness seen in Figure 4.11.

4.7.2 MgO-doped Bayer alumina

The influence of MgO on the sintering of Bayer alumina was reported in previous work, and it was shown that MgO increases the solubility of SiO₂ in the alumina lattice. Therefore, the reduction of SiO₂ on the grain boundaries by this process has to be taken into account when the grain boundary thickness is calculated. Figure 4.12 shows high resolution TEM images of grain boundaries of the MgO-doped powder with a) 60/82 ppm Na₂O/SiO₂, b) 60/582 ppm Na₂O/SiO₂, and c) 560/582 ppm Na₂O/SiO₂ after 3 h at 1525°C and the amorphous film thicknesses are 0 nm, 0.6 nm, and 0.8 nm, respectively. For the sample containing 60 ppm Na₂O and 82 ppm SiO₂ no amorphous film is expected because the amount of liquid phase in this sample is not sufficient to form a monolayer, similar to the MgO-free powder samples with 103 ppm SiO₂ seen in Figure 4.9d.

For the samples with 60/582 ppm Na₂O/SiO₂ and 560/582 ppm Na₂O/SiO₂ the grain boundaries are substantially thinner than the theoretical calculation of ~2.2 nm. As reported in previous work, we believe that this is due to a co-dissolution process of Mg²⁺ and Si⁴⁺ into the alumina lattice, which reduces the amount of liquid phase in the grain boundaries. Assuming that equivalent amounts of SiO₂ and MgO go into solid solution a maximum of 380 ppm MgO and 380 ppm SiO₂ could dissolve into the alumina lattice, which leaves 202 ppm SiO₂ in the grain boundaries that can form a liquid phase. With 202 ppm SiO₂ in the grain boundaries an amorphous film with a thickness of ~0.8 nm is calculated, which agrees well with the observed grain boundary thicknesses of 0.6 and 0.8 nm for the samples containing 560/582 ppm Na₂O/SiO₂ and 60/582 ppm Na₂O/SiO₂, respectively.

4.8 Conclusion

A model that describes the dynamic change in grain boundary chemistry and thickness during densification of Bayer alumina was developed. SiO₂ and Na₂O impurities form a glass phase during heating, which accumulates in particle contacts due to capillarity. The chemistry and concentration of this glass phase changes as a function of temperature. During sintering the grain boundary area changes as a result of densification and grain growth, which affects the glass phase distribution

and, therefore, leads to the observed dynamic change in grain boundary thickness as a function of relative density.

An intergranular film of equilibrium thickness can form between particles/grains if the glass phase concentration is sufficient, and an interparticle force balance governs the grain boundary thickness. We demonstrated that for grain boundary thicknesses ≥ 1.0 nm the contributions that control the equilibrium intergranular film thickness are the attractive capillary pressure and the repulsive structural disjoining pressure. If the glass phase concentration in the sample is insufficient to form an intergranular film of equilibrium thickness the grain boundary thickness is determined by the glass phase concentration in the sample. Changes in powder chemistry such as changing the $\text{Na}_2\text{O}/\text{SiO}_2$ ratio or the MgO concentration affect the concentration of glass phase in the sample and the interparticle force balance, which leads to a change in grain boundary thickness. Grain boundary thicknesses measured from high-resolution TEM images agree well with predicted values.

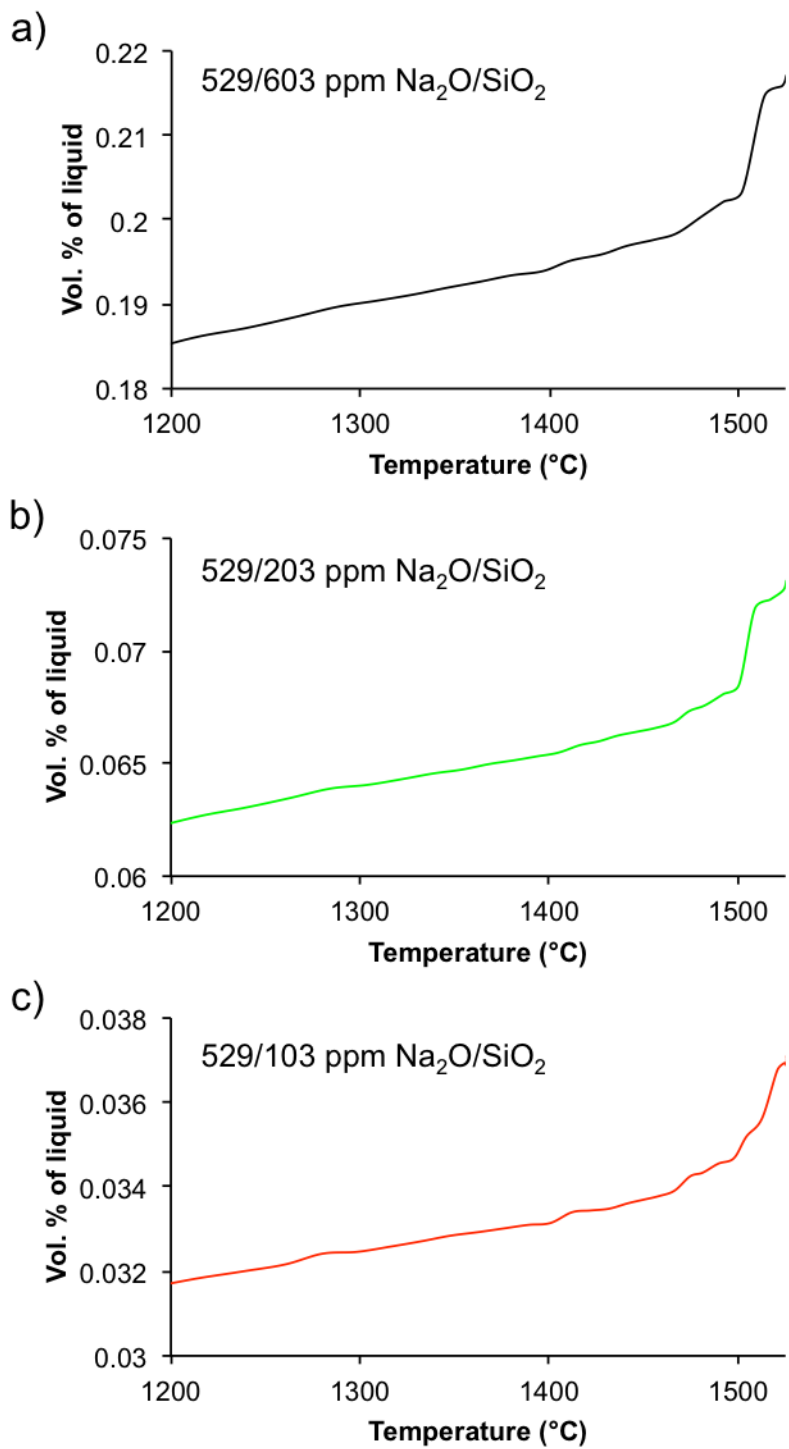


Figure 4.1. Increase in concentration of liquid phase as a function of temperature for MgO-free powder samples with 529 ppm Na_2O and different SiO_2 concentrations.

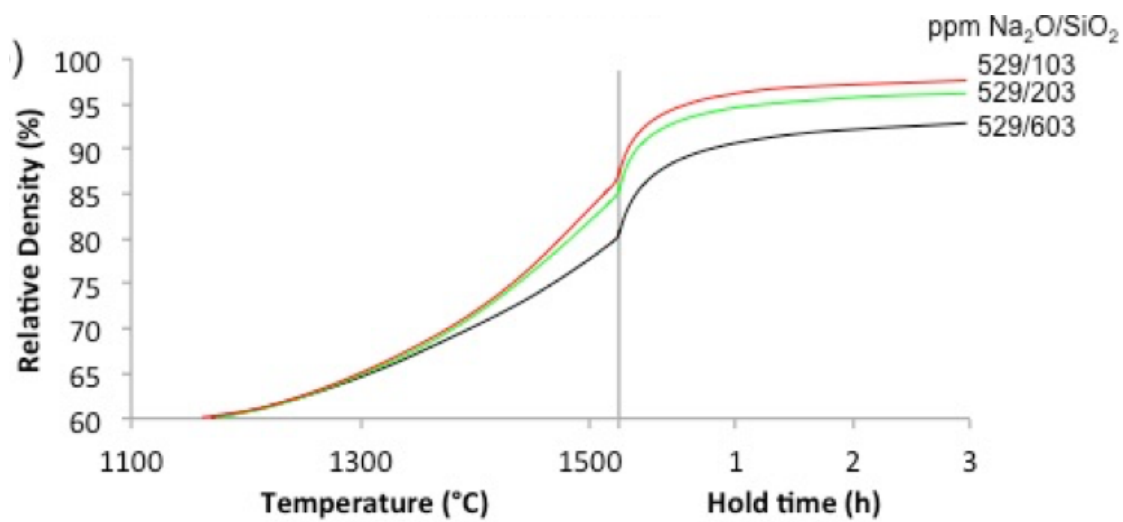


Figure 4.2. Relative density as a function of temperature and hold time determined from dilatometry for MgO-free powder samples with 529 ppm Na₂O and different SiO₂ concentrations.

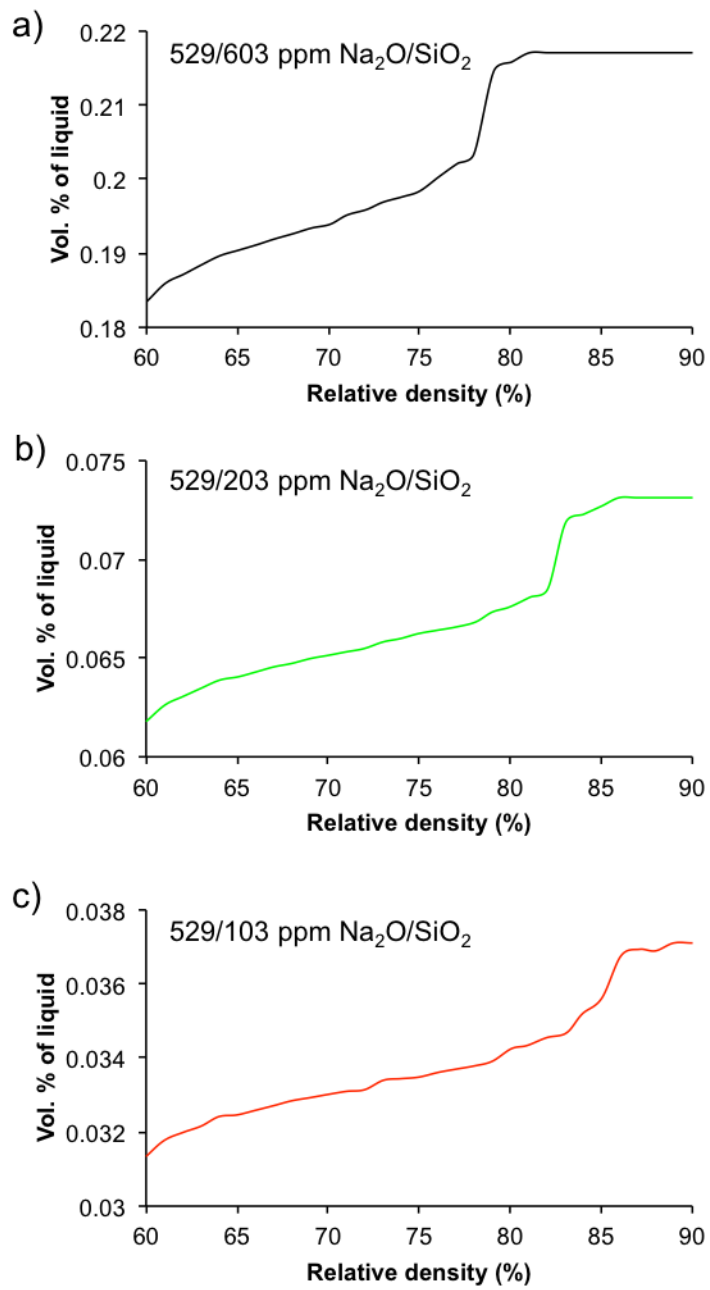


Figure 4.3. Liquid phase concentration as a function of relative density for MgO-free powder samples with 529 ppm Na₂O and different SiO₂ concentrations.

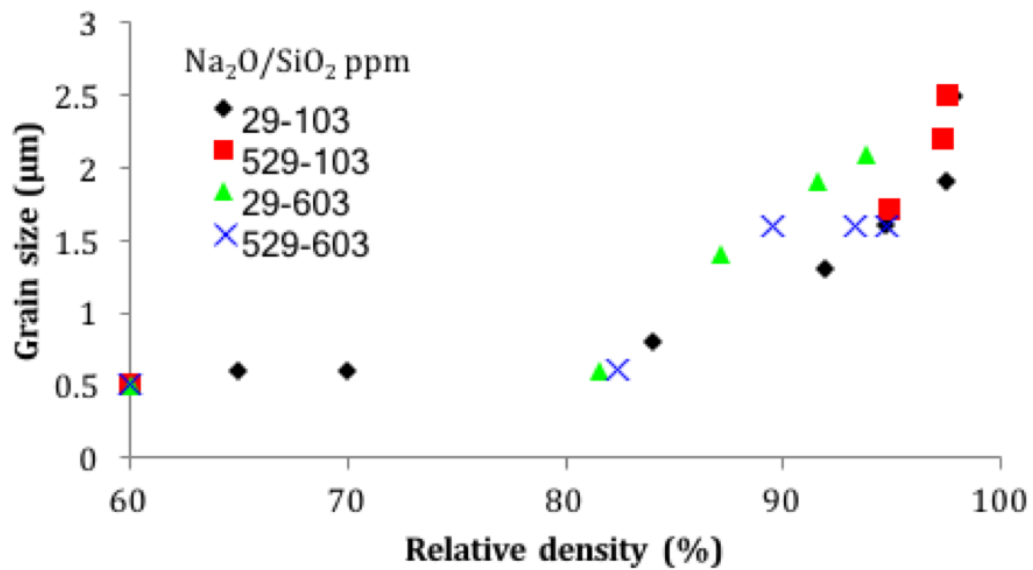


Figure 4.4. Grain size - density trajectories as a function of Na_2O and SiO_2 concentration for MgO-free alumina.

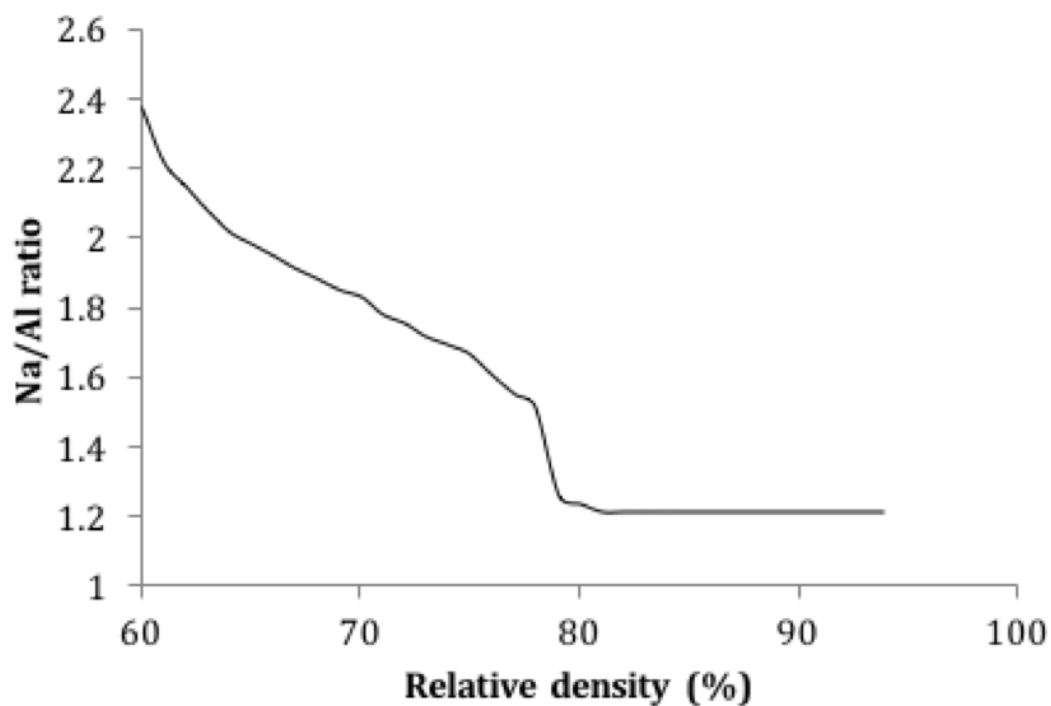


Figure 4.5. Change in Na/Al ion ratio in the liquid phase during sintering of samples with $\text{Na}_2\text{O}/\text{SiO}_2$ ratios > 0.5 .

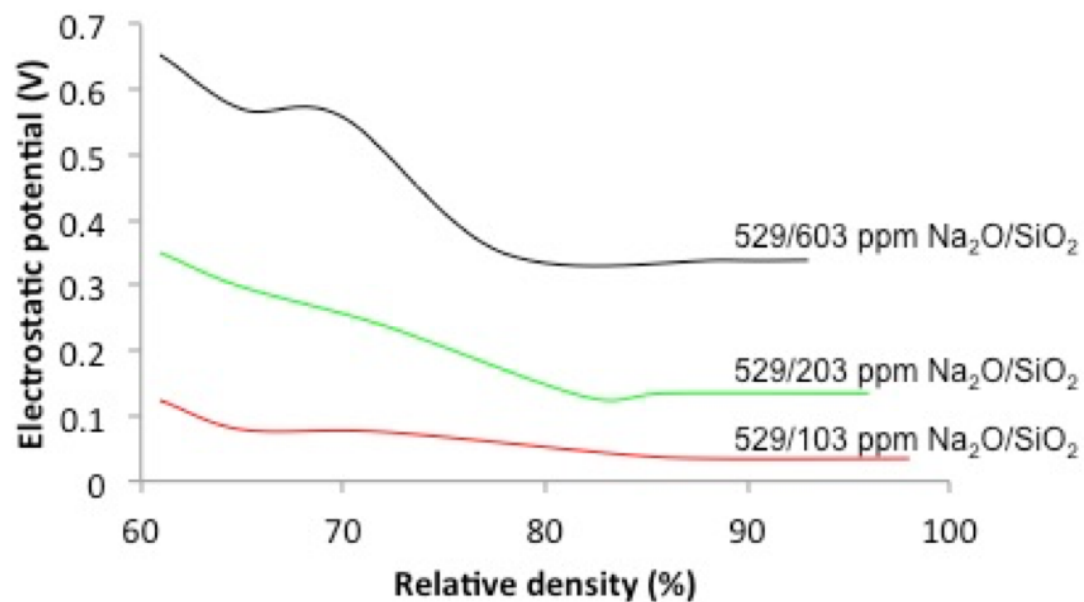


Figure 4.6. Development of the electrostatic potential as a function of relative density. For MgO-free powder samples with 529 ppm Na_2O and different SiO_2 concentrations.

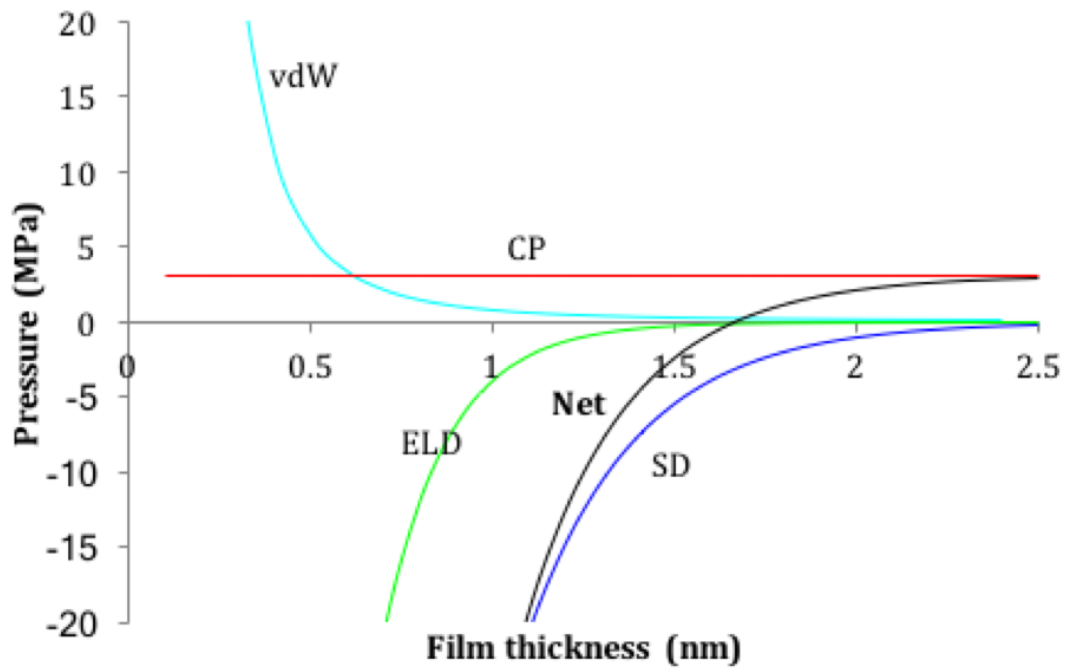


Figure 4.7. Contributions to the equilibrium film thickness as a function of film thickness for MgO-free powder samples with 529/603 ppm Na₂O/SiO₂ at a relative density of 93%.

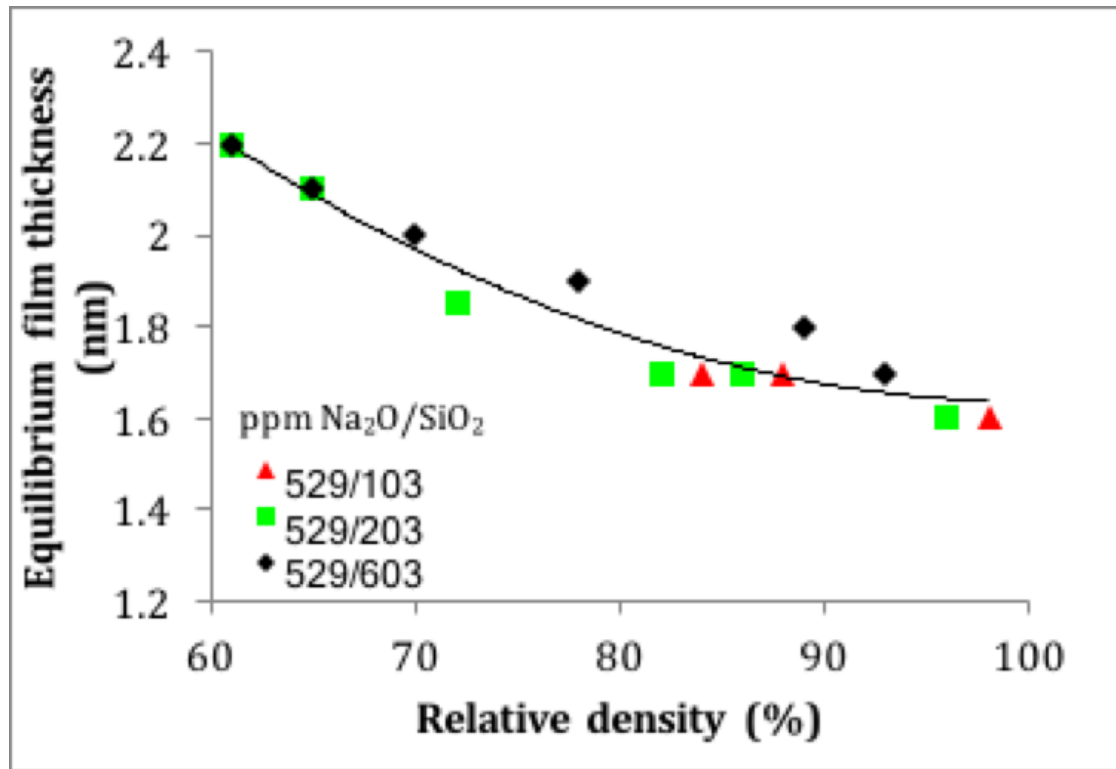


Figure 4.8. Calculated equilibrium film thickness for MgO-free powder samples at different chemistries as a function of relative density.

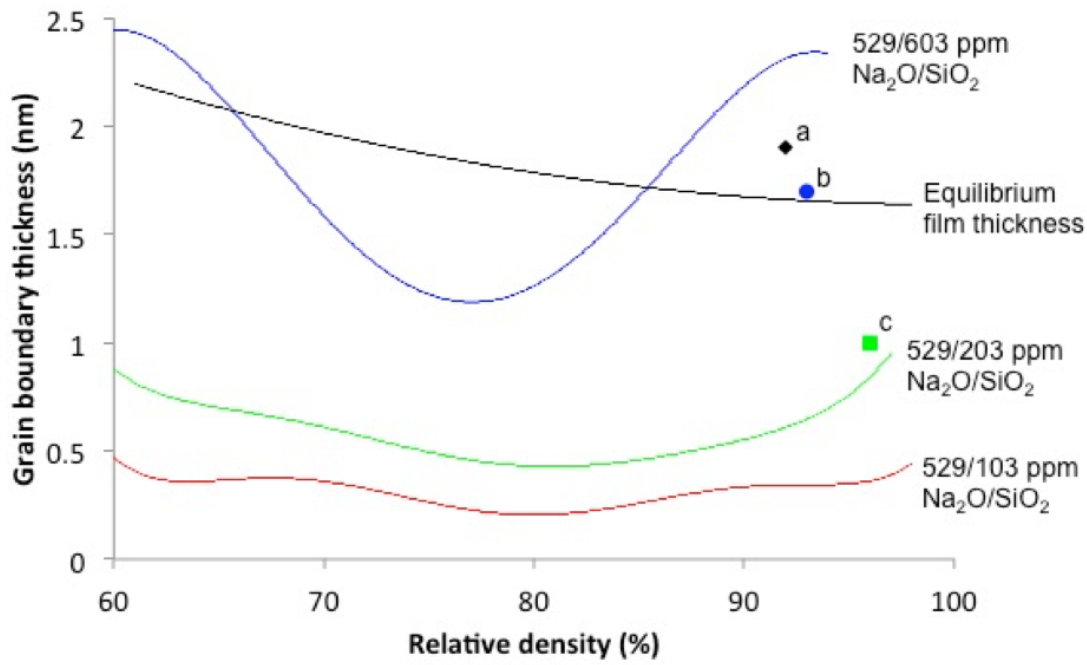


Figure 4.9. Calculated grain boundary thicknesses as a function of relative density for MgO-free powder samples. The trajectories labeled with 529/603 ppm $\text{Na}_2\text{O}/\text{SiO}_2$, 529/203 ppm $\text{Na}_2\text{O}/\text{SiO}_2$, and 529 ppm $\text{Na}_2\text{O}/\text{SiO}_2$ were calculated based on the liquid phase concentration and sintering stage. The equilibrium film thickness was calculated based on Clarke's model. The calculated grain boundary thicknesses are compared to measured grain boundary thicknesses (data points a: 1000/1000 ppm $\text{Na}_2\text{O}/\text{SiO}_2$, b) 529/603 ppm $\text{Na}_2\text{O}/\text{SiO}_2$, c) 529/203 ppm $\text{Na}_2\text{O}/\text{SiO}_2$ after heating at 1525°C for 3 h).

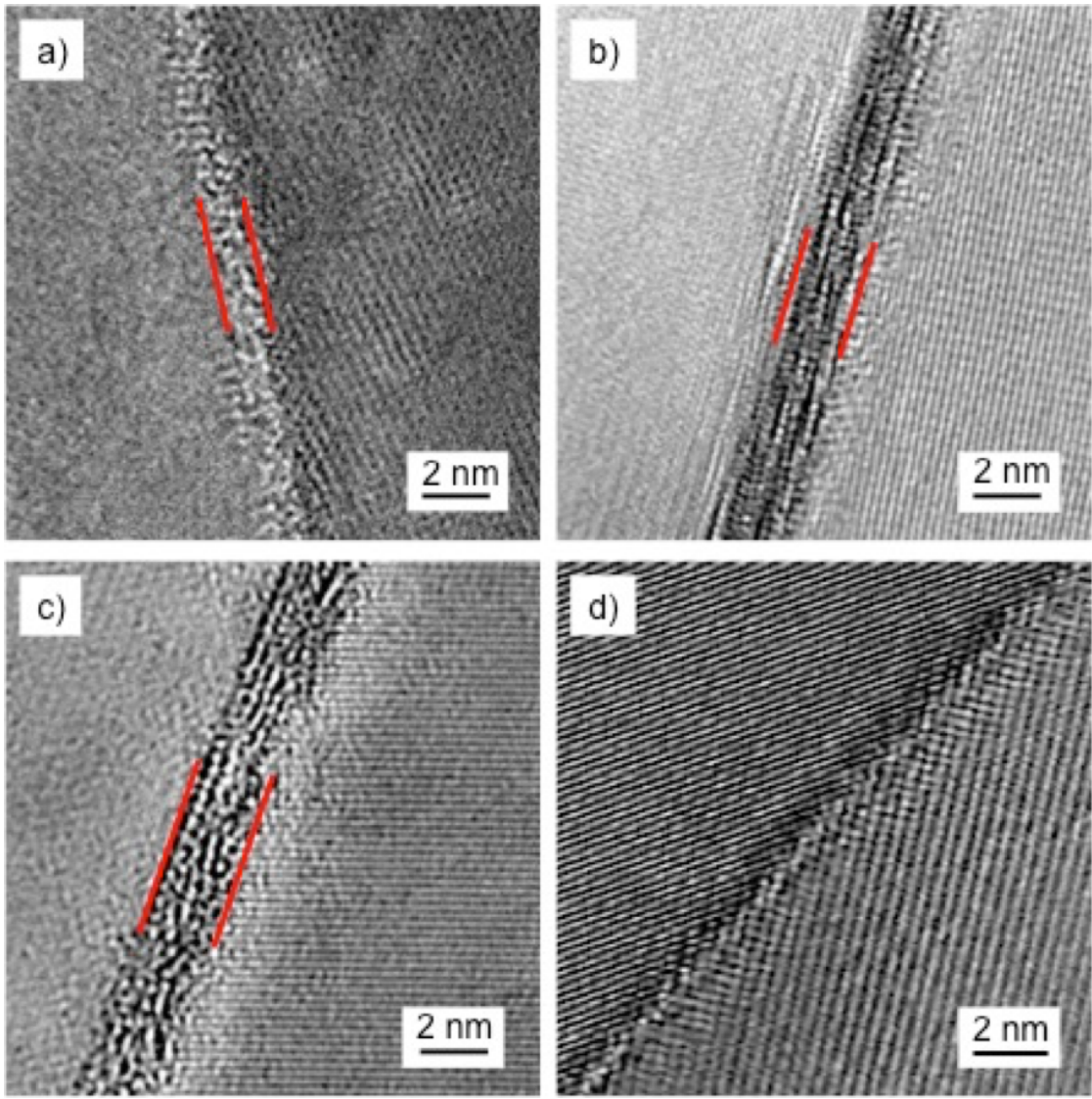


Figure 4.10. TEM images of MgO-free powder samples with a) 529/203 ppm Na₂/SiO₂, b) 529/603 ppm Na₂/SiO₂, c) 1000/1000 ppm Na₂/SiO₂, and d) 29/103 ppm Na₂/SiO₂ after sintering at 1525°C for 3 h.

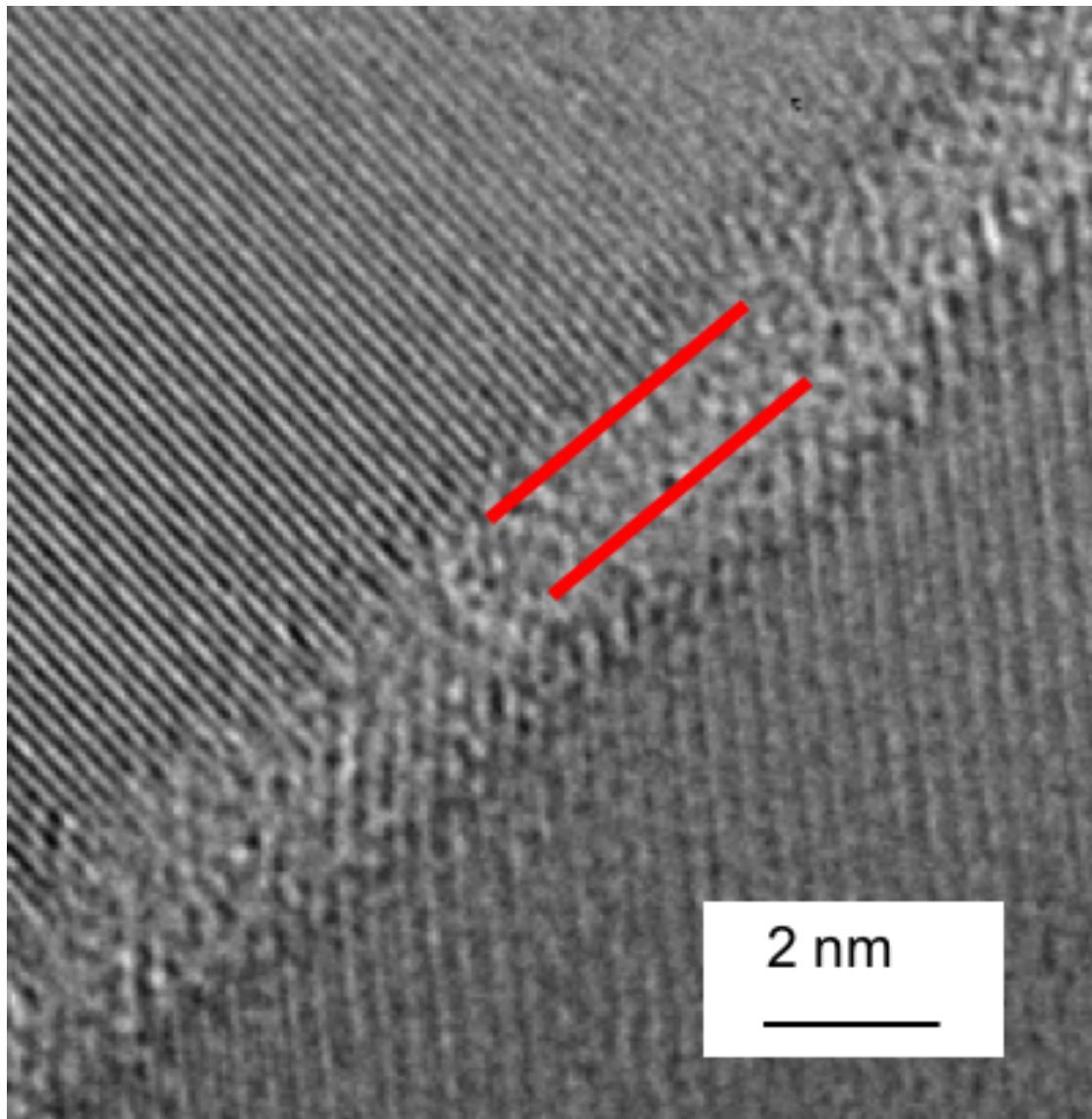


Figure 4.11. TEM image of a MgO-free powder sample with 29/603 ppm Na₂O/SiO₂.

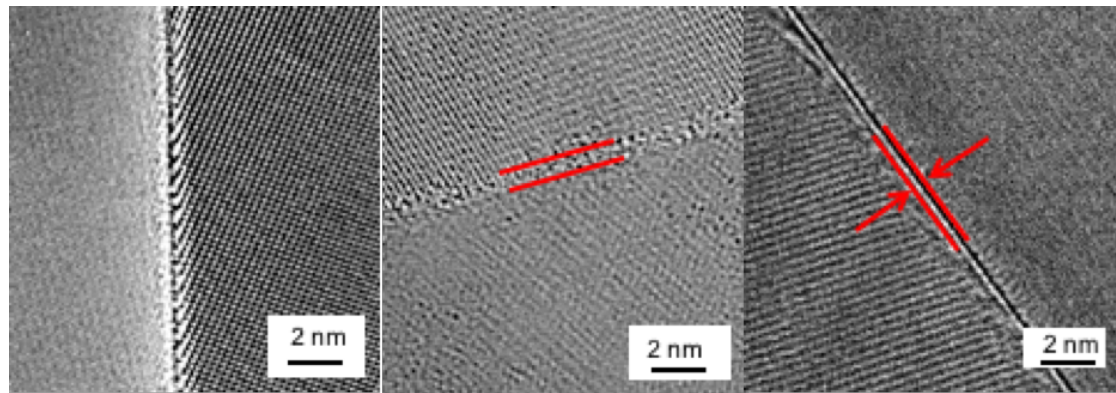


Figure 4.12. TEM images of MgO-doped (380 ppm) powder samples with a) 60/82 ppm Na₂O/SiO₂, b) 60/582 ppm Na₂O/SiO₂, and c) 560/582 ppm Na₂O/SiO₂. After heating at 1525°C for 3 h.

Chapter 5 |

Second phase formation in Bayer alumina

5.1 Introduction

It is reported in the literature that dopants and impurities such as MgO, CaO, and Na₂O can form second phases such as spinel, calcium hexaluminate, and β -Al₂O₃, respectively, if their concentration is high enough. For Bayer aluminas β -Al₂O₃ is of particular interest because Na₂O impurities are characteristic to Bayer alumina and small amounts of a few hundred ppm can be sufficient to form β -Al₂O₃. Rankin and Merwin [25] were the first to observe the formation of a new alumina phase in the high Al₂O₃ region in the system CaO-Al₂O₃-MgO. They believed it was an allotropic modification of Al₂O₃, and named it β -Al₂O₃. However, later work clarified that there is a relation between the alkali content in the Al₂O₃ and the formation of β -Al₂O₃ [82], and that β -Al₂O₃ is an alkali aluminate, rather than an allotropic form of Al₂O₃ [31]. Ridgway et al. [26] reported that the Na₂O content in Bayer process alumina can be high enough for the formation of β -Al₂O₃, and that β -Al₂O₃ forms in "dry ore process" Al₂O₃ (with unspecified low concentrations of Na₂O) only when Na₂O or K₂O is added. Four types of β -Al₂O₃ exist; two of them, β -Al₂O₃ (Na₂O*11Al₂O₃) and β'' -Al₂O₃ (Na₂O*5Al₂O₃), form in the binary system Na₂O-Al₂O₃, and can incorporate MgO. The other two beta aluminas, β''' -Al₂O₃ and β'''' -Al₂O₃ are found in the ternary system Na₂O-Al₂O₃-MgO [28]. For completeness it should be mentioned that the existence of a β' -Al₂O₃ (Na₂O*7Al₂O₃) has been reported as well, but subsequent literature is in agreement

that β' -Al₂O₃ is actually β -Al₂O₃ with excess Na₂O [28].

The formation and stability of β -Al₂O₃ has been extensively studied in the literature because its excellent ion conductivity makes it suitable for applications as a solid electrolyte; especially for use in batteries. Most reported preparation routes involve sodium carbonate and alumina [30,31,83]. Heating mixtures of alumina and sodium carbonate to 1100°C leads to the formation of β'' -Al₂O₃, which decomposes to β -Al₂O₃ and NaAlO₂ at temperatures >1500°C. The equilibrium vapor pressure of Na₂O over β -Al₂O₃ has been reported to be "appreciable" at temperatures >1400°C [30], where β -Al₂O₃ can decompose to α -Al₂O₃ by volatilization of Na₂O. However, soda loss has been reported to occur at lower temperatures as well, e.g. 6.4 wt% of soda loss was reported by de Vries and Roth [31] when they prepared β'' -alumina samples and heated it for 4 h at 1100 °C. On the other hand, Gallup [39] investigated the stability of β -Al₂O₃ at high temperatures and under different atmospheres and he reported that β -Al₂O₃ can convert to α -Al₂O₃ at temperatures as low as 1300°C in hydrogen or vacuum atmosphere, but in air no conversion was observed for heating as long as 1 h at 1500°C. Full conversion was observed when the material was heated for 10 min at 1600°C.

Even though the conditions for the formation of β -Al₂O₃ in α -Al₂O₃ ceramics are of great importance, especially because the Na₂O content in Bayer process Al₂O₃ is sufficient for the formation of β -Al₂O₃, it is barely studied in literature. Duncan and Creyke [84] investigated the formation and stability of β -Al₂O₃ in α -Al₂O₃ ceramics and used two commercial alumina powders with impurities of 0.038 wt% SiO₂, 0.006 wt% MgO and 0.061 ppm Na₂O, and 0.04 wt% SiO₂, 0.2 wt% MgO and 0.04 wt% Na₂O, respectively. They reported that β -Al₂O₃ can form at Na₂O concentrations as low as 300 ppm if a small amount of MgO is present. They estimated the amount of β -Al₂O₃ by measuring the dielectric loss of the sample, since β -Al₂O₃ was observed to increase the dielectric loss of α -Al₂O₃ samples. An increase in amount of β -Al₂O₃ was observed with increasing Na₂O, but also with increasing MgO additions, and it was shown by electron-probe microanalysis that there is a higher concentration of Na₂O and MgO in the β -Al₂O₃ grains. They state that samples, in which β -Al₂O₃ forms, show no formation of spinel [84] and furthermore they determined that β -Al₂O₃ in α -Al₂O₃ is stable to up to 1650 °C in stagnant air. In a flowing air stream, however, decomposition to α -Al₂O₃ takes place, even in the center of the sample and the decomposition is facilitated by

open porosity and higher temperatures, whereas a high degree of compaction of the powder, e.g. a high green density, impedes the decomposition. Small amounts of other oxides (e.g. SiO_2 , MgO , ZrO_2) are reported to facilitate the decomposition process due to an easier diffusion path through the grain boundaries. The work by Duncan and Creyke focuses on the decomposition and while some literature reports indicate under what conditions $\beta\text{-Al}_2\text{O}_3$ may form [84], there is no systematic study on the formation of $\beta\text{-Al}_2\text{O}_3$ as function of powder chemistry, at what sintering stage $\beta\text{-Al}_2\text{O}_3$ forms and what possible formation mechanisms are. Goal of this work is to identify the stages and mechanisms of $\beta\text{-Al}_2\text{O}_3$ formation in $\alpha\text{-Al}_2\text{O}_3$.

5.2 Experimental

The samples fabricated for the investigations in Chapters 2 and 3 were used to investigate the formation of $\beta\text{-Al}_2\text{O}_3$ in $\alpha\text{-Al}_2\text{O}_3$. To investigate the influence of MgO concentration on the formation of $\beta\text{-Al}_2\text{O}_3$ the MgO -free powder used in Chapter 2 was also doped with up to 1000 ppm MgO using magnesium nitrate hexahydrate ($\text{Mg}(\text{NO}_3)_2 \cdot 6\text{H}_2\text{O}$, 99.97%, Alfa Aesar, Ward Hill, MA, USA). The alumina powder was dispersed in aqueous magnesium nitrate solution and stirred on a magnetic stir plate for 5 h at room temperature, and then held at 80 °C for 24 h until the mixture was too viscous to stir. The mixture was then placed in a drying oven at 100 °C for 24 h to thoroughly dry the powder. Additionally, an ultra-high purity powder (AKP-50, Sumitomo Chemical Co. Ltd., Tokyo, Japan) was doped with up to 2000 ppm Na_2O , 500 ppm SiO_2 , and 500 ppm MgO and used to dry press samples. The intrinsic impurities in the ultra high purity powder are 11 ppm SiO_2 , 4 ppm Fe_2O_3 , 2 ppm Na_2O , 2 ppm MgO , and 1 ppm Cu . The doping and sample preparation procedure is described in detail in chapters 2 and 3.

5.3 Results

Initially the detection of $\beta\text{-Al}_2\text{O}_3$ in an $\alpha\text{-Al}_2\text{O}_3$ matrix was investigated. Figure 5.1a-c shows SEM micrographs of $\beta\text{-Al}_2\text{O}_3$ grains in a sample with 529 ppm Na_2O , 103 ppm SiO_2 , and 380 ppm MgO sintered at 1525°C for 3 h. It can be seen that in unetched samples $\beta\text{-Al}_2\text{O}_3$ grains can hardly be observed in images obtained from secondary electrons (Figure 5.1a). Figure 5.1b shows an SEM image of the

same area of the sample as Figure 5.1a obtained from the backscattered electrons and a stronger contrast between the β -Al₂O₃ grains and the surrounding α -Al₂O₃ matrix can be seen, which is due to the higher sensitivity of backscattered electrons to density. β -Al₂O₃ grains appear darker due to the lower density (3.31 g/cm³) compared to α -Al₂O₃ (3.986 g/cm³). Figure 5.1c shows a β -Al₂O₃ grain after thermal etching at 1425°C for 40 min and it can be seen that the β -Al₂O₃ grain has evaporated during thermal etching, leaving a platelet shaped hole in the etched microstructure. It is interesting to note that samples with low Na₂O concentrations such as 29 ppm form β -Al₂O₃ grains that do not evaporate during thermal etching, as seen in Figure 5.1d. SEM micrographs obtained from backscattered electrons were used to detect β -Al₂O₃ grains for the following investigations.

5.3.1 Influence of MgO on the formation of β -Al₂O₃

Figure 5.2a shows the influence of MgO concentration on the number of β -Al₂O₃ grains after sintering at 1525°C for 3 h. It can be seen that for a MgO concentration of 2 ppm no β -Al₂O₃ was observed, and with increasing the MgO concentration the number of β -Al₂O₃ grains that form increases up to 502 ppm MgO, but does not increase further when the MgO concentration is increased to 1002 ppm. This shows that MgO assists the formation of β -Al₂O₃. The influence of Na₂O concentration on the number of β -Al₂O₃ grains in MgO-free Bayer alumina after sintering at 1525°C for 3 h is shown in Figure 5.2b. It can be seen that only a small number of β -Al₂O₃ grains form for concentrations \leq 529 ppm Na₂O, but for higher concentrations, such as 1029 ppm, the number of β -Al₂O₃ grains increases significantly. Since commercial Bayer aluminas are typically doped with MgO, the following investigations are focused on Bayer alumina powder that was doped with 380 ppm MgO.

5.3.2 MgO-doped Bayer alumina

5.3.2.1 Number frequency of β -Al₂O₃ grains

Figure 5.3 shows the influence of the Na₂O and SiO₂ concentration on the number density of β -Al₂O₃ grains in Bayer alumina powder doped with 380 ppm MgO. It can be seen that the number density of β -Al₂O₃ grains increases with increasing Na₂O concentration (Figure 5.3a), but decreases as a function of SiO₂ concentration

in samples with different Na_2O concentrations (Figure 5.3b). This indicates that the $\text{Na}_2\text{O}/\text{SiO}_2$ ratio determines the number density of $\beta\text{-Al}_2\text{O}_3$ grains. Figure 5.3c shows the number density of $\beta\text{-Al}_2\text{O}_3$ grains as a function of the $\text{Na}_2\text{O}/\text{SiO}_2$ ratio, and it can be seen that the number density of $\beta\text{-Al}_2\text{O}_3$ grains increases linearly with increasing $\text{Na}_2\text{O}/\text{SiO}_2$ ratio.

The kinetics of $\beta\text{-Al}_2\text{O}_3$ formation at 1525°C for different powder chemistries (MgO-doped Bayer alumina) is shown in Figure 5.4. Most $\beta\text{-Al}_2\text{O}_3$ grains forms within the first hour at 1525°C, and after that the number density of $\beta\text{-Al}_2\text{O}_3$ grains does not change for all chemistries. In contrast, for samples prepared from ultra high purity powder (AKP-50) the amount of $\beta\text{-Al}_2\text{O}_3$ that forms during sintering in the temperature range from 1450°C to 1600°C for up to 8 h does not change, regardless of the Na_2O , MgO, or SiO_2 concentrations. However, in the ultra-high purity powder it was observed that increasing the Na_2O and MgO concentrations increases the number of $\beta\text{-Al}_2\text{O}_3$ grains in the microstructures, and increasing the SiO_2 concentration decreases the number of $\beta\text{-Al}_2\text{O}_3$ grains in the microstructures, similar to the Bayer alumina powder.

5.3.2.2 Size of $\beta\text{-Al}_2\text{O}_3$ grains

Figure 5.5 shows micrographs of samples with different powder chemistries with up to 1000 ppm MgO, Na_2O , and SiO_2 after sintering at 1525°C for 3 h. It can be seen that the size of the $\beta\text{-Al}_2\text{O}_3$ grains changes as a function of powder chemistry. Samples with 1000 ppm MgO, 1000 ppm SiO_2 , and 29 ppm Na_2O form 30-40 μm long $\beta\text{-Al}_2\text{O}_3$ grains (Figure 5.5a). The $\beta\text{-Al}_2\text{O}_3$ grains that form in samples with 2 ppm MgO, 1000 ppm SiO_2 , and 1000 ppm Na_2O are 10-20 μm long (Figure 5.5b), and the $\beta\text{-Al}_2\text{O}_3$ grains in samples with 1000 ppm MgO, 1000 ppm SiO_2 , and 1000 ppm Na_2O are 4-10 μm long (Figure 5.5c). Note that no $\beta\text{-Al}_2\text{O}_3$ was observed in samples with 29 ppm Na_2O and 2 ppm MgO, regardless of the SiO_2 concentration.

Micrographs of MgO-doped (380 ppm) Bayer alumina with Na_2O concentrations of up to 1060 ppm Na_2O sintered at 1525°C for 3 h are shown in Figure 5.6. The $\beta\text{-Al}_2\text{O}_3$ grains are 3-13 μm long for samples with 185 ppm Na_2O and 4-10 μm for samples with 560 ppm Na_2O , and if the Na_2O concentration is increased to 1060 ppm the $\beta\text{-Al}_2\text{O}_3$ grains are significantly smaller (2-7 μm).

Micrographs of samples with 185/182 ppm $\text{Na}_2\text{O}/\text{SiO}_2$ and 560/182 ppm $\text{Na}_2\text{O}/\text{SiO}_2$ after sintering at 1525°C for 3 h are shown in Figure 5.7. The Na_2O

concentrations in those samples are the same as in the samples in Figure 5.6a and b, respectively. However, the samples in Figure 5.7 contain 100 ppm more SiO₂. It can be seen that higher SiO₂ concentrations lead to larger β -Al₂O₃ grains compared to samples with lower SiO₂ concentrations.

Figure 5.8 shows micrographs of MgO-doped (380 ppm) Bayer alumina samples with 560 ppm Na₂O and 82 ppm SiO₂ after heating for 0 h, 1 h, and 8 h. It can be seen that the size of the β -Al₂O₃ grains does not change as a function of sintering time. However, as shown in Figure 5.4, the number of the β -Al₂O₃ grains increases with increasing sintering time.

Figure 5.9 show the XRD pattern of a polished sample with 1060 ppm Na₂O, 582 ppm SiO₂ and 380 ppm MgO after sintering at 1525°C for 5 h. The pattern shows that there is a small amount of β -Al₂O₃ present with P6₃/mmc crystal structure, which can be assigned to β -Al₂O₃. The estimated amount of β -Al₂O₃ from the XRD pattern is 0.6 wt.%. EDS reveals that the β -Al₂O₃ grains contain higher concentrations of MgO and Na₂O compared to the surrounding matrix.

Since the type of β -Al₂O₃ that forms is known a theoretical volume fraction of β -Al₂O₃ can be estimated based on the chemical formula of β -Al₂O₃ (Na₂O*11Al₂O₃) and the amount of Na₂O in the samples, as seen in Table 5.1. The size of the β -Al₂O₃ grains was measured from the SEM images (length and thickness) and an area fraction was estimated. The estimated area fraction is assumed to be equal to the volume fraction of β -Al₂O₃ in the sample. It can be seen that the theoretically estimated amount of β -Al₂O₃ that can form based on the amount of Na₂O in the samples is higher than the observed amount of β -Al₂O₃ in the samples. A possible explanation is that some amount of Na₂O might volatize during sintering, as shown in Chapter 3. Taking into account that 35% of the Na₂O might volatize during heating (Figure 3.12 Chapter 3), the expected amount of β -Al₂O₃ in the samples is close to the observed amount of β -Al₂O₃, as seen in Table 5.1.

5.3.3 Interpretation and mechanisms of formation

TEM and EDS analysis showed that insoluble impurities and dopants such as Na₂O, MgO, CaO and SiO₂ segregate to the grain boundaries. In general it can be assumed that second phases can form when the solubility of impurities and dopants in the bulk and in the grain boundaries is exceeded. In the MgO-free powder it can

be seen that no second phase forms for Na_2O concentrations of 29 ppm, and only a very small amount of β - Al_2O_3 forms in samples with 529 ppm Na_2O . When the Na_2O concentration is increased to 1029 ppm the amount of β - Al_2O_3 that forms increases drastically (Figure 5.2b). This indicates that the solubility of Na_2O in the grains and grain boundaries in the MgO -free alumina is \sim 500 ppm Na_2O (note the presence of 103 ppm SiO_2 in the MgO -free powder). For higher Na_2O concentrations the grain boundaries supersaturate during sintering and β - Al_2O_3 forms. If the SiO_2 concentration in MgO -free powder samples is increased no β - Al_2O_3 forms and we believe that SiO_2 significantly increases the Na_2O solubility in the grain boundaries by forming a liquid grain boundary phase. The argument that SiO_2 increases the solubility of Na_2O in the grain boundaries is further supported by the observation that a considerable number of β - Al_2O_3 grains form in the ultra high purity powder with 502 ppm Na_2O , 2 ppm MgO and 11 ppm SiO_2 , as seen in Figure 5.10, whereas almost no β - Al_2O_3 grains were observed in MgO -free Bayer alumina samples with 529 ppm Na_2O , 2 ppm MgO , and 103 ppm SiO_2 .

When the MgO concentration in Bayer alumina is increased β - Al_2O_3 forms at significantly lower Na_2O concentrations, e.g. at Na_2O concentrations as low as 29 ppm. The amount of β - Al_2O_3 that forms increases with increasing MgO concentration up to 502 ppm. We believe that this is because MgO removes SiO_2 from the grain boundaries during sintering, as explained earlier, and this mechanism significantly decreases the solubility of Na_2O in the grain boundaries, leading to the nucleation of β - Al_2O_3 .

If it is assumed that MgO and SiO_2 form the defect complex proposed earlier, and if it is assumed that MgO and SiO_2 go into solid solution at equal amounts and that all MgO is consumed by this process, MgO -doped powder samples (380 ppm MgO) with 82 and 182 ppm SiO_2 do not have any SiO_2 left in the grain boundaries. This reduction in the amount of SiO_2 in the grain boundaries reduces the solubility of Na_2O in the grain boundaries significantly, leading to the precipitation of β - Al_2O_3 . Samples with 582 ppm SiO_2 have 202 ppm SiO_2 left in the grain boundaries after 380 ppm MgO and SiO_2 co-dissolve into the alumina lattice, and the solubility of Na_2O in the grain boundaries is still high enough so that only few β - Al_2O_3 grains in this sample, due to the presence of 202 ppm SiO_2 .

The process of SiO_2 and MgO co-dissolving into the alumina lattice and the formation of β - Al_2O_3 happens at the same time, between 0 and 3 h at 1525°C,

which supports the hypothesis that β -Al₂O₃ nucleates and grows as a result of supersaturation of the grain boundaries when MgO removes SiO₂ from the grain boundaries. However, samples with 560 ppm Na₂O and 82 ppm SiO₂ form more β -Al₂O₃ than samples with 560 ppm Na₂O and 182 ppm SiO₂, even though no SiO₂ should be in the grain boundaries for both samples. One reason could be that not all 380 ppm MgO and SiO₂ are consumed by this co-dissolution process, and a small amount SiO₂ might remain on the grain boundaries, which would increase the Na₂O solubility.

Another possible explanation is that MgO has an additional effect on the formation of β -Al₂O₃ in α -Al₂O₃. It has been reported that MgO supports the formation of β -Al₂O₃ in alumina, and samples with 560 ppm Na₂O and 82 ppm SiO₂ have 100 ppm more MgO left in the grain boundaries than samples with 560 ppm Na₂O and 182 ppm SiO₂. Since EDS shows that MgO is in the β -Al₂O₃ grains MgO might facilitate the formation of β -Al₂O₃.

5.4 Summary

Table 5.1. Estimated amount of β -Al₂O₃ in MgO-doped (380 ppm) Bayer alumina samples after 3 h at 1525°C.

Concentration of Na ₂ O in the sample (ppm)	Theoretical vol.% of β -Al ₂ O ₃		Measured amount of β -Al ₂ O ₃ 3h 1525°
	No Na ₂ O volatizes	Assuming 35 % of Na ₂ O volatizes	
60	0.14	0.09	0.18
185	0.42	0.28	0.25
310	0.71	0.46	0.38
560	1.28	0.84	0.65
1060	2.42	1.58	0.49

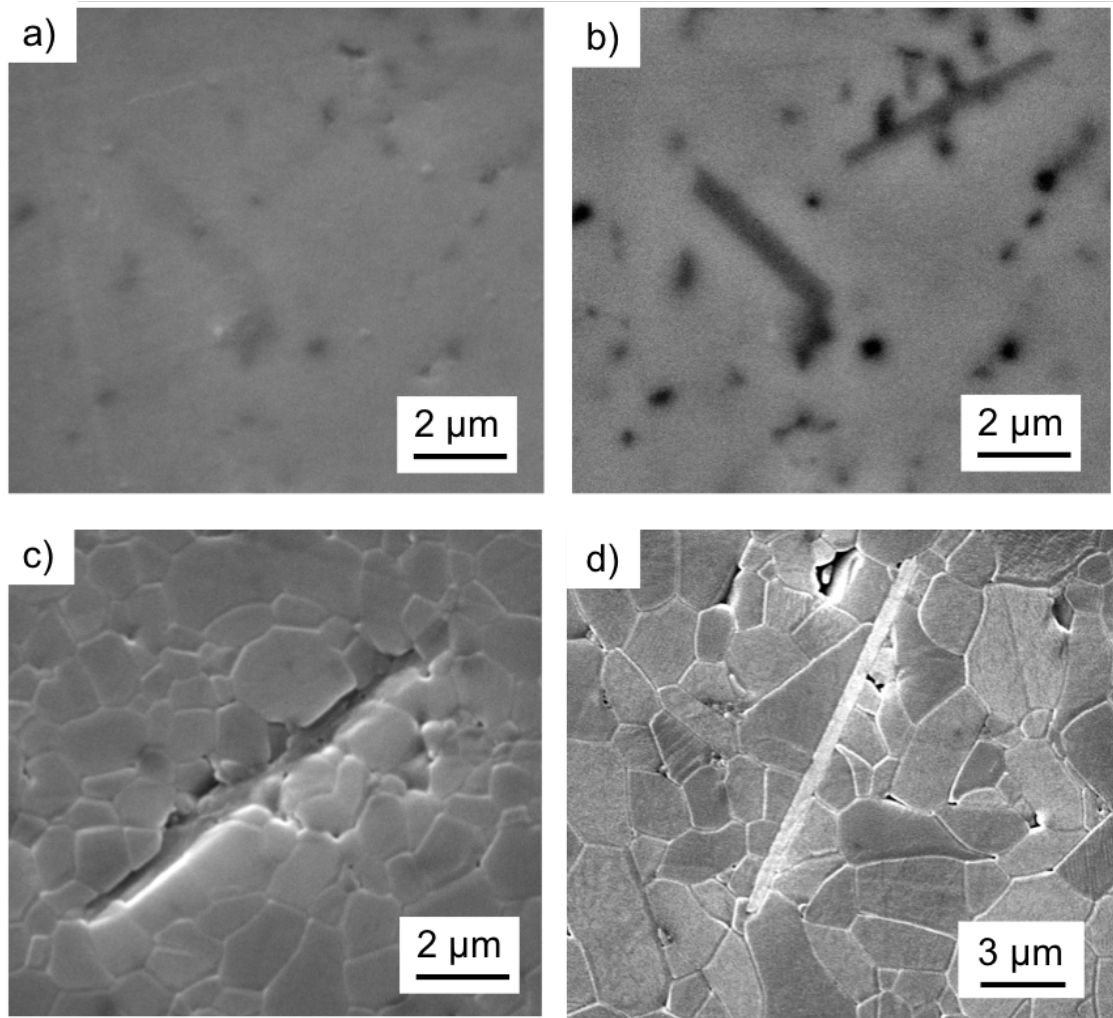


Figure 5.1. SEM micrographs of β - Al_2O_3 grains in a-c) Bayer alumina with 560 ppm Na_2O , 82 ppm SiO_2 , and 380 ppm MgO after 3 h at 1525°C and d) Bayer alumina with 29 ppm Na_2O , 103 ppm SiO_2 , and 502 ppm MgO after 3 h at 1525°C. The samples in a) and b) were not etched and the samples in c) and d) were etched. a), c), and d) were obtained using a secondary electron detector, and b) was obtained using a backscattered electron detector.

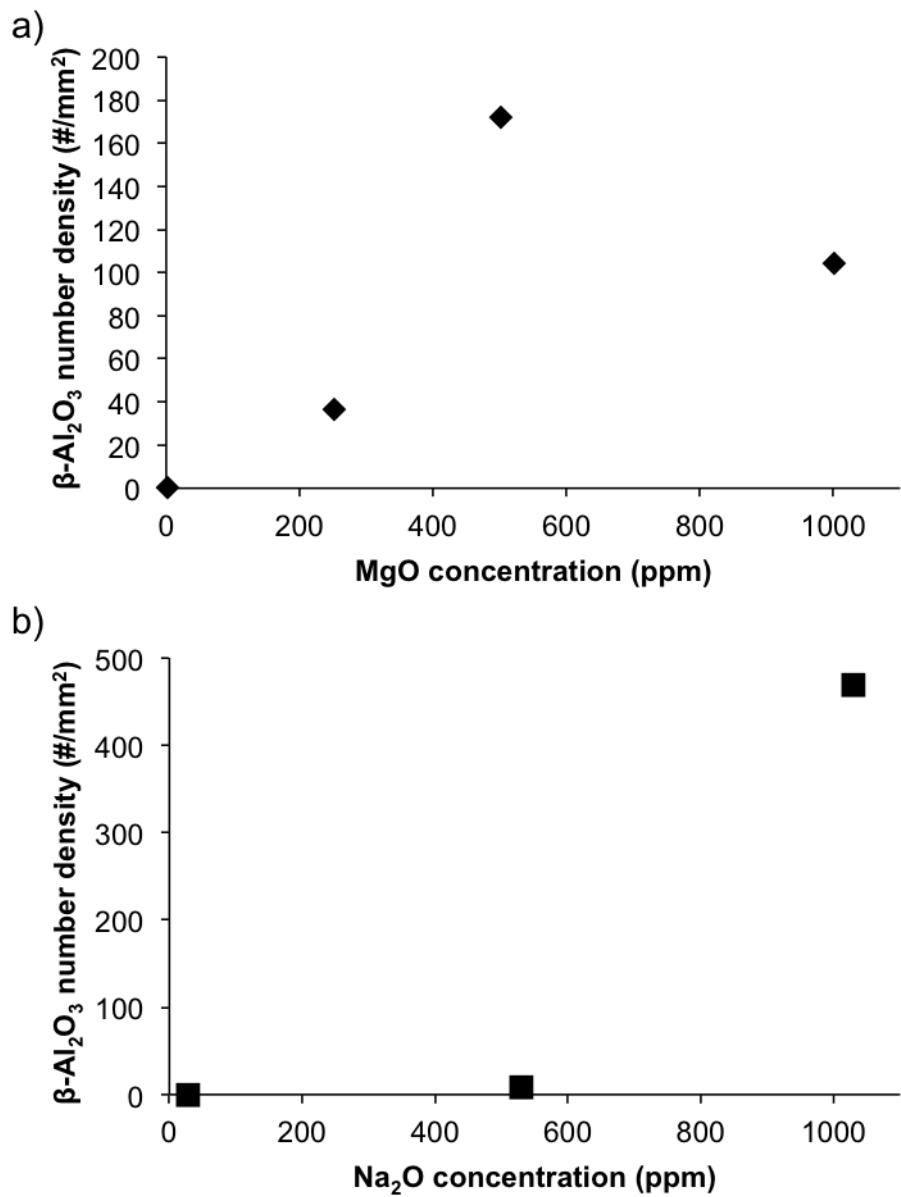


Figure 5.2. Formation of β -Al₂O₃ in MgO-free powder samples as a function of a) MgO concentration and b) Na₂O concentration in samples after 3 h at 1525°C.

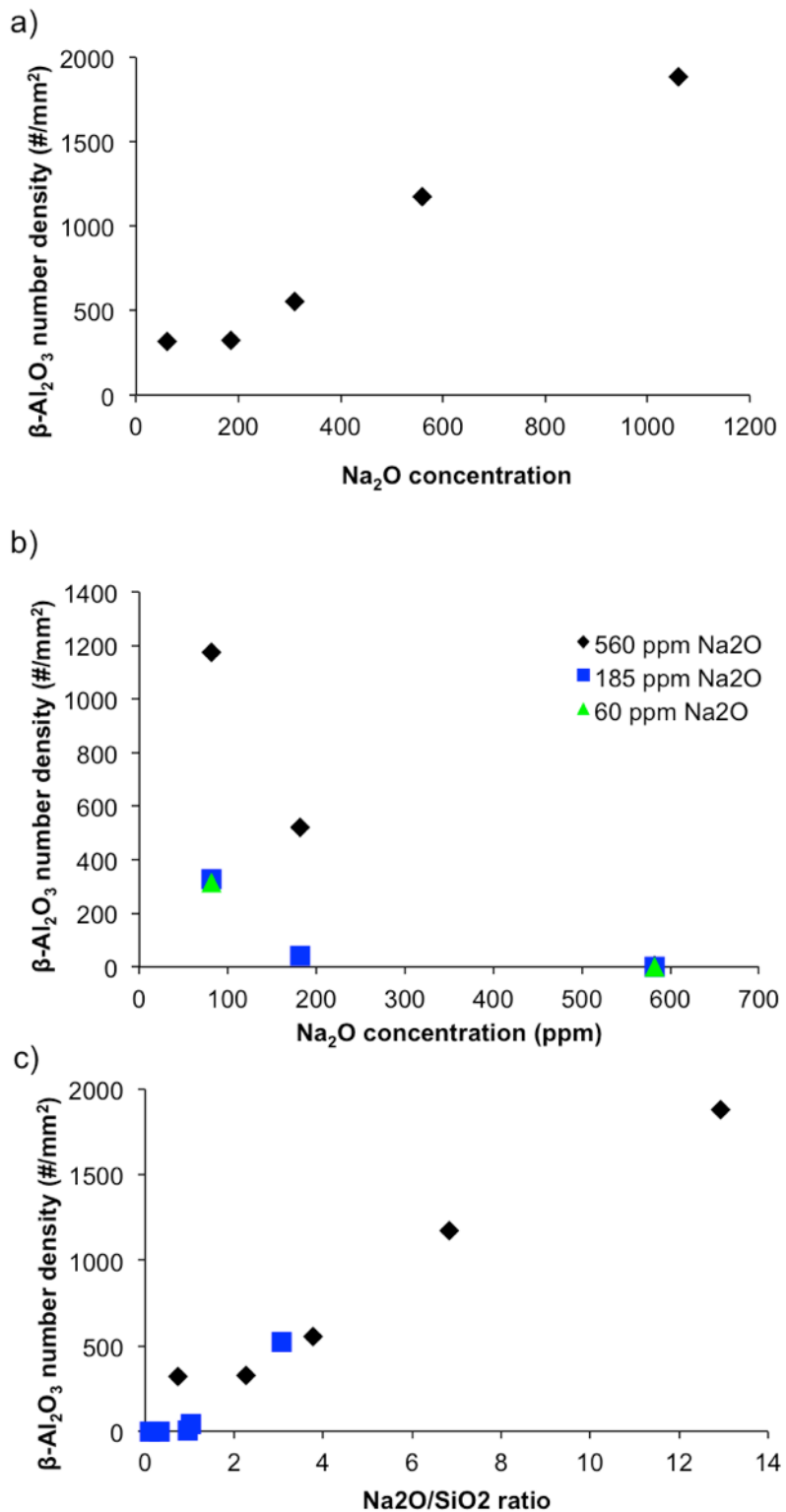


Figure 5.3. Formation of β -Al₂O₃ a function of a) Na₂O concentration, b) SiO₂ concentration for different Na₂O concentrations, and c) of the Na₂O/SiO₂ ratio in MgO-doped (380 ppm) powder samples. In c) the black diamonds are samples with 82 ppm SiO₂ and the blue squares are samples with 182 and 582 ppm SiO₂.

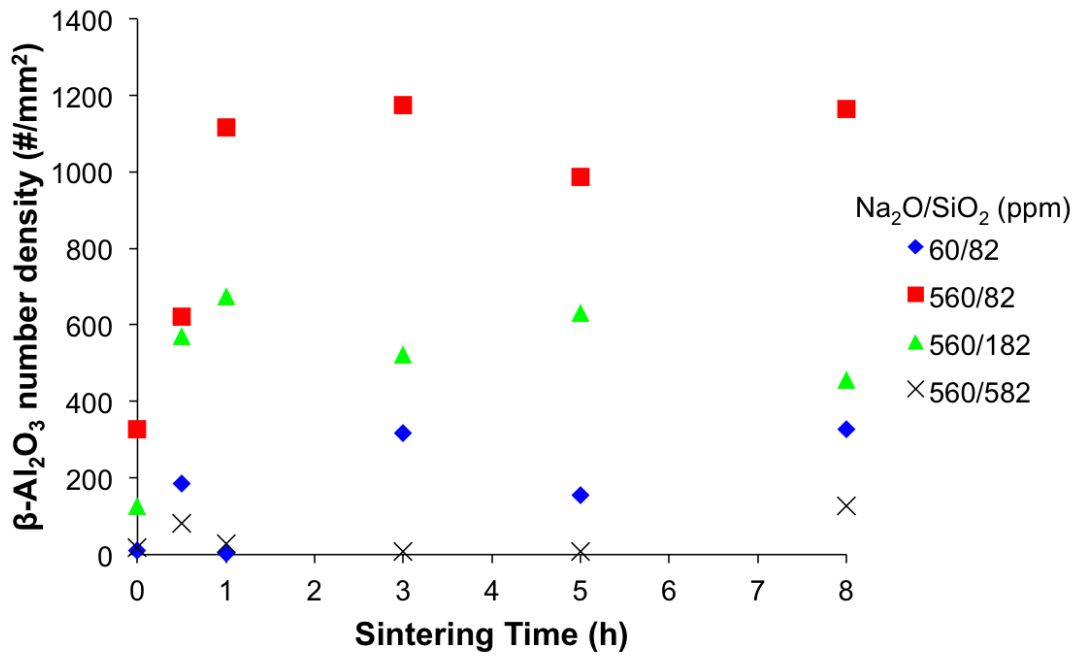
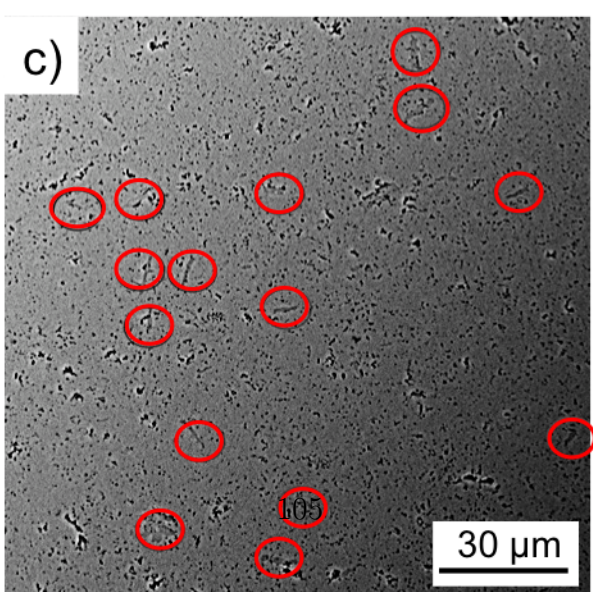
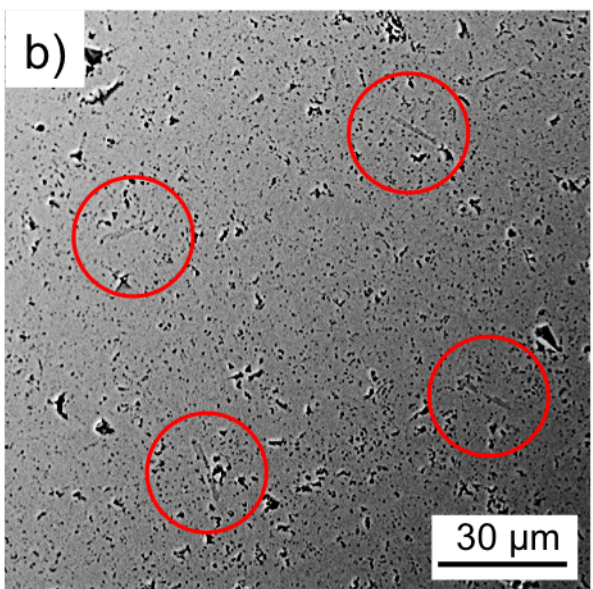
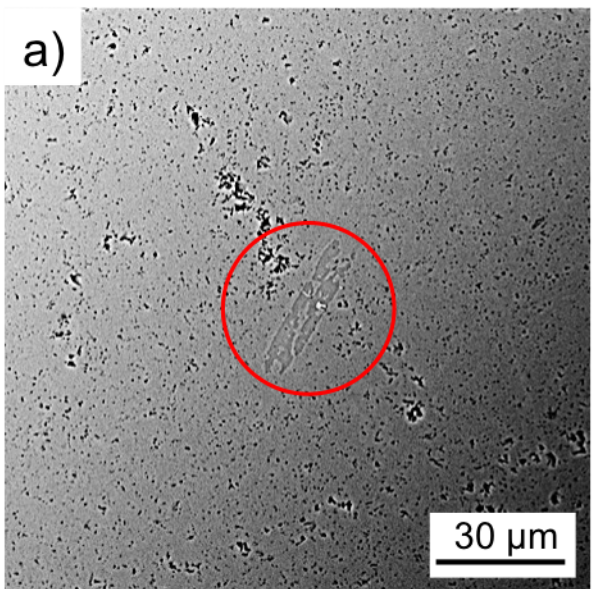
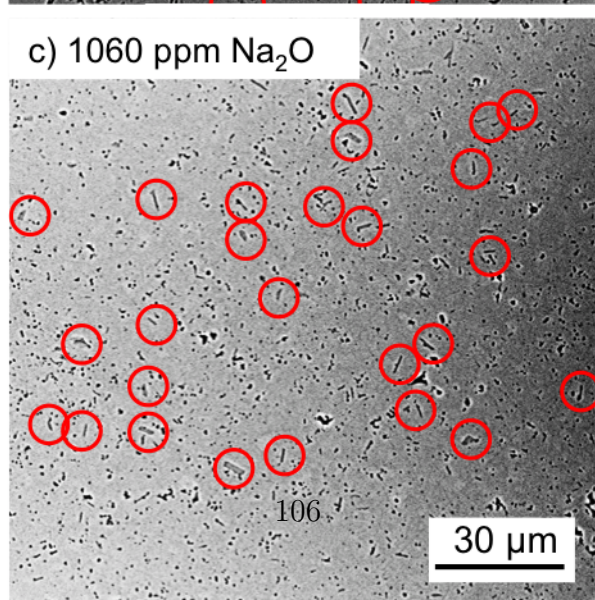
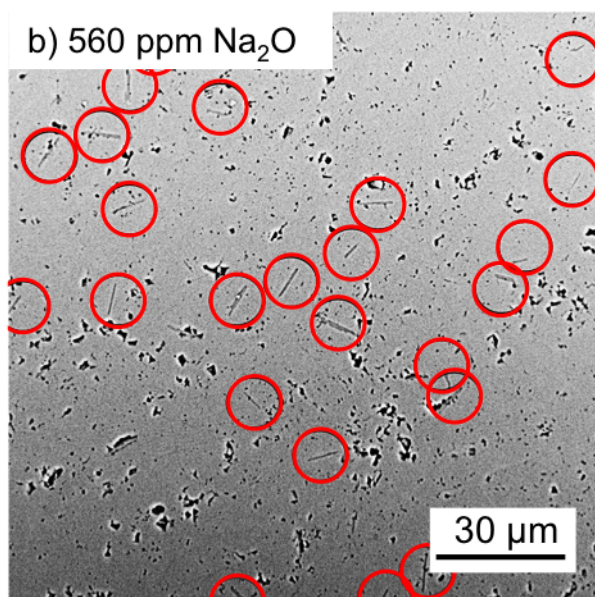
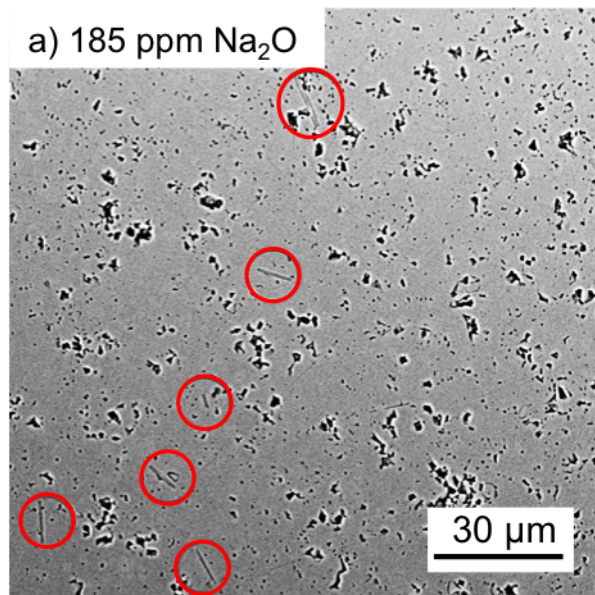


Figure 5.4. Kinetics of β -Al₂O₃ formation for different powder chemistries of MgO-doped powder samples (380 ppm MgO).





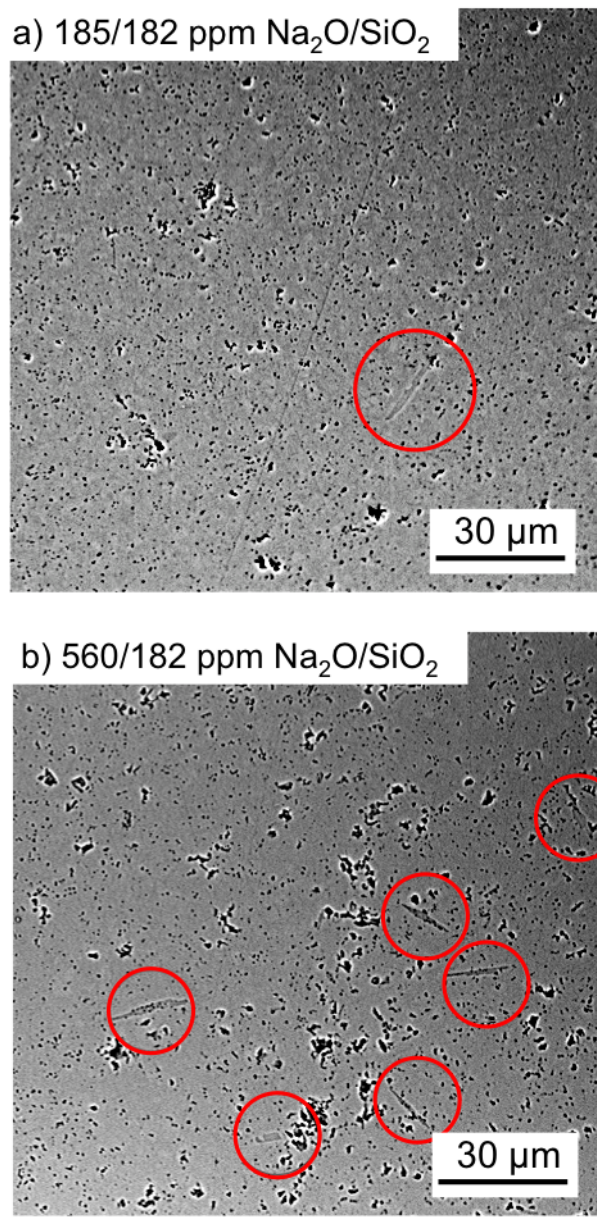
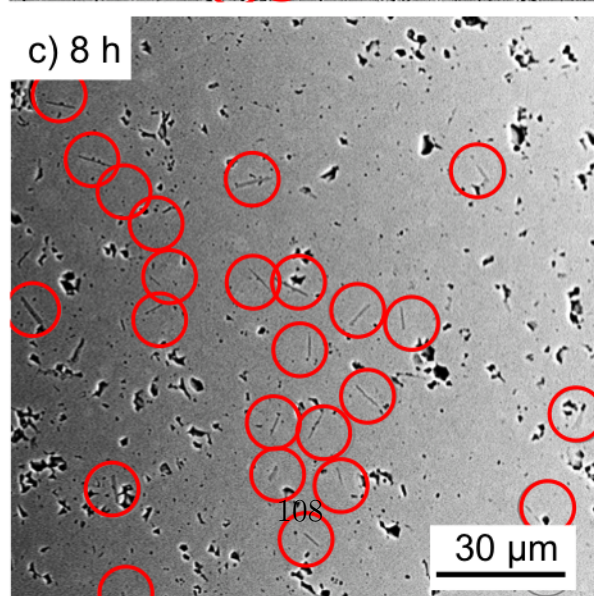
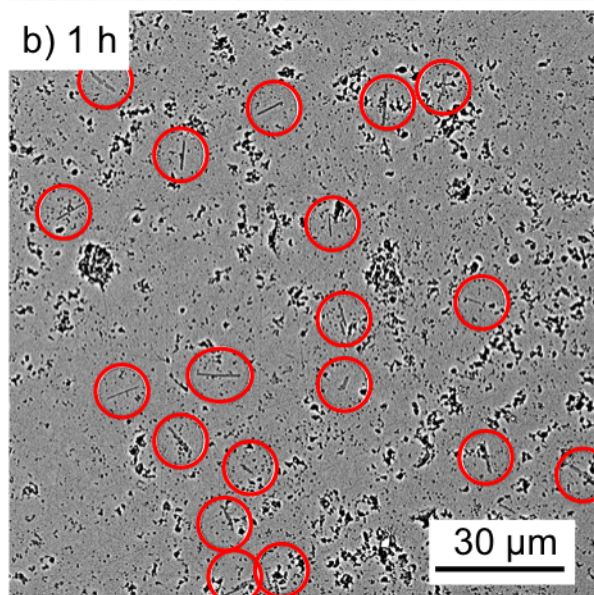
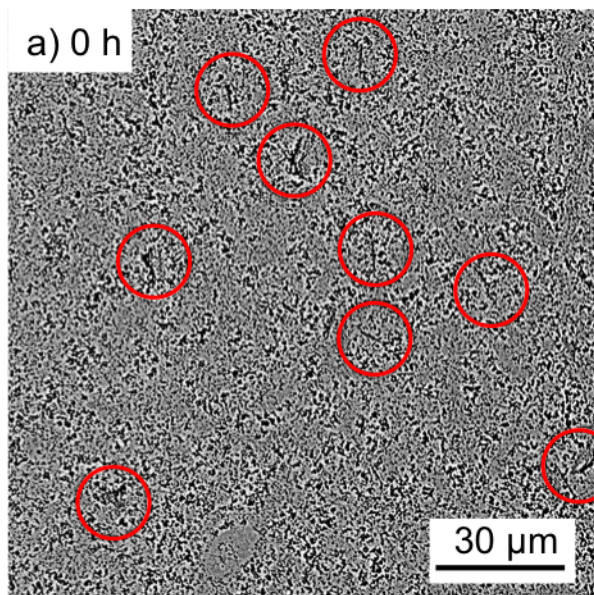


Figure 5.7. Micrographs showing β -Al₂O₃ grains (red circles) in MgO-doped (380 ppm) Bayer alumina samples with a) 185/182 ppm Na₂O/SiO₂ and b) 560/182 ppm Na₂O/SiO₂ after sintering at 1525°C for 3 h.



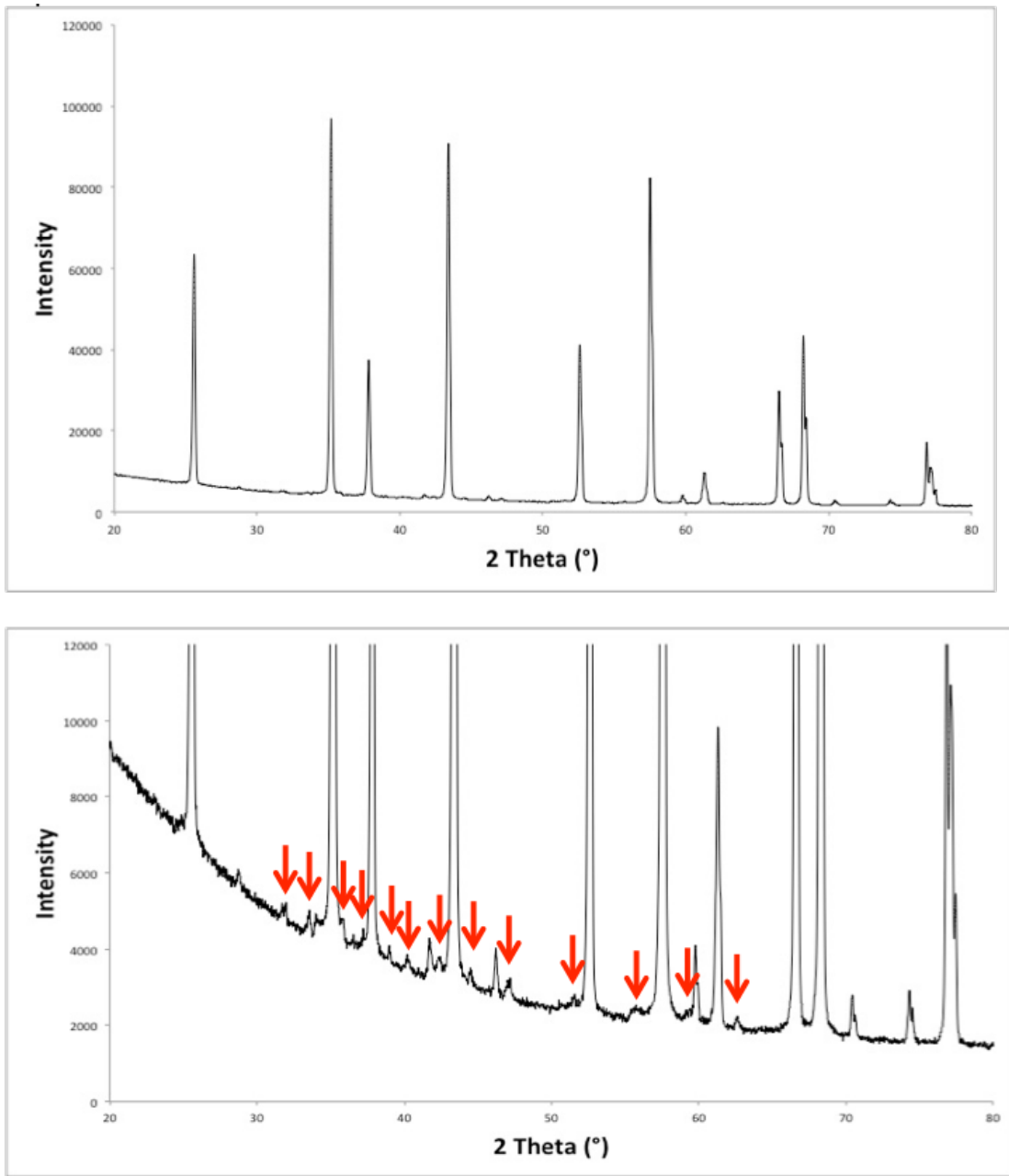


Figure 5.9. XRD pattern of a sample with 1060 ppm Na₂O, 82 ppm SiO₂, and 380 ppm MgO after sintering at 1525°C for 5 h. The red arrows indicate the peaks that can be assigned to β -Al₂O₃. The other peaks can be assigned to α -Al₂O₃.

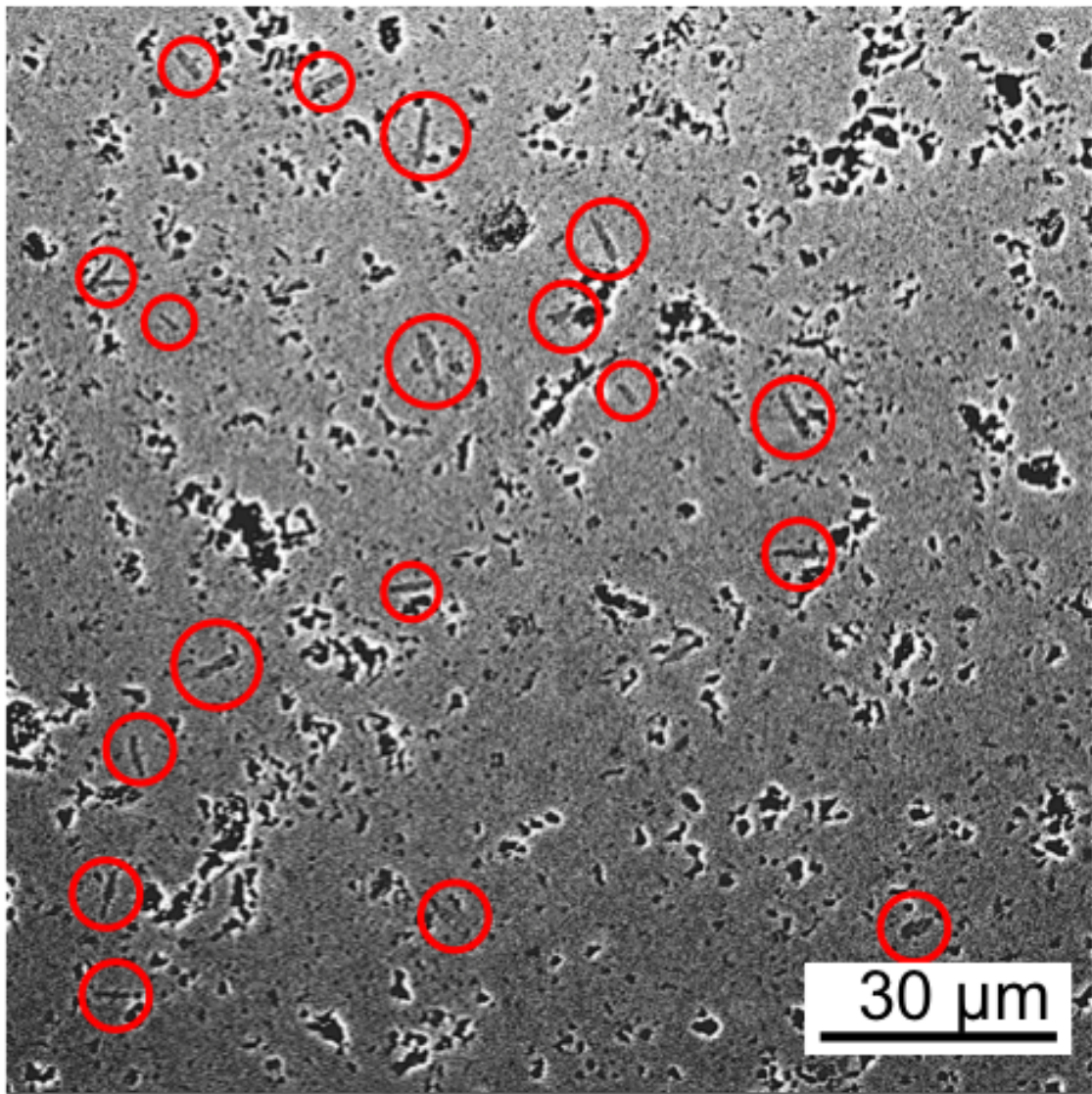


Figure 5.10. Micrograph showing β -Al₂O₃ grains (red circles) in an ultra high purity powder sample with 502 ppm Na₂O, 2 ppm MgO, and 11 ppm SiO₂ after sintering at 1525°C for 0 h.

Chapter 6 |

A Critique of the Master Sintering Curve Analysis of Sintering Processes

6.1 Introduction

The master sintering curve (MSC) approach was developed by Su and Johnson [85] to generalize the densification profile of a sintering powder with a single curve for the entire sintering time/temperature. The MSC approach is based on a combined-stage sintering model developed by Hansen et al, [86] given as:

$$\frac{1}{\rho} \frac{d\rho}{dt} = \frac{3\gamma\Omega}{k_B T} \left(\frac{\delta D_b \Gamma_b}{G^4} + \frac{D_v \Gamma_v}{G^3} \right) \quad (6.1)$$

where ρ is relative density of the powder compact, $d\rho/dt$ is densification rate, γ is surface energy, Ω is molar volume, k_B is Boltzmann's constant, T is absolute temperature, G is grain size, D is diffusion coefficient, δ is grain boundary thickness, and Γ is a geometric scaling factor. The subscripts b and v represent grain boundary and volume diffusion mechanisms, respectively. The MSC is derived by simplifying the combined-stage sintering model (Eq. 6.1) to account for only a single diffusion mechanism, and by considering diffusion as thermally-activated via an activation energy Q . The resulting equation is given as:

$$\frac{1}{\rho} \frac{d\rho}{dt} = \frac{3\gamma\Omega}{k_B T} \left(\frac{D\Gamma}{G^n} \right) \quad (6.2)$$

where

$$D = D_0 e^{-Q/RT} \quad (6.3)$$

and R is the ideal gas constant. Eq. 6.2 is re-written to collect microstructural parameters on the left hand side and temperature dependent parameters on the right hand side:

$$\frac{k_B G^n}{3\rho\gamma\Omega\Gamma D_0} \frac{d\rho}{dt} = \frac{1}{T} \exp\left(-\frac{Q}{RT}\right) = \frac{d\Theta}{dt} \quad (6.4)$$

Eq. 4 can be integrated to give:

$$\frac{k_B}{\gamma\Omega\Gamma D_0} \int_{\rho_0}^{\rho} \frac{(G(\rho))^n}{3\rho\Gamma(\rho)} d\rho = \int_0^t \frac{1}{T} \exp\left(-\frac{Q}{RT}\right) dt = \Theta \quad (6.5)$$

Equation 6.5 describes the sintering behavior for an arbitrary time-temperature profile, and the integral over this profile (the right hand side of Eq. 6.4) is termed the work of sintering Θ . The MSC is obtained by plotting ρ versus Θ . The left hand side of Eq. 6.4 is not solved, as many of the included parameters are unknown. However, as long as these parameters are independent of time and temperature, data plotted in this way will collapse into a single continuous curve for the correct value of Q . In practice, Q is a fitting parameter for which the best-fit MSC is obtained by determining the minimum mean residual. Assuming arbitrary values for Q in Eq. 6.5, the mean residual square is calculated by [87–89]

$$\text{Mean residual square} = \sqrt{\frac{1}{\rho_s - \rho_0} \int_{\rho_0}^{\rho_s} \frac{\sum_{i=1}^N \left(\frac{\Theta_i}{\Theta_{avg}} - 1 \right)^2}{N} d\rho} \quad (6.6)$$

where N is the number of experimental data points, and Q_{avg} is the average of all Q_i over N . The Q value that yields the minimum mean residual square is the Q value at which the MSC trajectories obtained from the densification curves at different heating rates yield the best fit and converge onto a single curve. Because of the mechanistic nature of the model, the Q value is usually referred to as the activation energy for sintering.

A large body of literature exists on MSC analysis for different ceramic powders and forming techniques. For alumina, the Q values reported in the literature vary drastically. In Su and Johnson's original work [85] Q values of 440 and 488

kJ/mol were determined by shrinkage rate analysis and minimum mean residuals, respectively, for an ultrafine ultrahigh purity alumina (AKP-50, Sumitomo Chemical America, Inc.). Using the same powder, Tatami et al. [90] determined a Q of 555 kJ/mol , and if the powder is doped with 2000 ppm MgO , a Q of 880 kJ/mol was determined. Pouchly et al. [91] estimated the activation energies of two different ultrahigh purity alumina powder compacts (Taimicron TM-DAR, Taimei Chemicals and RC-HP DBM, Reynolds Chemicals) to be 770 and 640 kJ/mol , respectively, and attributed the difference in Q to the difference in particle size of 110 nm and 240 nm, respectively. The influence of the forming technique on Q of alumina was investigated by Aminzare et al., [92] who obtained Q values of 700 and 605 kJ/mol for samples prepared by dry pressing and pressure filtration, respectively (Taimicron TM-DAR, Taimai Chemicals). Using the same alumina powder (Taimicron TM-DAR, Taimai Chemicals), Guillon and Langer [93] determined a Q of 290 kJ/mol densified by spark plasma sintering and attributed the very low Q to the high heating rates of 35 - 150 $^{\circ}\text{C}/\text{min}$. Q values of up to 1064 kJ/mol were reported by Shao et al. [94] for granulated and dry pressed alumina powder (350 nm, 99.9%, Dalian Luming Nanometer Material Ltd.), and they explained the higher values with the lower heating rates of 0.5 and 5 $^{\circ}\text{C}/\text{min}$. The effect of heating rate on the activation energy of sintering has been well studied, and a number of reasonable mechanistic explanations of this effect can be found in the literature [95, 96].

Based on this review of Q values for alumina powders and values for other ceramic powders, it is obvious that Q can vary significantly depending on forming method and powder chemistry, and even for the same powder. Also, the value of Q is usually reported as the activation energy for sintering with little, or no, mechanistic explanation for the variability of value compared other Q values. Thus, it is not clear if these differences can be quantified and analyzed by MSC analysis in a meaningful way. To examine the impact of the forming technique on the MSC we prepared alumina samples by isopressing, slip casting and tape casting. To examine how changes in sintering mechanism affect the MSC analysis, we studied a series of Na_2O -doped aluminas that we reported in an earlier paper. In this work we systematically investigate how shrinkage anisotropy, relative density, forming technique, and powder chemistry affect Q and the shape of the MSC. Based on these experiments we discuss the limitations of the MSC approach and describe how MSC can be used in a constructive way to predict the sintering of a specific

powder.

6.2 Experimental Procedure

Commercially available alpha-alumina (CT3000LS-SG, Almatis, Inc., Leetsdale, PA) powder was used to prepare samples for MSC analysis. The alumina powder was doped with up to 1000 ppm Na₂O using sodium acetate (NaC₂H₃O₂*₃H₂O, ACS grade, BDH, West Chester, PA) to investigate the influence of Na₂O concentration on the MSC. The detailed doping procedure is reported in previous work [44].

Samples were prepared from as-received and doped alumina powders using a range of forming techniques. Two sets of samples were prepared by uniaxial dry pressing. For one set the as-received powder was sieved to -106 µm and uniaxially dry pressed at 30 MPa. For the second set, the powder was granulated by dispersing it in ethanol and 5wt.% polyethylene glycol (PEG). After ball milling for 24 h, the dried powder sieved to -105 µm and samples were lightly pressed at 30 MPa.

For tape casting a slurry was prepared by ball milling 68.14 wt.% alumina powder with 15.31 wt.% xylene, 15.31 wt.% ethanol, and 1.24 wt.% Menhaden fish oil. After 24 h 3.09 wt.% polyvinyl butyral (PVB), 1.55 wt.% polyalkylene glycol (PAG) and 1.55 wt.% butyl benzyl phthalate (BBP) were added and the mixture was ball milled for another 24 h, before 1 drop of cyclohexane per 20 g of alumina powder was added and the slurry was stirred for an additional 45 min. The slurry was tape cast on a silicone-coated MylarTM carrier tape using a doctor blade gap height of 305 µm. After drying the tape was cut, stacked, uniaxially pressed at 70°C for 10 min and then isostatically laminated at 74°C and 20 MPa for 30 min.

For non-aqueous slip casting 65.3 wt.% powder was dispersed in xylene with 2 wt.% Menhaden fish oil was ball milled for 24 h and slip cast into a mold consisting of a PVC tube (1 inch diameter) and a plaster of Paris plate.

For aqueous slip casting 76 wt.% alumina powder was dispersed in deionized water mixed with 3 wt.% Darvan C. The pH of the Darvan and water mixture was adjusted to 11 using 5 M NH₄OH before the alumina powder was added. The slurry was ball milled for 24 h and then slip cast into a mold consisting of a PVC tube and a plaster of Paris plate.

The polymer processing aids in all samples were burned out by heating at 600°C in air for 12 h and then the samples were cold isostatically pressed at 200 MPa

(CIP, Autoclave Engineers, Erie, PA). The samples were subsequently cut and ground into 3x3x15 mm³ bars for dilatometry studies. The bars were heated at 5, 10, and 20°C/min up to 1600°C in a thermomechanical analyzer (TMA; Linseis PT1600, Robbinsville, NJ) to record the linear shrinkage of the samples. The thermal expansion contribution to the dilatometry curves was subtracted out of the measurement using the cooling curves of the samples measured in the TMA.

6.3 Results and Discussion

6.3.1 Anisotropy

Figure 6.1 shows the dilatometry curves of slip cast samples heated to 1525°C at 5, 10, and 20°C/min. The shrinkage was measured in 2 directions; along the z-direction, i.e., the direction along which the capillary force acts during slip casting, and along the x/y-direction, perpendicular to the capillary force. Differential shrinkage was observed between the z-direction and the x/y-directions, for all heating rates. Anisotropic shrinkage is commonly observed in slip cast parts since the capillary force causes the particles in the slurry to orient during slip casting. It should be noted that the degree of anisotropy strongly depends on the particle morphology and forming technique. For samples that were prepared by forming techniques, such as slip casting or tape casting, anisotropic shrinkage has to be taken into account during the MSC analysis, otherwise the densities calculated from the dilatometry data alone are inaccurate, which leads to inaccuracy in the calculated value of activation energy Q and the shape of the MSC.

The anisotropic shrinkage can be characterized by an anisotropy factor k , which is the ratio of the shrinkage in the z-direction and the shrinkage in x/y-direction. Figure 6.2 illustrates how k changes as a function of relative density for the slip cast samples heated at different heating rates.

Relative density was calculated as a function of temperature using the directional measurements (Figure 3.1), as shown in Figure 6.3. The MSC can be determined using Eq. 6.5 if the activation energy Q is known. To determine Q , Figure 6.4 shows the mean residuals calculated as a function of Q (Eq. 6.6) and the minimum mean residuals for this sample occurs at $Q = 550$ kJ/mol. The relatively sharp minimum provides evidence that a single MSC curve provides a good fit for the

measured TMA data.

Since sintering is a thermally activated process, the activation energy at a particular relative density can be determined by iso-density analysis, i.e. by plotting $\ln(-T \frac{d\rho}{dt})$ vs. $1/T$ and determining the slopes of the resulting linear curves at given relative densities. Figure 6.5 shows the activation energies obtained from iso-density analysis between 59 and 85% relative density, and an average activation energy of 568 kJ/mol is obtained, which is close to the Q obtained from the minimum mean residuals.

The MSCs for both Q values of 550 kJ/mol and 568 kJ/mol are illustrated in Figure 3.6 and both MSCs fit the trajectories of the different heating rates well. For comparison, Figure 3.7 shows the MSC of the same sample, taking into account only the shrinkage in the x/y direction and assuming isotropic shrinkage (no correction for anisotropy). In this case Q (determined by mean residuals) increases to 625 kJ/mol. This example demonstrates the importance of correcting for anisotropic shrinkage when Q and the MSC are determined. Note that the final densities of the samples discussed above are $\leq 90\%$, because the MSC curves obtained from different heating rates diverge at higher densities, and influence Q , as discussed below.

6.3.2 MSC at high densities

Figure 6.8a shows the densification curves of dry pressed samples sintered up to 1600°C at different heating rates and Figure 6.8b shows the mean residuals of apparent activation energies. The minimum mean residuals were determined at $Q = 700$ kJ/mol and Figure 6.8c shows the resulting MSC. It can be seen that $Q = 700$ kJ/mol gives a good fit at low densities, but the trajectories diverge at densities $>85\%$. Figure 6.9 shows the development of the apparent activation energy obtained from iso-density analysis, Q_{iso} , and it can be seen that Q_{iso} is ~ 700 kJ/mol and increases slightly with increasing relative density. At densities $>85\%$ Q_{iso} increases somewhat more rapidly, and at densities $>95\%$ Q_{iso} increases drastically up to >1800 kJ/mol. This change in Q_{iso} explains the divergence of the MSC trajectories obtained from the different heating rates using $Q_{res} = 700$ kJ/mol. At densities $<90\%$ the activation energy obtained from the minimum mean residuals Q_{res} , which is used to obtain the MSC, is reasonably close to the

activation energies obtained from iso-density analysis, Q_{iso} , resulting in a good fit at all heating rates. However, at densities $>90\%$ the values of Q_{iso} are >100 kJ/mol greater than the Q_{res} value used to construct the MSC, which causes the trajectories to diverge as a function of heating rate. Although the idea of variable activation energy is relatively simple, it is not physically realistic to consider that Q is intrinsically a function of ρ . It is more likely that this increase in Q_{iso} and the divergence of the MSC at high densities is caused by microstructural or mechanistic changes that are not accounted for in the MSC model. Without being able to take these changes into account, we find MSC analysis to be insufficient to describe final stage sintering at densities $>90\%$.

6.3.3 Quantification of the MSC shape

The shape of the MSC is related to the evolution of the microstructural parameters the left hand side of Eq. 6.5 and the development of the microstructural evolution can be quantitatively described by:

$$C = \frac{k_B G^n}{3\gamma\Omega\Gamma D_0} \quad (6.7)$$

With rearranging Eq. 6.4 C can be determined as a function of relative density:

$$C = \rho \frac{d\Theta}{d\rho} \quad (6.8)$$

Figure 6.10 shows C as a function of relative density and it can be seen that C increases over 5 orders of magnitude between 57% and 98% relative density. This increase in C with relative density is partially due to coarsening of the powder during sintering. A 8-fold increase in average grain size was observed during sintering to 98% relative density. Assuming that grain boundary diffusion controls densification ($n=4$), the coarsening of the microstructures accounts for an increase in C of ~ 3.5 order of magnitude. The remaining ~ 2 orders of magnitude increase in C are most likely due to an increase in Γ , since it is a function of relative density and the only parameter that is expected to change considerably.

6.3.4 Influence of forming technique

Samples were prepared from the as-received powder using different forming techniques to investigate the influence of forming technique on the MSC. Figure 6.11 shows the corresponding MSC curves for samples heated up to 1525°C. It is clear that Q changes as a function of forming technique, which is in part due to different green densities. The sample prepared by non-aqueous slip casting has a green density of 59% and the lowest Q (550 kJ/mol), followed by the sample prepared by aqueous slip casting with a green density of 58% and a Q of 650 kJ/mol. The samples prepared by dry pressing (no PEG) and tape casting have green densities of 57% and 55%, respectively, and both samples have a Q of 730 kJ/mol. The dry pressed sample with 5 wt.% PEG has a green density of 55% and the highest activation energy with 810 kJ/mol. It can be observed that Q decreases as the green density increases and that the shape and position of the MSC changes as a function of forming technique (Figure 6.11). However, these changes are not straightforward. For example, the samples prepared by tape casting and dry pressing with 5 wt.% PEG have the same green density of 55%, but different Q values of 730 kJ/mol and 810 kJ/mol, respectively, and different MSC shapes.

6.3.5 Influence of powder chemistry

Figure 6.12 shows the MSCs of samples doped with different amounts of Na₂O prepared by non-aqueous slip casting. It can be seen that Q changes as a function of Na₂O concentration and increases from 550 kJ/mol for samples with no Na₂O additions to 700 and 730 kJ/mol for samples with 250 and 500 ppm Na₂O additions, respectively. Q decreases to 690 kJ/mol when the concentration is further increased to 1000 ppm additional Na₂O. The position of the MSC changes as a function of Na₂O concentration, and the shape of the MSC changes as the Na₂O concentration of the as-received powder is increased by 250 ppm, but does not change as the Na₂O concentration is increased further. The effect of Na₂O concentration on the MSC is not straightforward, but becomes more clear when the influence of Na₂O on the sintering behavior as reported earlier is considered. For example, the increased sintering onset temperature for samples with higher Na₂O concentrations results in a high Q and causes the shape and position of the MSC to change. Furthermore, changes in the microstructure that were observed as a function of

Na_2O concentration are not considered in the MSC analysis.

The above discussion shows that a variety of factors such as forming technique and powder chemistry affect not only the value of Q , but also the shape of the MSC. As explained earlier, the shape of the MSC is determined by the microstructural development, which is described by the factor C . Therefore, the different powder chemistries and different forming techniques lead to a different microstructural development, which implies that the microstructural development is not only a function of relative density, as assumed for MSC analysis. Therefore, the MSC is insufficient to explain fundamental changes in sintering behavior due to changes in forming technique or chemistry, and MSC analysis is insufficient to characterize the influence of the chemistry on the sinterability of a powder.

6.3.6 Prediction of densities

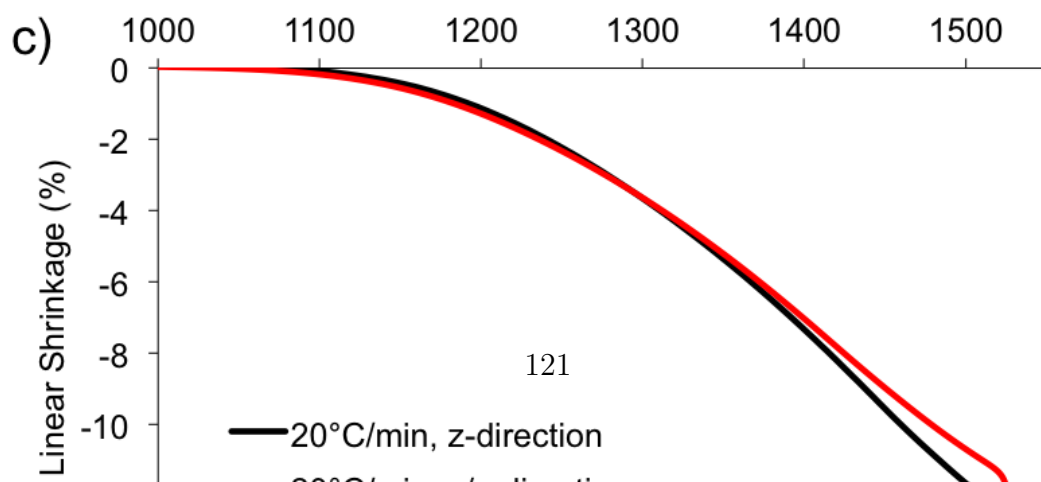
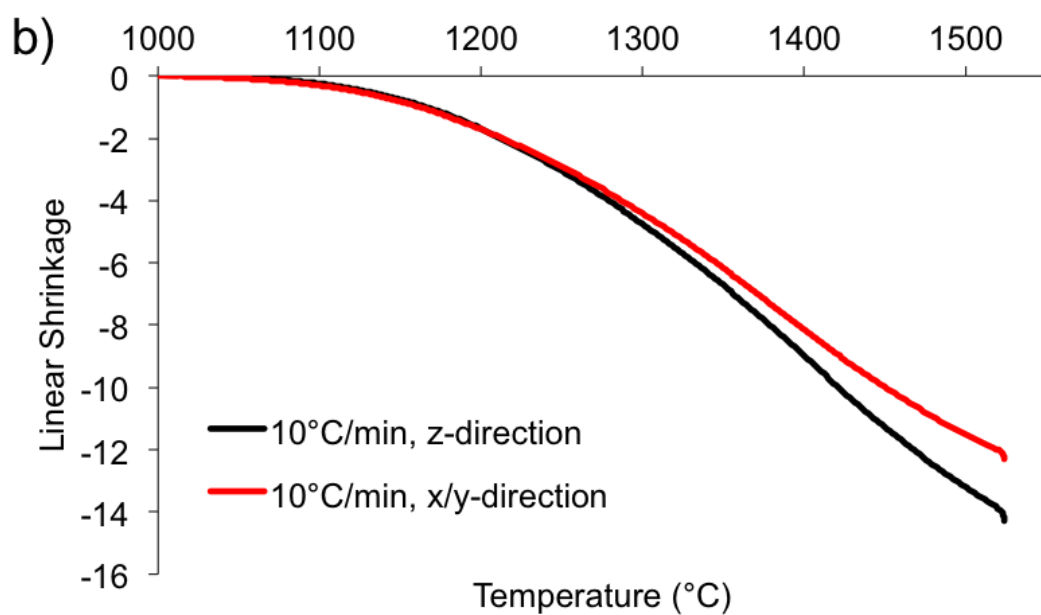
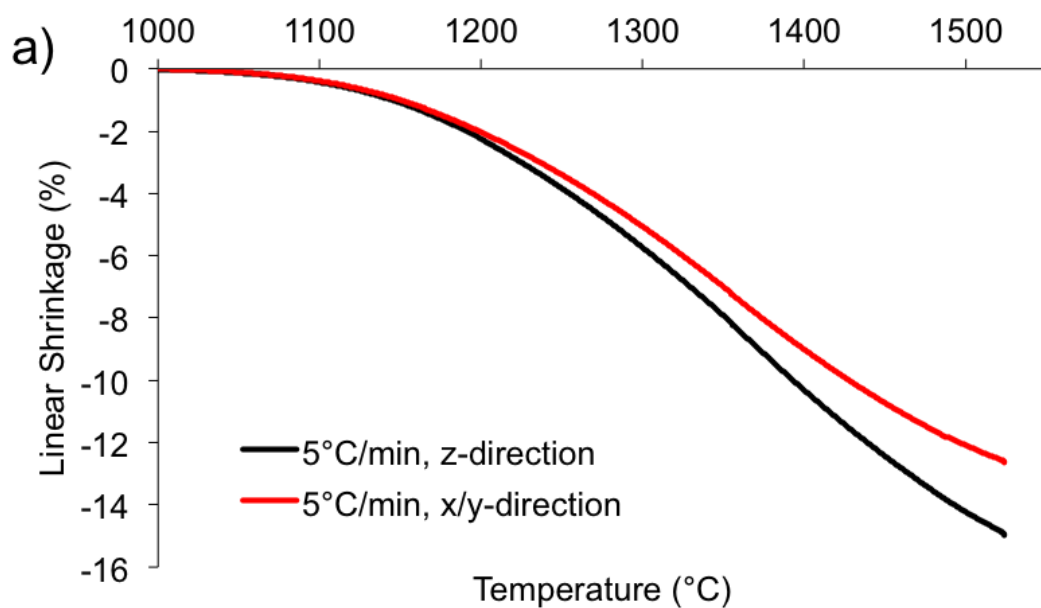
One of the main objectives of MSC analysis is to predict the density of samples prepared from a given powder using a given forming technique after the MSC is established for this powder and forming technique. The MSC data provided above and Eq. 6.5 can be used to construct equivalent time/temperature diagrams to predict the density of samples for known heating conditions. An example for this is shown in Figure 6.13 for dry pressed samples and a heating rate of $10^\circ\text{C}/\text{min}$. The contours shown in Figure 6.13 indicate the equivalent relationships between particular time/temperature treatments and relative densities of 80, 85, 90, and 95%. For example, a relative density of 85% is reached after heating a dry pressed sample at $10^\circ\text{C}/\text{min}$ to 1460°C and no hold time. The same density is reached after heating a dry pressed sample from the same powder at $10^\circ\text{C}/\text{min}$ to 1400°C and holding it at this temperature for 29 min. It should be noted that the predicted MSC response for $>90\%$ sintered density has a larger error due to the discrepancies we noted above for MSC data analysis at $>90\%$ density.

6.4 Conclusions

1. MSC analysis is very susceptible to over interpretation. MSC analysis results in two pieces of information; an activation energy Q and the MSC curve itself. Caution must be exercised when interpreting the so-called activation energy,

since processing history and powder chemistry affect Q and the shape of the MSC curve. Therefore, comparing Q between different chemistries is not sufficient to interpret fundamental changes in sintering behavior. The MSC is only useful to characterize sintering behavior of a ceramic powder formed in a specific way.

2. Q is reasonable for describing intermediate stage sintering behavior because microstructural changes are minimal. At final sintering stage the trajectories diverge and Q is only useful for comparisons for a single powder.
3. Therefore, the most accurate method to take anisotropic shrinkage into account is to measure the shrinkage in different directions relative to the acting forces during forming. Anisotropic shrinkage of samples must be taken into account to obtain accurate MSCs and values for Q .
4. MSC is very useful for predicting equivalent time/temperature conditions for densification. However, it should be emphasized that such predictions are only valid for sinters that were prepared from the same powder as the samples to generate the MSC, and prepared by the same forming technique as the samples to generate the MSC.



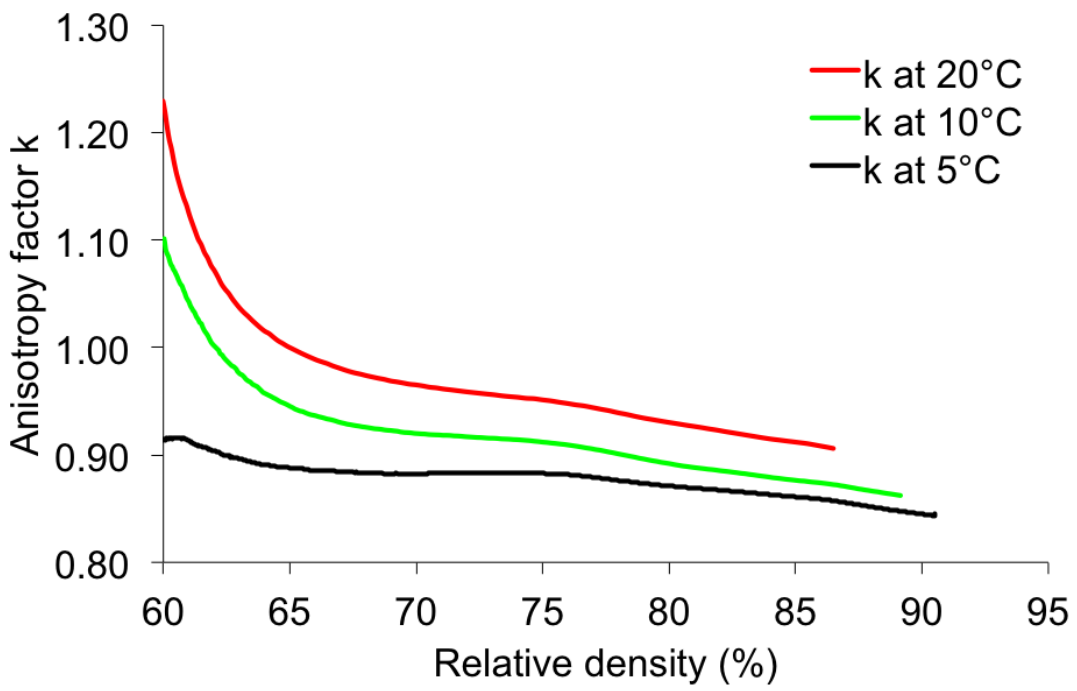


Figure 6.2. Development of the anisotropy factor for shrinkage, k , as a function of relative density for CT3000LS-SG samples heated at different rates.

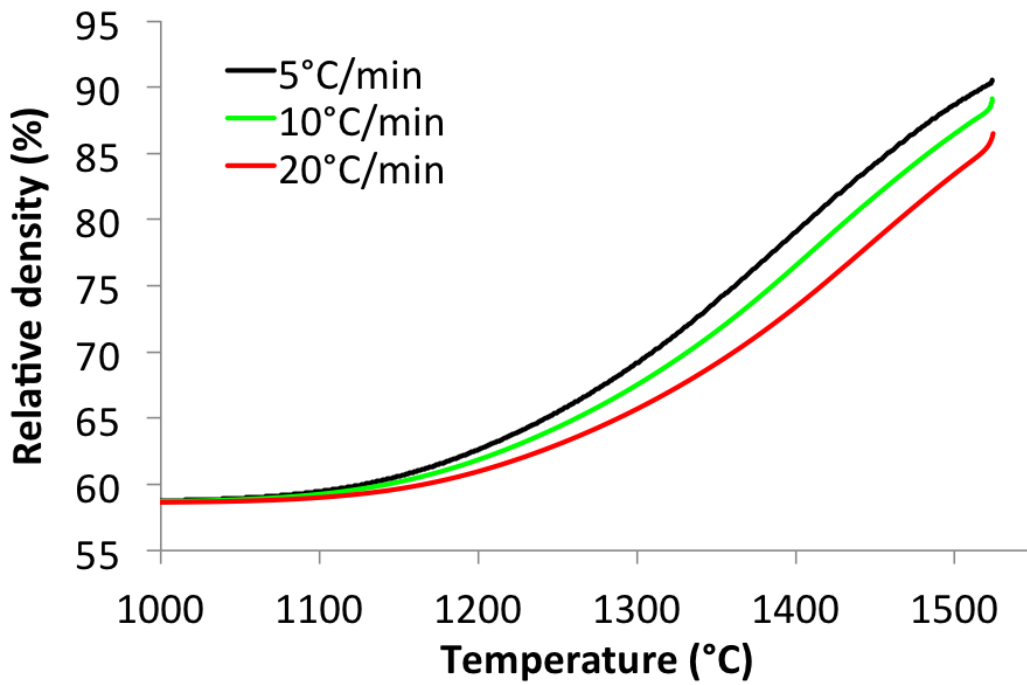


Figure 6.3. Development of the relative density corrected for anisotropy as a function of temperature for slip cast CT3000LS-SG samples for different heating rates.

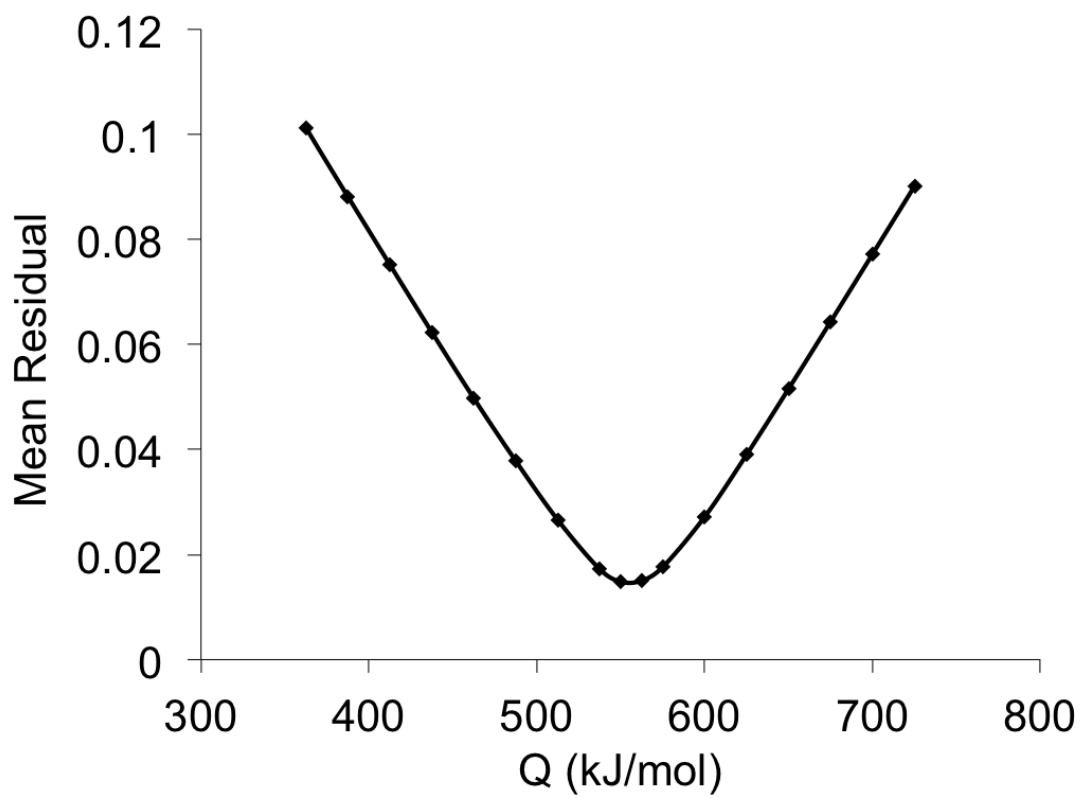


Figure 6.4. Mean residuals of the MSC curves assuming different values for the activation energy Q for slip cast CT3000LS-SG samples.

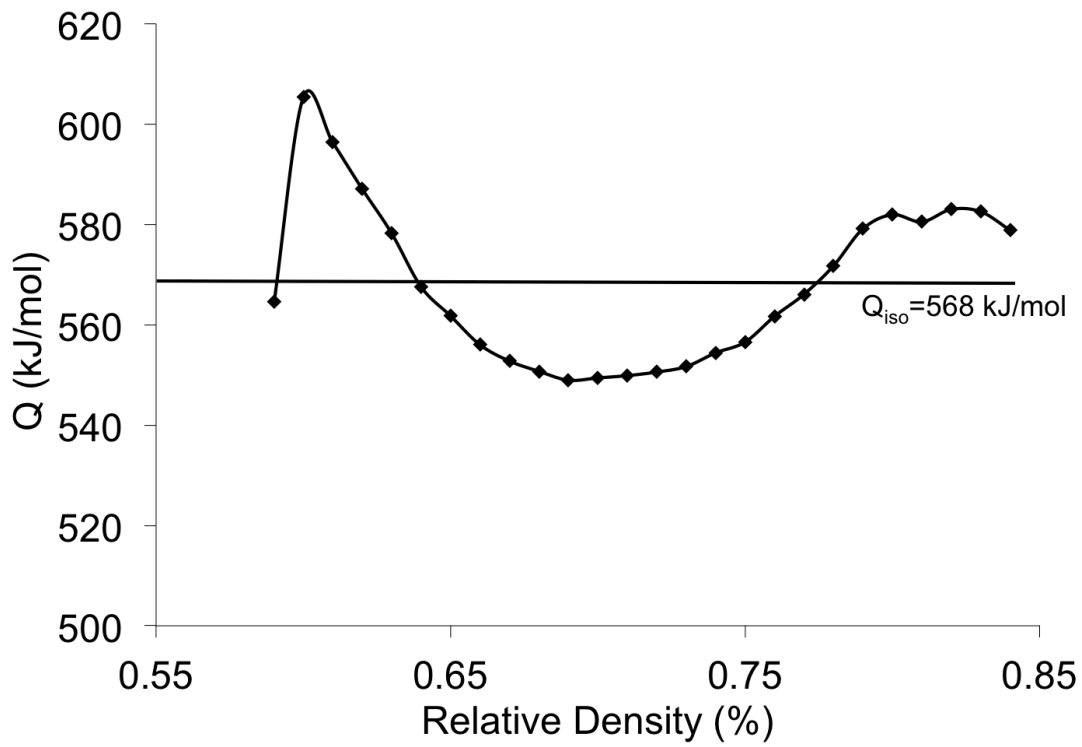


Figure 6.5. Apparent activation energy of slip cast CT3000LS-SG samples obtained from anisotropy-corrected iso-density analysis.

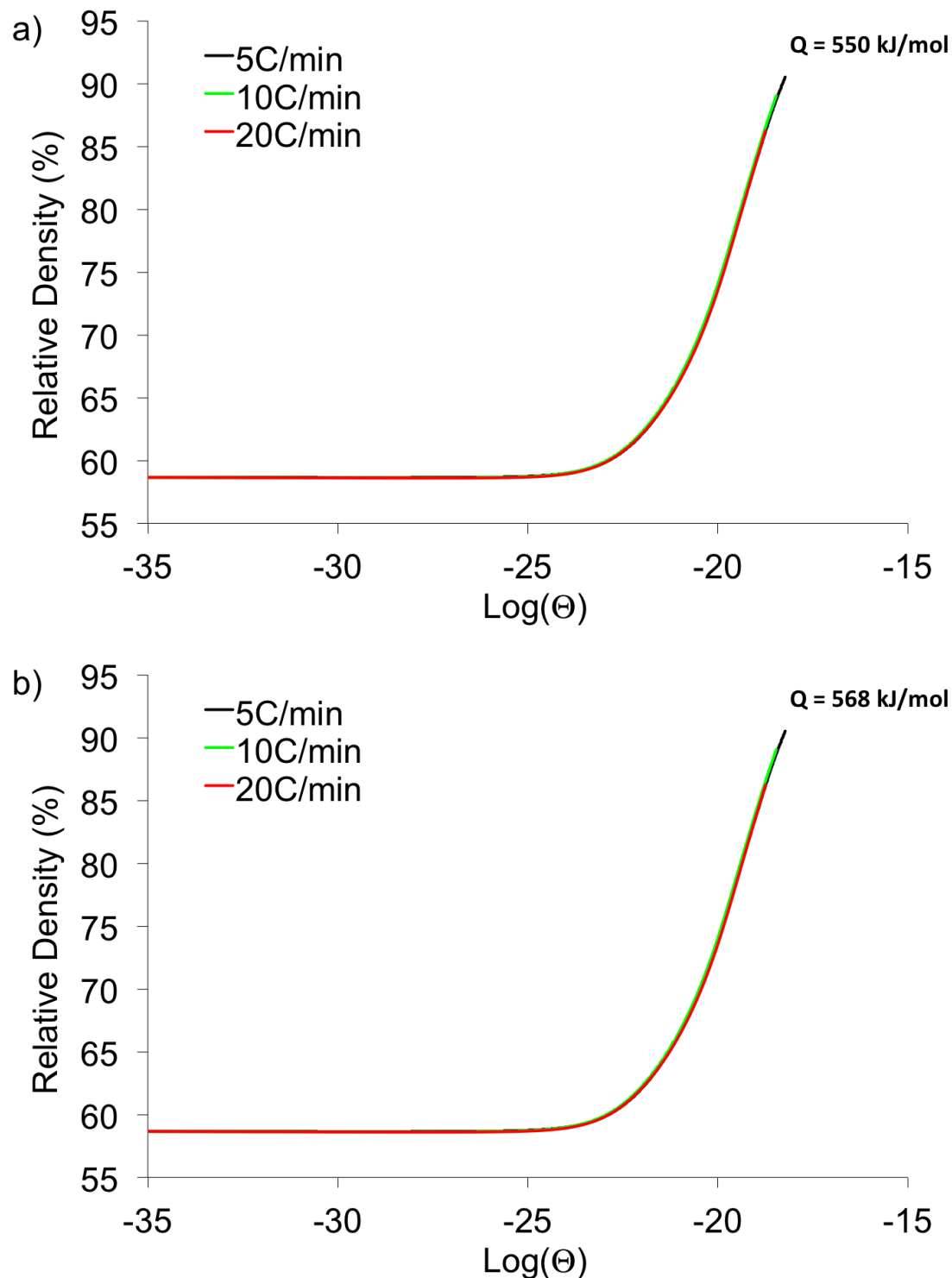


Figure 6.6. MSC curves of CT3000LS-SG samples prepared by non-aqueous slip casting using the activation energy obtained from a) minimum mean residuals, and b) the average of the iso-density analysis.

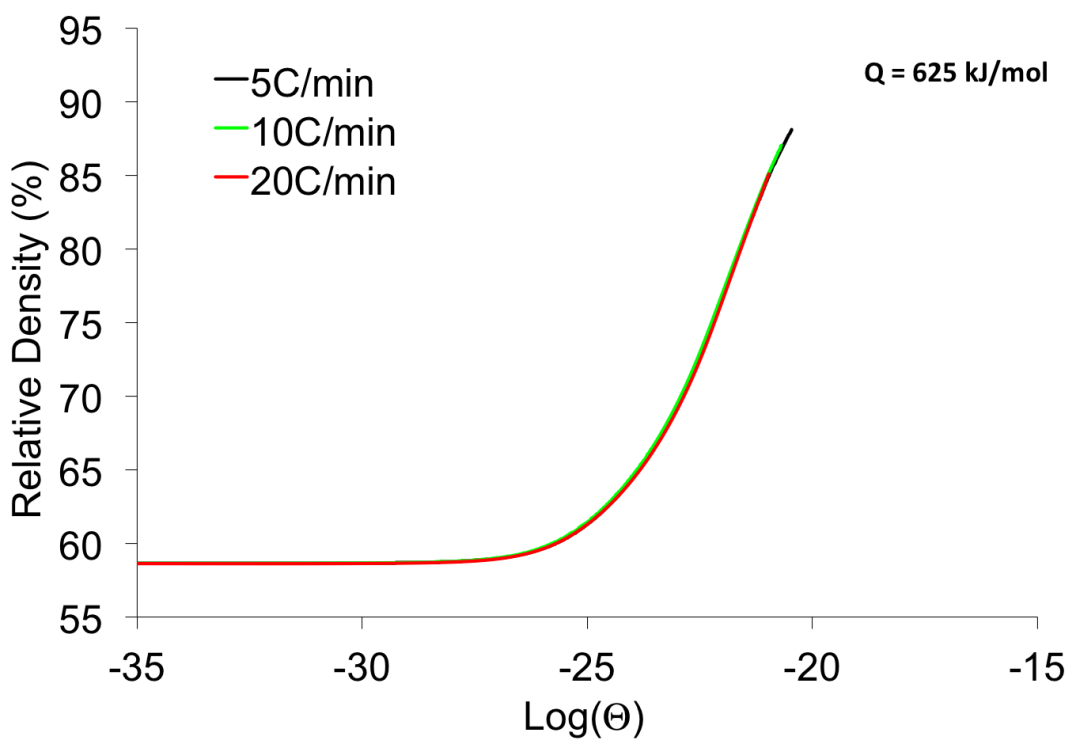
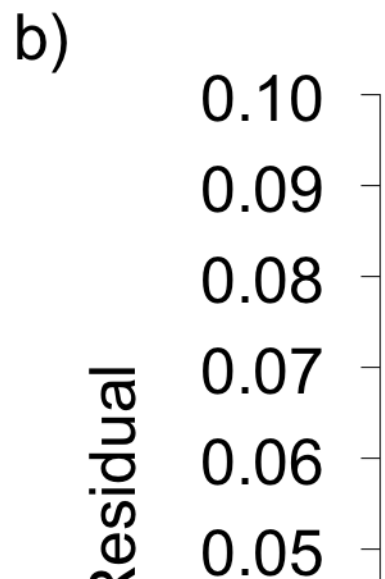
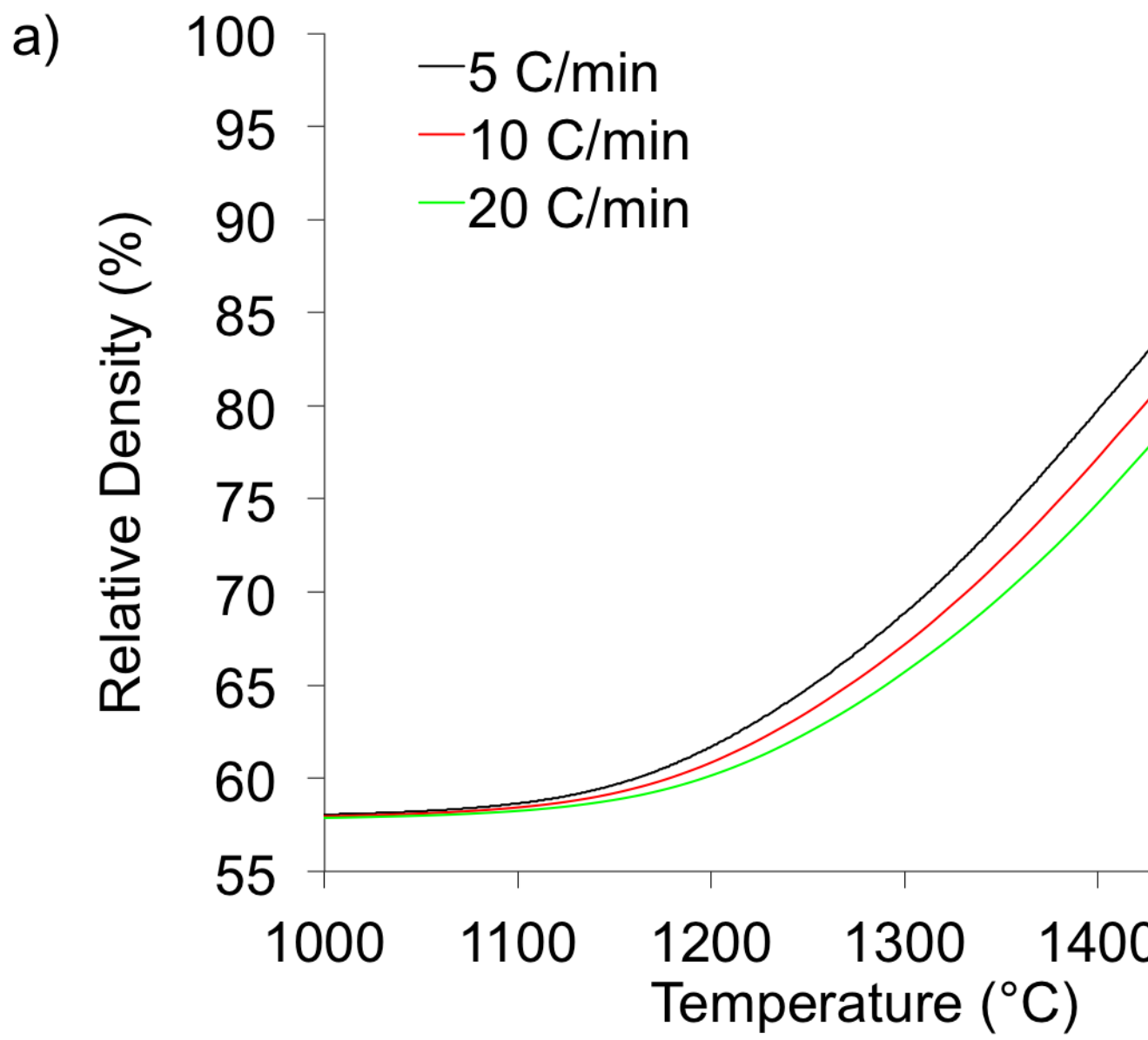


Figure 6.7. MSC curve of CT3000LS-SG samples prepared by non-aqueous slip casting neglecting the anisotropic shrinkage in the samples. Q was obtained from the minimum mean residuals.



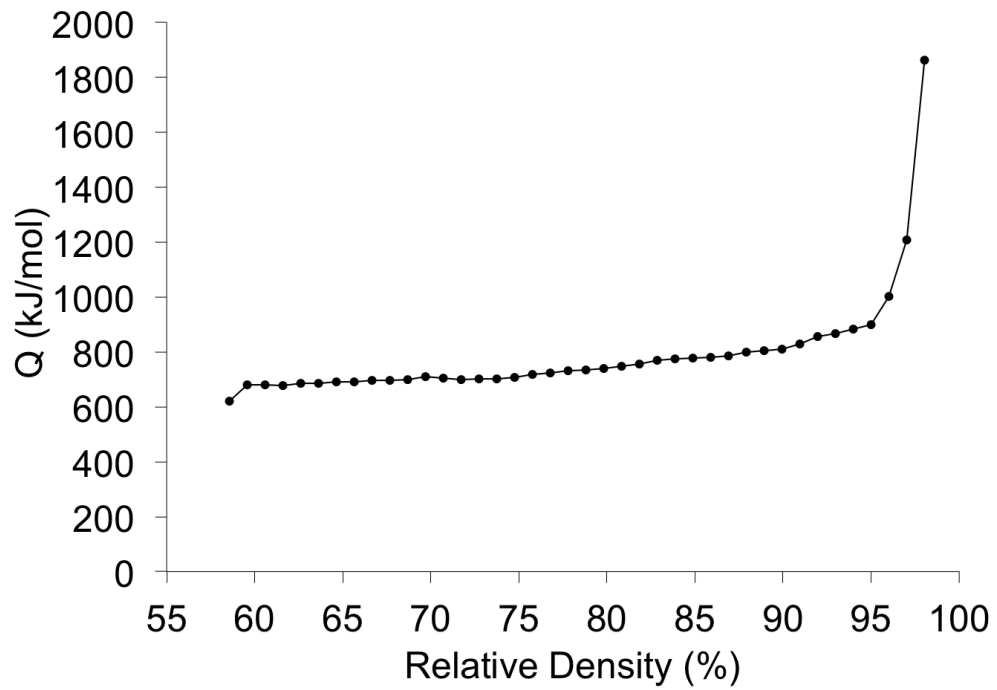


Figure 6.9. Activation energy of dry pressed CT3000LS-SG samples as a function of relative density obtained from iso-density analysis.

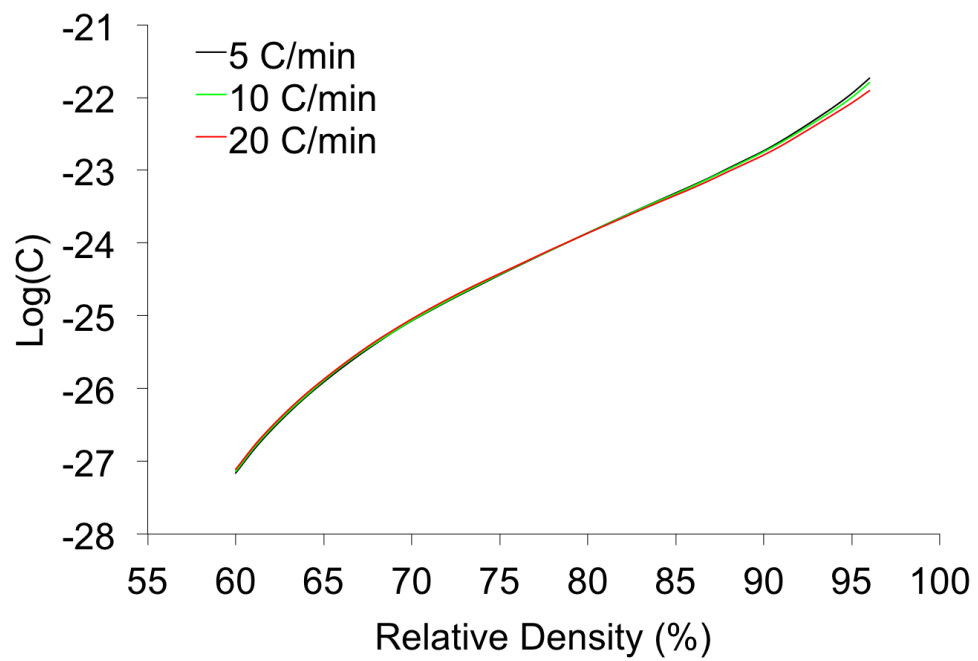


Figure 6.10. Development of the microstructural parameters, summarized in a factor C , as a function of relative density for a dry pressed CT3000LS-SG sample.

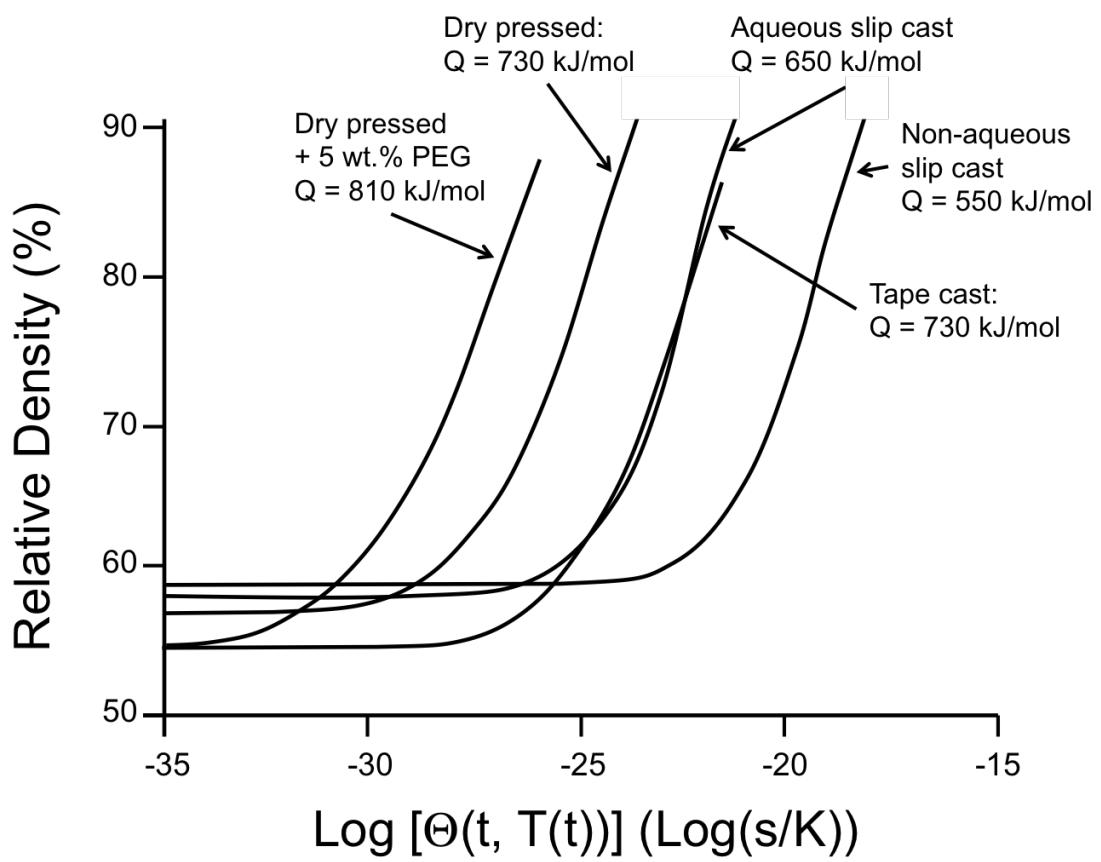


Figure 6.11. MSC curves and activation energies of CT3000LS-SG samples obtained from the minimum mean residuals for samples prepared by different forming techniques.

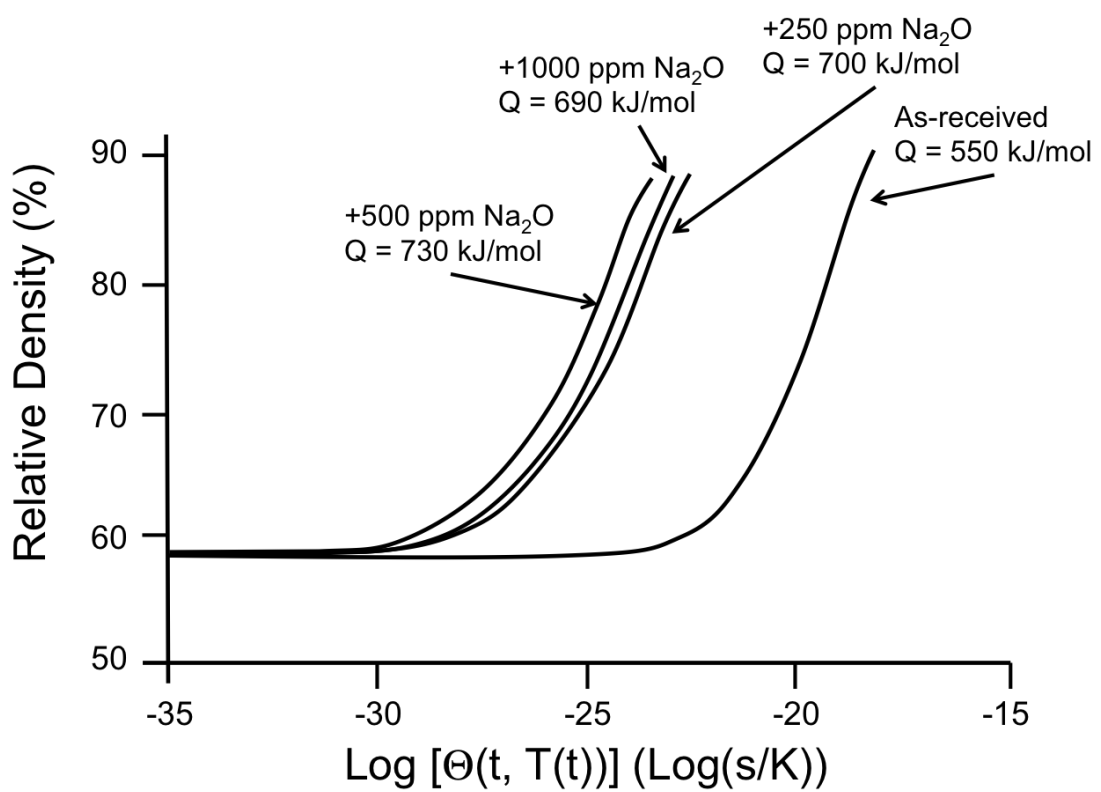


Figure 6.12. MSCs and activation energies for CT3000LS-SG samples prepared by non-aqueous slip casting with different Na_2O concentrations.

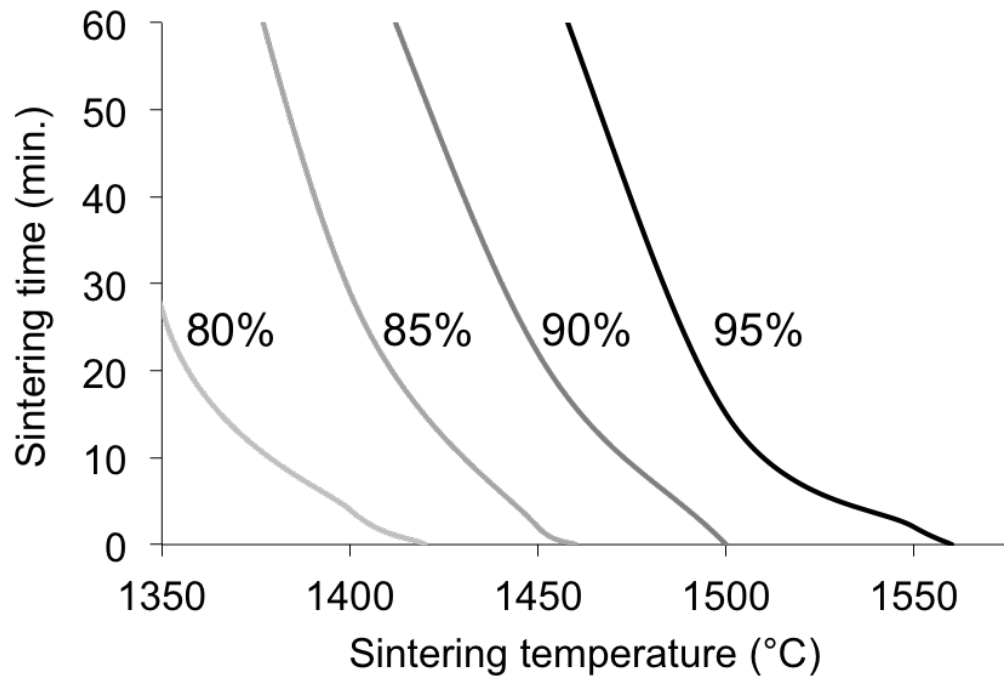


Figure 6.13. Equivalent time/temperature diagram for CT3000LS-SG samples prepared by non-aqueous slip casting heated at 10°C. The contours indicate what heat treatment is required to obtain the shown density.

Chapter 7 |

Summary and Future Work

7.1 Introduction

When in the Course of human events, it becomes necessary for one people to dissolve the political bands which have connected them with another, and to assume among the powers of the earth, the separate and equal station to which the Laws of Nature and of Nature's God entitle them, a decent respect to the opinions of mankind requires that they should declare the causes which impel them to the separation.

7.2 More Declaration

We hold these truths to be self-evident, that all men are created equal, that they are endowed by their Creator with certain unalienable Rights, that among these are Life, Liberty and the pursuit of Happiness. —That to secure these rights, Governments are instituted among Men, deriving their just powers from the consent of the governed, —That whenever any Form of Government becomes destructive of these ends, it is the Right of the People to alter or to abolish it, and to institute new Government, laying its foundation on such principles and organizing its powers in such form, as to them shall seem most likely to effect their Safety and Happiness. Prudence, indeed, will dictate that Governments long established should not be changed for light and transient causes; and accordingly all experience hath shewn, that mankind are more disposed to suffer, while evils are sufferable, than to right themselves by abolishing the forms to which they are accustomed. But when a long train of abuses and usurpations, pursuing invariably the same Object evinces

a design to reduce them under absolute Despotism, it is their right, it is their duty, to throw off such Government, and to provide new Guards for their future security. —Such has been the patient sufferance of these Colonies; and such is now the necessity which constrains them to alter their former Systems of Government. The history of the present King of Great Britain [George III] is a history of repeated injuries and usurpations, all having in direct object the establishment of an absolute Tyranny over these States. To prove this, let Facts be submitted to a candid world.

Bibliography

- [1] BAE, I.-J. and S. BAIK (1997) “Abnormal grain growth of alumina,” **56**(192101), pp. 1149–1156.
- [2] COMPSON, C., N. ROSENBERGER, and M. SPREIJ (2013) “The Effect of SiO₂ and Na₂O content on the Sintering Behavior of Calcined Specialty Aluminas for the Ceramics Industry,” *CFI-Ceramic Forum International*, **90**(3), pp. E17–E22.
- [3] COBLE, R. L. (1961) “Sintering crystalline solids,” *Journal of applied physics*, **32**(5), pp. 787–799.
- [4] ——— (1962) “Sintering alumina: effect of atmospheres,” *Journal of the American Ceramic Society*, **45**(3), pp. 123–127.
- [5] ——— (1962), “Transparent alumina and method of preparation,” .
- [6] JORGENSEN, P. J. and J. H. WESTBROOK (1964) “Role of Solute Segregation at Grain Boundaries During FinalâŠStage Sintering of Alumina,” *Journal of the American Ceramic Society*, **47**(7), pp. 332–338.
- [7] JORGENSEN, P. J. (1965) “Modification of sintering kinetics by solute segregation in Al₂O₃,” *Journal of the American Ceramic Society*, **48**(4), pp. 207–210.
- [8] LÜCKE, K. and K. DETERT (1957) “A quantitative theory of grain-boundary motion and recrystallization in metals in the presence of impurities,” *Acta Metallurgica*, **5**(11), pp. 628–637.
- [9] CAHN, J. W. (1962) “The impurity-drag effect in grain boundary motion,” *Acta metallurgica*, **10**(9), pp. 789–798.
- [10] JOHNSON, W. C. and R. L. COBLE (1978) “A Test of the SecondâšPhase and ImpurityâšSegregation Models for MgOâšEnhanced Densification of Sintered Alumina,” *Journal of the American Ceramic Society*, **61**(3âš4), pp. 110–114.

- [11] ZUO, F., C. CARRY, S. SAUNIER, S. MARINEL, and D. GOEURIO (2013) “Comparison of the microwave and conventional sintering of alumina: effect of MgO doping and particle size,” *Journal of the American Ceramic Society*, **96**(6), pp. 1732–1737.
- [12] BAE, S. I. and S. BAIK (1993) “Determination of critical concentrations of silica and/or calcia for abnormal grain growth in alumina,” *Journal of the American ceramic society*, **76**(4), pp. 1065–1067.
- [13] ——— (1993) “Sintering and grain growth of ultrapure alumina,” *Journal of Materials Science*, **28**(15), pp. 4197–4204.
- [14] HANDWERKER, C. A., P. A. MORRIS, and R. L. COBLE (1989) “Effects of chemical inhomogeneities on grain growth and microstructure in Al₂O₃,” *Journal of the American Ceramic Society*, **72**(1), pp. 130–136.
- [15] GAVRILOV, K. L., S. J. BENNISON, K. R. MIKESKA, J. M. CHABALA, and R. LEVI-SETTI (1999) “Silica and magnesia dopant distributions in alumina by high-resolution scanning secondary ion mass spectrometry,” *Journal of the American Ceramic Society*, **82**(4), pp. 1001–1008.
- [16] KAYSER, W. A., M. SPRISSLER, C. A. HANDWERKER, and J. E. BLENDELL (1987) “Effect of a liquid phase on the morphology of grain growth in alumina,” *Journal of the American Ceramic Society*, **70**(5), pp. 339–343.
- [17] AHN, J. H., J. LEE, S. HONG, N. HWANG, and D. KIM (2003) “Effect of the Liquidâ€Forming Additive Content on the Kinetics of Abnormal Grain Growth in Alumina,” *Journal of the American Ceramic Society*, **86**(8), pp. 1421–1423.
- [18] HANSEN, S. C. and D. S. PHILLIPS (1983) “Grain boundary microstructures in a liquid-phase sintered alumina (α -Al₂O₃),” *Philosophical Magazine A*, **47**(2), pp. 209–234.
- [19] HARMER, M. P. (1984) “Use of solid-solution additives in ceramic processing,” *Advances in ceramics*, **10**, p. 679.
- [20] STANDARD, A. (2015) “B962-15 Standard Test Method for Density of Compacted or Sintered Powder Metallurgy (PM) Products Using Archimedes’ Principle,” .
URL www.astm.org
- [21] ——— (2013) “E112-13: Standard Test Methods for Determining Average Grain Size,” *West Conshocken*.
URL www.astm.org

- [22] JUDD, M., B. PLUNKETT, and M. POPE (1974) "The thermal decomposition of calcium, sodium, silver and copper (II) acetates," *Journal of Thermal Analysis and Calorimetry*, **6**(5), pp. 555–563.
- [23] BROWNMILLER, L. T. and R. H. BOGUE (1932) "The system CaO-Na 2 O-Al 2 O 3," *American Journal of Science*, (138), pp. 501–524.
- [24] PABLOÂŘGALAN, L. and W. R. FOSTER (1959) "Investigation of Role of Beta Alumina in the System Na₂OâŘAl₂O₃âŘSiO₂," *Journal of the American Ceramic Society*, **42**(10), pp. 491–498.
- [25] RANKIN, G. A. and H. E. MERWIN (1916) "THE TERNARY SYSTEM CaO-Al₂O₃-MgO." *Journal of the American Chemical Society*, **38**(3), pp. 568–588.
- [26] RIDGWAY, R. R., A. A. KLEIN, and W. J. O'LEARY (1936) "The Preparation and Properties of SoâŘCalled âĲBeta AluminaâÍ," *Transactions of the Electrochemical Society*, **70**(1), pp. 71–88.
- [27] SUTORIK, A. C., S. S. NEO, D. R. TREADWELL, and R. M. LAINE (1998) "Synthesis of Ultrafine β âŖAlumina Powders via Flame Spray Pyrolysis of Polymeric Precursors," *Journal of the American Ceramic Society*, **81**(6), pp. 1477–1486.
- [28] STEVENS, R. and J. G. P. BINNER (1984) "Structure, properties and production of β -alumina," *Journal of materials science*, **19**(3), pp. 695–715.
- [29] CHRISTIE, J. R., A. J. DARNELL, and D. F. DUSTIN (1978) "Reaction of molten sodium carbonate with aluminum oxide," *J. Phys. Chem.;(United States)*, **82**(1).
- [30] KUMMER, J. T. (1972) " β -alumina electrolytes," *Progress in solid state chemistry*, **7**, pp. 141–175.
- [31] VRIES, R. C. and W. L. ROTH (1969) "Critical Evaluation of the Literature Data on Beta Alumina and Related Phases: I, Phase Equilibria and Characterization of Beta Alumina Phases," *Journal of the American Ceramic Society*, **52**(7), pp. 364–369.
- [32] TERAI, R. and R. HAYAMI (1975) "Ionic diffusion in glasses," *Journal of Non-Crystalline Solids*, **18**(2), pp. 217–264.
- [33] KWON, O. and G. L. MESSING (1990) "Kinetic Analysis of SolutionâŘPrecipitation During LiquidâŘPhase Sintering of Alumina," *Journal of the American Ceramic Society*, **73**(2), pp. 275–281.

- [34] KWON, O.-H. and G. L. MESSING (1991) “A theoretical analysis of solution-precipitation controlled densification during liquid phase sintering,” *Acta metallurgica et materialia*, **39**(9), pp. 2059–2068.
- [35] PARK, C. W. and D. Y. YOON (2000) “Effects of SiO₂, CaO₂, and MgO additions on the grain growth of alumina,” *Journal of the American ceramic society*, **83**(10), pp. 2605–2609.
- [36] DAY, D. E. and G. E. RINDONE (1962) “Properties of soda aluminosilicate glasses: I, refractive index, density, molar refractivity, and infrared absorption spectra,” *Journal of the American Ceramic Society*, **45**(10), pp. 489–496.
- [37] WU, G., E. YAZHENSKIHKH, K. HACK, and M. MÜLLER (2015) “Viscosity model for oxide melts relevant to fuel slags. Part 2: The system SiO₂-Al₂O₃-CaO-MgO-Na₂O,” *Fuel Processing Technology*, **138**, pp. 520–533.
- [38] POPOVIC, A., L. BENCZE, J. KORUZA, B. MALIC, and M. KOSEC (2012) “Knudsen effusion mass spectrometric approach to the thermodynamics of Na₂O-Nb₂O₅ system,” *International Journal of Mass Spectrometry*, **309**, pp. 70–78.
- [39] GALLUP, J. (1935) “The transformation of aluminum oxide from the beta to the alpha form,” *Journal of the American Ceramic Society*, **18**(1–12), pp. 144–148.
- [40] BAE, S. I. and S. BAIK (1994) “Critical concentration of MgO for the prevention of abnormal grain growth in alumina,” *Journal of the American Ceramic Society*, **77**(10), pp. 2499–2504.
- [41] BENNISON, S. J. and M. P. HARMER (1990) “A history of the role of MgO in the sintering of alpha-Al₂O₃,” in *Ceramic Transactions 7, Sintering of Advanced Ceramics* (C. A. Handwerker, J. E. Blendell, and W. A. Kaysser, eds.), Am. Ceram. Soc., Westerville, pp. 13–49.
- [42] HEUER, A. H. (1979) “The role of MgO in the sintering of alumina,” *Journal of the American Ceramic Society*, **62**, pp. 317–318.
- [43] PARK, C. W. and D. Y. YOON (2000) “Grain growth of alumina,” *609*(3), pp. 2605–2609.
- [44] FRUEH, T., E. KUPP, C. COMPSON, J. ATRIA, and G. MESSING (2016) “The effects of Na₂O and SiO₂ in liquid phase sintering of Bayer Al₂O₃,” *Journal of the American Ceramic Society*, **99**(7), pp. 2267–2272.

- [45] SHANG, S., Y. WANG, D. KIM, and Z.-K. LIU (2010) “First-principles thermodynamics from phonon and Debye model: Application to Ni and Ni₃Al,” *Computational Materials Science*, **47**(4), pp. 1040–1048.
- [46] WANG, Y., Z.-K. LIU, and L.-Q. CHEN (2004) “Thermodynamic properties of Al, Ni, NiAl, and Ni₃Al from first-principles calculations,” *Acta Materialia*, **52**(9), pp. 2665–2671.
- [47] LIU, X. L., B. K. VANLEEUWEN, S. SHANG, Y. DU, and Z.-K. LIU (2015) “On the scaling factor in Debye–Grüneisen model: A case study of the Mg–Zn binary system,” *Computational Materials Science*, **98**, pp. 34–41.
- [48] SHANG, S., Y. WANG, and Z.-K. LIU (2007) “First-principles elastic constants of alpha- and theta-Al₂O₃,” *Applied Physics Letters*, **90**(10), pp. 101909–1–101909–3.
- [49] KRESSE, G. and J. FURTHMÜLLER (1996) “Efficiency of ab-initio total energy calculations for metals and semiconductors using a plane-wave basis set,” *Computational Materials Science*, **6**(1), pp. 15–50.
- [50] KRESSE, G. and D. JOUBERT (1999) “From ultrasoft pseudopotentials to the projector augmented-wave method,” *Physical Review B*, **59**(3), pp. 1758–1775.
- [51] BLÖCHL, P. (1994) “Projector augmented-wave method,” *Physical Review B*, **50**(24), p. 17953.
- [52] PERDEW, J. and Y. WANG (1992) “Accurate and simple analytic representation of the electron-gas correlation energy,” *Physical Review B*, **45**(23), p. 13244.
- [53] MONKHORST, H. and J. PACK (1976) “Special points for Brillouin-zone integrations,” *Physical Review B*, **13**(12), pp. 5188–5192.
- [54] ATKINSON, K. J. W., R. W. GRIMES, M. R. LEVY, Z. L. COULL, and T. ENGLISH (2003) “Accommodation of impurities in α -Al₂O₃, α -Cr₂O₃ and α -Fe₂O₃,” *Journal of the European Ceramic Society*, **23**(16), pp. 3059–3070.
- [55] GRIMES, R. W. (1994) “Solution of MgO, CaO, and TiO₂ in α -Al₂O₃,” *Journal of the American Ceramic Society*, **77**(2), pp. 378–384.
- [56] LAGERLÖF, K. P. D. and R. W. GRIMES (1998) “The defect chemistry of sapphire (α -Al₂O₃),” *Acta materialia*, **46**(16), pp. 5689–5700.
- [57] XIANG, X., G. ZHANG, X. WANG, T. TANG, and Y. SHI (2015) “A new perspective on the process of intrinsic point defects in α -Al₂O₃,” *Physical Chemistry Chemical Physics*, **17**(43), pp. 29134–29141.

- [58] SARSAM, J., M. W. FINNIS, and P. TANGNEY (2013) “Atomistic force field for alumina fit to density functional theory,” *The Journal of chemical physics*, **139**(20), p. 204704.
- [59] MAO, H., O. FABRICHNAYA, M. SELLEBY, and B. SUNDMAN (2005) “Thermodynamic assessment of the MgO-Al₂O₃-SiO₂ system,” *Journal of Materials Research*, **20**(04), pp. 975–986.
- [60] SUBRAMANIAM, A., C. T. KOCH, R. M. CANNON, and M. RÜHLE (2006) “Intergranular glassy films: An overview,” *Materials Science and Engineering A*, **422**(1-2), pp. 3–18.
- [61] JAIN, A., S. ONG, G. HAUTIER, W. CHEN, W. RICHARDS, S. DACEK, S. CHOLIA, D. GUNTER, D. SKINNER, and G. CEDER (2013) “The Materials Project: A materials genome approach to accelerating materials innovation,” *Apl Materials*, **1**(1), p. 11002.
- [62] “Materials Project,” .
URL <http://www.materialsproject.org>
- [63] GRAHAM, J. (1960) “Lattice spacings and colour in the system alumina - chromic oxide,” *Journal of Physics and Chemistry of Solids*, **12**, pp. 349–350.
- [64] BERGERHOFF, G., R. HUNDT, R. SIEVERS, and I. D. BROWN (1983) “The inorganic crystal structure data base,” *Journal of Chemical Information and Computer Sciences*, **23**(2), pp. 66–69.
- [65] KARLSRUHE, F. I. Z., “Inorganic Crystal Structure Database,” .
- [66] RAGHAVAN, V. (2010) “Al-Fe-O (Aluminum-iron-oxygen),” *Journal of Phase Equilibria and Diffusion*, **31**(4), p. 367.
- [67] DILLON, S. J., M. TANG, W. C. CARTER, and M. P. HARMER (2007) “Complexion : A new concept for kinetic engineering in materials science,” **55**, pp. 6208–6218.
- [68] CLARKE, D. R., T. M. SHAW, A. P. PHILIPSE, and R. G. HORN (1993) “Possible electrical double-layer contribution to the equilibrium thickness of intergranular glass films in polycrystalline ceramics,” *Journal of the American Ceramic Society*, **76**(5), pp. 1201–1204.
- [69] CLARKE, D. R. (1987) “On the equilibrium thickness of intergranular glass phases in ceramic materials,” *Journal of the American Ceramic Society*, **70**(1), pp. 15–22.
- [70] KINGERY, W. D. (2004) “Densification during sintering in the presence of a liquid phase. I. Theory,” *Journal of Applied Physics*, **30**1(1959).

- [71] LEE, S.-M. and S.-J. L. KANG (1998) “Theoretical analysis of liquid-phase sintering: Pore filling theory,” *Acta Materialia*, **46**(9), pp. 3191–3202.
- [72] SHAW, T. M. (1986) “Liquid redistribution during liquid-phase sintering,” *Journal of the American Ceramic Society*, **69**(1), pp. 27–34.
- [73] SVOBODA, J., H. RIEDEL, and R. GAEBEL (1996) “A model for liquid phase sintering,” *Acta Materialia*, **44**(8), pp. 3215–3226.
- [74] GERMAN, R. M. (2016) “Sintering trajectories: Description on how density, surface area, and grain size change,” *Jom*, **68**(3), pp. 878–884.
- [75] ISRAELACHVILI, J. (2011) *Intermolecular and Surface Forces*.
- [76] HSIEH, C., H. JAIN, and E. I. KAMITSOS (1996) “Correlation between dielectric constant and chemical structure of sodium silicate glasses,” *Journal of Applied Physics*, **80**(3), pp. 1704–1712.
- [77] LYON, K. (1942) “Calculation of surface tensions of glasses,” *Journal of The American Ceramic Society-Lyon*, **27**(6), pp. 25–28.
- [78] ZHANG, S. and S. H. GAROFALINI (2005) “Molecular dynamics computer simulations of the interface structure of calcium-alumino-silicate intergranular films between combined basal and prism planes of α -Al₂O₃,” *Journal of the American Ceramic Society*, **88**(1), pp. 202–209.
- [79] TANAKA, I., H.-J. KLEEBE, M. K. CINIBULK, J. BRULEY, D. R. CLARKE, and M. RÜHLE (1993) “Calcium concentration dependence of the intergranular film thickness in silicon nitride,” *Journal of the American Ceramic Society*, **77**(4), pp. 911–914.
- [80] TOPLIS, M. J., D. B. DINGWELL, and T. LENCI (1997) “Peraluminous viscosity maxima in Na₂O-Al₂O₃-SiO₂ liquids: The role of triclusters in tectosilicate melts,” *Geochimica et Cosmochimica Acta*, **61**(13), pp. 2605–2612.
- [81] LITTON, D. A. and S. H. GAROFALINI (1999) “Atomistic structure of sodium and calcium silicate intergranular films in alumina,” *Journal of Materials Research*, **14**(4), pp. 1418–1429.
- [82] STILLWELL, C. V. (1926) “The Color of the Ruby,” *J. Phys. Chem.*, **30**, pp. 1441–1466.
- [83] RAY, A. K. and E. C. SUBBARAO (1975) “Synthesis of sodium beta and beta” alumina,” *J. Phys. Chem.*, **10**(6), pp. 583–590.

- [84] DUNCAN, J. H. and W. E. C. CREYKE (1969) “The formation and stability of beta-Al₂O₃ in alpha-Al₂O₃ Ceramics,” *Trans. Brit. Ceram. Soc.*, pp. 137–144.
- [85] SU, H. and D. L. JOHNSON (1996) “Master Sintering Curve: a practicle approach to sintering,” *J. Am. Ceram. Soc.*, **79**(12), pp. 3211 – 3217.
- [86] HANSEN, J. D., R. P. RUSIN, M.-H. TENG, and D. L. JOHNSON (1992) “Combined-Stage Sintering Model,” *Journal of the American Ceramic Society*, **75**(5), pp. 1129–1135.
- [87] BLAINE, D. C., S. J. PARK, and R. M. GERMAN (2009) “Linearization of master sintering curve,” *Journal of the American Ceramic Society*, **92**(7), pp. 1403–1409.
- [88] BLAINE, D. C., S. J. PARK, P. SURI, and R. M. GERMAN (2006) “Applcation of work-of-sintering concepts in powder metals,” *Metallurgical and Materials Transactions A: Physical Metallurgy and Materials Science*, **37**(9), pp. 2827–2835.
- [89] SHAO, W., S. O. CHEN, D. LI, and S. S. ZHANG (2009) “Construction of the master sintering curve for submicron size α -Al₂O₃ based on non-isothermal sintering containing lower heating rates only,” *Materials Science-Poland*, **27**(1), pp. 97– 107.
- [90] TATAMI, J., Y. SUZUKI, T. WAKIHARA, T. MEGURO, and K. KOMEYA (2006) “Control of Shrinkage during Sintering of Alumina Ceramics Based on Master Sintering Curve Theory,” *Key Engineering Materials*, **317-318**, pp. 11–14.
- [91] POUCHLY, V. and K. MACA (2009) “Master sintering curves of two different alumina powder compacts,” *Processing and Application of Ceramics*, **3**(4), pp. 177–180.
- [92] AMINZARE, M., F. GOLESTANI-FARD, O. GUILLO, M. MAZAHERI, and H. R. REZAIE (2010) “Sintering behavior of an ultrafine alumina powder shaped by pressure filtration and dry pressing,” *Materials Science and Engineering A*, **527**(16-17), pp. 3807–3812.
- [93] GUILLO, O. and J. LANGER (2010) “Master sintering curve applied to the Field-Assisted Sintering Technique,” *Journal of Materials Science*, **45**(19), pp. 5191–5195.
- [94] SHAO, W. Q., S. O. CHEN, D. LI, H. S. CAO, Y. C. ZHANG, and S. S. ZHANG (2009) “Prediction and control of microstructure evolution for sub-microscale beta-Al₂O₃ during low-heating-rate sintering based on the master

- sintering curve theory,” *Journal of the European Ceramic Society*, **29**(1), pp. 201–204.
- [95] OLEVSKY, E. A., S. KANDUKURI, and L. FROYEN (2008) “Consolidation enhancement in spark-plasma sintering : Impact of high heating rates Consolidation enhancement in spark-plasma sintering : Impact of high,” **114913**(2007).
- [96] RAETHER, F. and P. SCHULZE HORN (2009) “Investigation of sintering mechanisms of alumina using kinetic field and master sintering diagrams,” *Journal of the European Ceramic Society*, **29**(11), pp. 2225–2234.

Vita

Tobias Frueh

The details of my childhood are inconsequential.